Winter 2018

Development of a 300 KV DC High Voltage Photogun and Beam Based Studies of Alkali Antimonide Photocathodes

Yan Wang
Old Dominion University

DEVELOPMENT OF A 300 KV DC HIGH VOLTAGE PHOTOGUN AND BEAM BASED STUDIES OF ALKALI ANTIMONIDE PHOTOCATHODES

by

Yan Wang
B.S., July 1985, Department of Physics, Liaoning University, China
M.S., December 1995, Department of Physics, Old Dominion University

A Dissertation Submitted to the Faculty of
Old Dominion University in Partial Fulfillment of the
Requirements for the Degree of

DOCTOR OF PHILOSOPHY

PHYSICS

OLD DOMINION UNIVERSITY
December 2018

Approved by:

G. A. Krafft (Director)

H. Baumgart (Member)

R. Kazimi (Member)

T. Satogata (Member)

R. Schiavilla (Member)

ABSTRACT

DEVELOPMENT OF A 300 KV DC HIGH VOLTAGE PHOTOGUN AND BEAM BASED STUDIES OF ALKALI ANTIMONIDE PHOTOCATHODES

Yan Wang
Old Dominion University, 2018
Director: Dr. G. A. Krafft

To advance magnetized gun research in the United States, a compact DC high voltage photogun with inverted-insulator geometry was designed, built, and operated reliably at -300 kV bias voltage using alkali-antimonide photocathodes. This photogun will provide a magnetized electron beam for the future Jefferson Lab Electron-Ion Collider (JLEIC) cooler. This research describes key electrostatic design features of the photogun and evaluates the performance of the in-house fabricated photocathodes and the quality of the electron beams. The thermal emittance of the electron beam was measured with various conditions: different gun bias voltages, different laser spot sizes, and photocathodes with different substrate materials. It has been hypothesized that the photocathode surface roughness affects the quality of the photocathodes and the electron beam produced, which is directly related to the thickness of the antimony layer of the photocathode. This effect was studied experimentally for both the beam emittance and photocathode quantum efficiency lifetime, and the measurements indicate that the beam emittance is largely independent of the antimony layer thickness, and the lifetime benefits from a thick layer. The ion bombardment always poses a problem for the photocathodes during high current beam operations. An effective way to repel the beam-induced ions was identified and implemented, and a sustainable 28 mA beam was achieved from the gun. This thesis presents a summary of the good performance of the photogun, a remarkable quantum efficiency lifetime of the photocathodes, and a low emittance of the electron beam.

To Individuals and Organizations Who Support Science

ACKNOWLEDGMENTS

I must express my sincere gratitude to my supervisor, Dr. R. Kazimi, the project manager, Dr. M. Poelker, and my advisor, Dr. G. A. Krafft. They encouraged me to go back to school, helped me find the research project, and provided me with guidance during the course of this research.

I would like to thank Dr. C. Hernandez-Garcia for teaching me how to high voltage condition photoguns, Dr. M. Mamun for training me how to fabricate alkali antimonide photocathodes, and Dr. R. Suleiman for showing me how to use the Root program to calculate the beam emittance. We often sat in the GTS control room discussing the program, making run plans, finding solutions to the problems we encountered, and tuning and running beam together. I really enjoyed working together with them and learning from them. I am sure I will miss the fun, the frustration, and the joy we had in the GTS control room.

I owe special thanks to Dr. M. Tiefenback who helped me troubleshoot the problems with the beamline wires scanner. He also taught me how to use Gnuplot to process the wire scanner data. He is knowledgeable and willing to teach. Special thanks also go to Dr. J. Benesch who is another source of help. Whenever I knocked his door he always made time for me and patiently explained how things work. My colleague, Dr. A. Hofler also deserves my special thanks. She always offered her help when I asked for it.

I am thankful that the GTS beamline was built in a timely manner and was quickly and successfully commissioned. I learned a lot about vacuum from Mr. B. Bullard and Mr. P. Adderley during the construction of the GTS beamline. I learned from Mr. J. Hansknecht how to swap the high voltage cables, and how to bypass the high voltage conditioning resister. During the gun high voltage conditioning Mr. Bullard would start everything very early in the morning and then I would take over later. Mr. E. Diggs, Mr. J. Delk, Mr. K. Banks, and Mr. M. Augustine installed all the magnets. Mr. T. Dela Crus, Mr. K. Cole, and Mrs. S. Witherspoon installed the wire scanner and the related software. Mr. G. Croke and Dr. W. Lu made the software control (MEDM) ready. Mr. B. Freeman made the viewer software user friendly. Mr. D. Machie, Mr. J. Hoerger and Mr. G. Hay made the drawing and model of the GTS beamline. Dr. S. Zhang did a very good job to maintain the laser so that it was always ready for use. Mr. G. Palacios-Serrano generated GTS gun field maps.

My committee members, Dr. G. A. Krafft, Dr. H. Baumgart, Dr. R. Kazimi, Dr. T. Satogata, and Dr. R. Schiavilla were always available when I needed their help and advice. In

particular, Dr. G. A. Krafft always came to me first to discuss the project, checked the progress, and made sure the research was going well. He read my thesis thoroughly to ensure all the details were in correct order. My committee helped me improve my research skills. I would not be where I am without their support. I am really grateful.

In the Physics Department at Old Dominion University, I owe thanks to Dr. L. Vuskovic and Ms. L. Okun. They always encouraged me academically and helped me administratively.

I wanted to thank my family for their support. My parents have been encouraging me to learn and do my best academically since my childhood. Through all these years, especially the last few years of my graduate studies, they did everything they could to support me with unconditional love.

I am indebted to many people for their help and support during my research. I know despite my best efforts that I will inadvertently fail to remember everyone here. I apologize to anyone I have left out. Each person's contribution is appreciated even if unacknowledged here.

This work is supported by the Department of Energy under contract DE-AC05-06OR23177. Additional support comes from Laboratory Directed Research and Development program.

TABLE OF CONTENTS

LIST OF TABLES

LIST OF FIGURES

CHAPTER 1

INTRODUCTION

The next large nuclear physics research facility being proposed to the Department of Energy for construction is an Electron-Ion Collider (EIC) [1]. An EIC will provide unique capabilities for the study of Quantum Chromodynamics (QCD), the theory that describes how quarks and gluons build protons, neutrons, and nuclei. In March 2013, NSAC ranked an EIC as absolutely central in its ability to contribute to world-leading science research. The EIC will accelerate electrons on one side and protons or ions on the other to nearly the speed of light before slamming the two streams of particles together. These collisions would allow scientists to probe deep inside the nucleus of the atom to discover the hidden workings of nature that are responsible for all visible matter.

The proposed Electron-Ion Collider will ensure that the cutting-edge science that has kept Jefferson Lab and the United States at the frontier of nuclear physics research for 25 years will continue for decades to come. Two laboratory efforts, at Jefferson Lab and Brookhaven National Lab in New York, are developing facility concepts. HERA, the first and only electron-ion collider to date, operated from 1992 to 2007. HERA was a technological achievement, but the physics output was limited by its low luminosity. Recently collider designers have focused on maximizing the luminosity, both peak and integrated.

For the Jefferson Lab Electron-Ion Collider (JLEIC) proton or ion beams, there is no synchrotron radiation damping of the beam particles. Therefore an efficient damping mechanism, namely, beam cooling, must be introduced to deliver high luminosity performance in the collider. Such beam cooling will be required to enable a significant reduction of the proton or ion beam emittance, up to an order of magnitude in all directions. This reduction allows a very short bunch with a very small beam spot at collision to be delivered. The JLEIC ion beams will be cooled by conventional electron cooling, a proven technology, both at low energy and high energy. JLEIC adopts a scheme of multi-phase cooling, which uses electron cooling both during formation of the ion beam, particularly including an initial cooling at low energy, and during collision for enhancing the cooling efficiency. This scheme is based on the fact that the cooling time is proportional to ion beam emittance and beam energy.

Three electron coolers are required to implement the JLEIC cooling scheme. In the booster, a low voltage DC cooler with electron energy up to 55 keV is needed for cooling during ion accumulation. In the collider ring, a modest high voltage DC cooler with electron energy up to 4.3 MeV is needed to pre-cool proton and ion beams for emittance reduction. In addition, a high energy bunched beam cooler with electron energy up to 54.5 MeV is needed for cooling of ion beams during collision.

During the cooling the energy of the thermal motion of the ions is transferred to the cold electron gas. The cooling rate can be improved by co-propagating the electron and ion beams inside a solenoid field provided that the electron beam is magnetized, i.e., the electron beam is not rotating when inside the solenoid. In a magnetized state, the trajectories of the electrons are small helices around the magnetic field lines in the cooling solenoid thereby increasing the interaction time and improving the cooling efficiency. Therefore electron cooling of ion beams often benefits from the use of magnetized electron beams.

A magnetized electron beam is produced from a photocathode immersed in an axial magnetic field. Then the electron beam is transported and matched to a magnetized state into the long solenoid magnet composing the cooling section [2]. Given the importance of JLEIC and a crucial role of magnetized electron beam in the JLEIC cooling a reliable electron source is a must. A primary motivation of this research is to provide a suitable electron source for the magnetized electron beam for future JLEIC cooling. The magnetized beam is a fairly new concept and prior to this work there has been no experimental research done on this subject at Jefferson Lab.

Field emission, or electron field emission, is emission of electrons induced by an electrostatic field. The most common situation is emission from a metallic solid surface into vacuum at high surface electric field. As part of this effort, one needs to design and construct a 300 kV DC high voltage photogun and operate the gun at high voltage with minimum field emission. It is essential that electrodes exhibit little or no field emission during continuous operation at high voltages because field emission is most commonly an undesirable primary source of vacuum breakdown and electrical discharge phenomena. Low-level field emission at nano-Ampere levels desorbs gas from the vacuum chamber walls by direct impact and by x-ray stimulated desorption, leading to enhanced ion bombardment of the photocathode which hastens quantum efficiency decay. Field emission at the micro-Ampere level can lead to high voltage breakdown that completely eliminates photocathode quantum efficiency and in some instances can result in irreparable damage of the photogun insulator.

In order to reduce or eliminate field emission great care must be taken to design the gun,

polish its parts, and high voltage condition the gun. First, a gun design must avoid sharp edges and reduce the metal surface biased to high voltage. This is why the cathode electrode should be spherical. Some old gun designs have a T-shaped cathode electode. Both ends of a T-shaped electrode have right angles, which is not optimal. High electric field accompanies high voltage leading to field emission from the metal surface. The gun design in this research employs an inverted-insulator geometry, which significantly reduces both the metal surface biased to high voltage and the volume of the gun chamber.

Second, the cathode electrode and its associated parts must be polished and cleaned because rough and contaminated surface is a good source of field emission. The cathode electrode and its associated parts were polished to mirror-like conditions. Traditionally the polishing was done using diamond paste. The results are good but this process is very time consuming. Barrel polishing with corncob media and plastic cones was tried, which provides comparable results to traditional diamond paste polishing but uses much less time.

The last step is the gun high voltage conditioning. Current conditioning is typically the default technique for high voltage conditioning a new photogun, whereby voltage is applied to the electrode in small increments, allowing the pre-breakdown field emission current to stabilize. The field emission current decreases to a smaller level over time as field emission sources burn off. Current conditioning as a means to eliminate field emission is not effective once the bias voltage reaches a certain level, usually around -200 kV. Gas conditioning is more effective. The gas conditioning works via ion implantation and sputtering. In this research noble gas krypton was employed to condition the gun. The partial pressure of Kr used in this research was in 10^{-7} Torr range.

The new gun design also adopted the load-lock technique, i.e., there is a photocathode deposition chamber separated from the photogun chamber, with the benefit of keeping the gun chamber clean so that the components in the gun chamber will not be contaminated with chemicals. This new gun design is very compact, which helps support excellent vacuum conditions. Although the application of high voltage using a cable represents a non-trivial technical challenge, having an inverted-insulator gun eliminates the need for a bulky SF_6 tank attached to the gun, thereby greatly simplifying the mechanical design of the gun.

Photocathodes are important parts of photoguns. The JLEIC collider cooling needs non-polarized high current magnetized electron beams. Past scientific experience indicates that the alkali antimonide photocathodes are a good candidate for this purpose. Several Cs_xK_ySb photocathodes were made and studied in this work. The photocathodes are thin

Cs_xK_ySb films deposited on substrates. The photocathodes were fabricated using two different substrate materials, GaAs and molybdenum, with various thickness of the Sb layer. When making a photocathode, a layer of Sb is deposited on a substrate. Then K and Cs are co-deposited on top of the Sb layer. Traditionally K and Cs are deposited on the Sb layer sequentially. The co-deposition technique is expected to produce low emittance beam. In this research all the photocathodes were fabricated with co-deposition of K and Cs on the Sb layers. The thickness of the Sb layer affects the surface roughness of the Cs_xK_ySb photocathodes, which, in turn, may affect beam quality. This possibility was studied experimentally. The thickness of the Sb layer is controlled by the deposition time while keeping the temperature of the Sb source constant. The Sb deposition time ranges from 10 to 90 minutes and the corresponding thickness of the Sb layer ranges from about a few dozen nm to several hundred nm. The size of the active photocathode area can be controlled using a mask with holes of different sizes. The size of the active area can be from 3, 5, and 12.8 mm. After each photocathode is fabricated a quantum efficiency (QE) map is obtained across the whole photocathode to check the quality. A diagnostic beamline was built to test the photogun, and to study the alkali antimonide photocathodes. The beam emittance and QE lifetime of the photocathodes were measured. Also magnetized beam was generated and studied.

The beam emittances were measured under various conditions using the scan-solenoid technique. At different beam bunch charges the beam emittance was measured to see at what bunch charge the space charge starts to affect the beam emittance. The thermal emittance is the interest of this research. If beam current is too high space charge effect will be present. Then the emittance was quantified at different gun bias voltages to verify the theory that the normalized beam emittance is independent of the gun bias voltage once the beam becomes relativistic. A beam emittance map was obtained for a photocathode by scanning the incident laser spot on the photocathode with a full activation area (12.8 mm diameter) in the horizontal plane and the vertical plane and measuring the beam emittance at each point, checking whether the gun field asymmetry affects the beam emittance or not. The laser spot size at the photocathode affects the beam emittance but the thermal angle should remain constant. The thermal angle is the beam emittance normalized to the laser spot size. This expectation was verified for each photocathode, and the results are comparable to the published data. It is believed that the photocathode surface roughness affects the beam emittance but no published was available until this research was done. There is no obvious effect from the surface roughness.

Delivery of high current electron beam is also a goal. During the QE lifetime studies high

current running was achieved. Achieving the high current was a challenge. A significant number of ions were generated during high current operations. Some of those ions travel into the photogun chamber and hit the photocathode. This ion bombardment damages the photocathode, which causes the photocathode QE to drop. After an intensive period of study a way to repel the ions was found and stable high current operations was accomplished. Biasing the gun anode positively prevents the photocathode from damage.

The outcome of the measurements and studies is very promising and satisfactory. The photogun has been operated up to 300 kV reliably with minimum field emission. The beam emittance is low and good, comparable to the published data from other research institutes. The photocathodes demonstrate a remarkably good lifetime. The highest beam current was 28 mA. The beam current was limited by the laser power and the power of the high voltage power supply, and not by any inherent limitations in the photocathode material.

The gun test stand (GTS) in the lower energy recirculator facility (LERF) at Jefferson Lab was a convenient place for this research. A high voltage power supply (HVPS), a laser system, and a personnel safety system for the beam enclosure were already available in the GTS. This research work was started at GTS in summer 2015.

CHAPTER 2

APPARATUS

This research project was conducted in the Gun Test Stand (GTS) located in the Low Energy Recirculator Facility (LERF) building at Jefferson Lab. The apparatus consists of a High Voltage Power Supply (HVPS), two laser systems, a photocathode preparation chamber, a gun chamber, and a short beamline as shown in Figure 1.

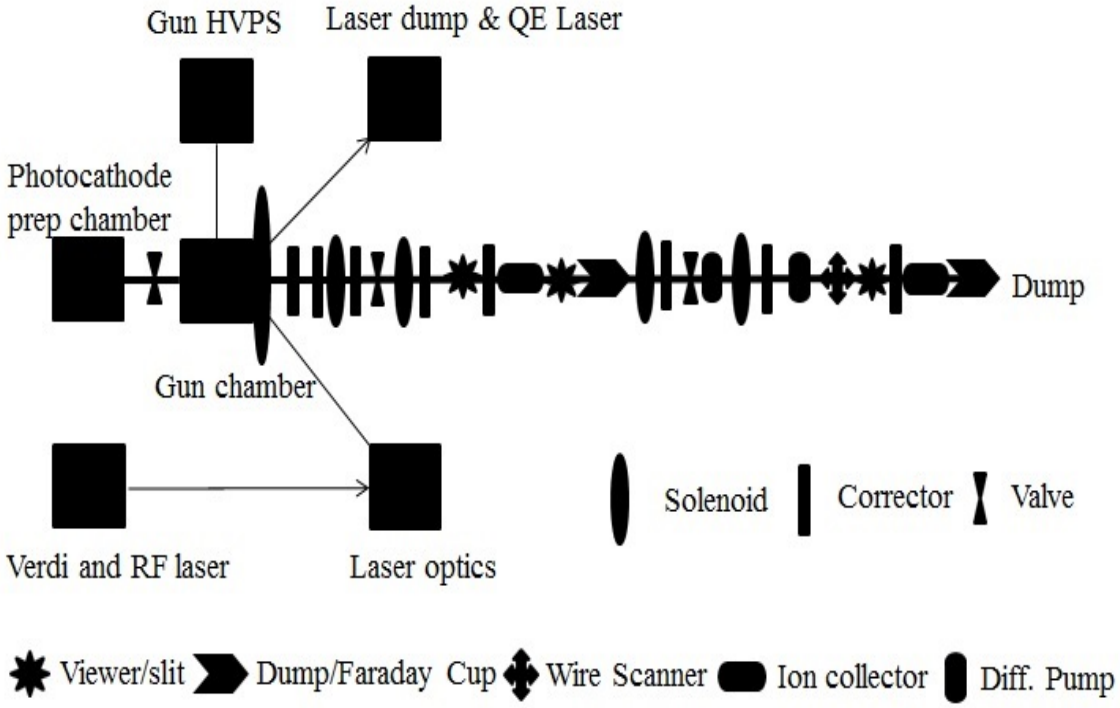

FIG. 1: The schematic of the GTS apparatus.

2.1 HIGH VOLTAGE POWER SUPPLY (HVPS)

A 600 kV power supply, as shown in Figure 2, provides the beam energy for the GTS beam. It is a Jefferson Lab modified Glassman model PS/PK500N004YU2 consisting of a voltage multiplier stack, a monitor stack, and a power driver. The multiplier stack is a

48 stage full-wave Cockcroft-Walton (C-W) voltage multiplier, rated in air at 500 kV and 4 mA. The C-W stack was modified with smaller corona rings and installed in a pressure tank. When this tank is filled with SF_6 gas above 5 psig, additional insulation and cooling is provided for operation up to 600 kV and 5 mA. The power driver electronics have also been modified to achieve this output.

The monitor stack acts as the feedback voltage divider for the power driver circuitry. It provides a divider probe for both the AC and DC components of the output voltage, and acts as a bleeder resistor for the capacitors of the multiplier stack. The AC and DC outputs can be viewed on an oscilloscope to verify proper operation. A solid-state pulse width modulated (PWM) power drive unit provides up to 12 kV of drive voltage for the C-W multiplier stack. The power input to the driver is 3 phase 208 VAC, which is directly rectified and filtered for use in the PWM chopper. The JLab Operational Safety Procedure (OSP) has the detailed information on the power supply used in the GTS [3].

FIG. 2: The 600 kV, 5 mA power supply used in GTS.

The insulating gas handling system consists of mechanical pumps and various solenoid control valves used to fill the HVPS with SF_6. Instrument air is used to purge and backfill

the tanks prior to opening the tank. The mechanical pumps have switching valves used to evacuate the SF_6 from the tank to the gas storage bag and to evacuate the tank of air prior to backfilling with SF_6. To replace any SF_6 that is lost from the system, several high-pressure SF_6 gas cylinders, located outside, are used to refill the gas recovery bag. If the pressure in the tank is above 13 psi, a relief valve opens and the SF_6 flows back into the recovery gas bladder. The system is designed to be pressurized up to 10 psig and is equipped with the normal complement of control valves and pressure gauges.

2.1.1 CONNECTION OF THE HVPS TO THE GUN CHAMBER

The photogun is connected to the high voltage power supply, with a 300 MΩ conditioning resistor in series. A male-type cable connector, as shown in Figure 3, fits precisely into the conical inverted insulator on the photogun and into a plastic receptacle supporting the conditioning resistor inside the HVPS SF_6 tank as shown in Figure 4. The ceramic insulator, plastic receptacle, and the high voltage cable are industry-standard components with dimensions specified by the commercial designation R30.

FIG. 3: (a) Industry-standard cable R30 plug. (b) A cut-away view of a cable R30 plug.

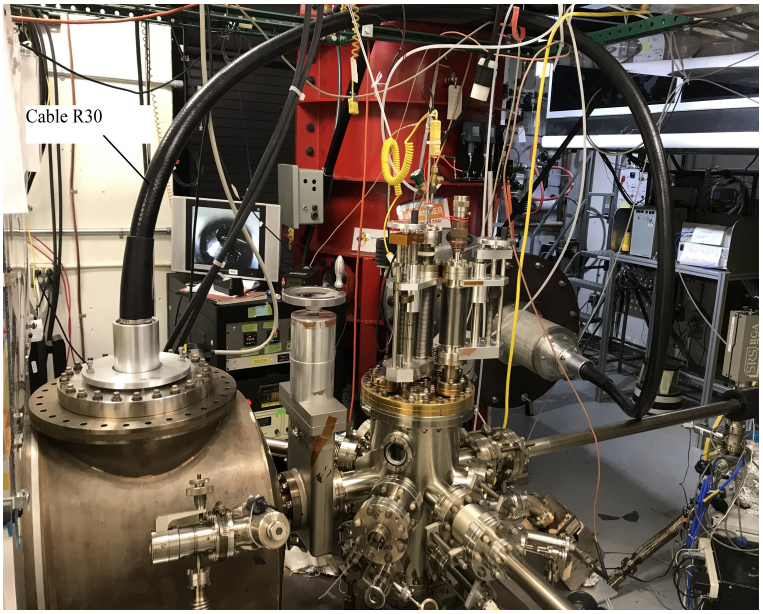

FIG. 4: An industry-standard high voltage cable connects the photogun and HVPS (thick black cable in the photograph).

2.2 LASER SYSTEMS

There are two main drive laser systems, which share the same optical path. One system is a Verdi DC laser, and the other a RF pulsed laser. In addition there are two small pen lasers for quantum efficiency (QE) measurement. All lasers are green lasers with 532 nm wavelength. A laser expert is responsible for the operations of lasers.

2.2.1 VERDI LASER

This laser is a DC laser which provides up to 2 W of power. The laser was used during the commissioning of the beamline including the trial runs of beam emittance measurements. After a RF laser was built the Verdi laser was kept as a spare but was not used again as the RF laser was very reliable.

2.2.2 RF LASER

The RF laser was built at Jefferson Lab. It is a pulsed laser and provides up to 2 W of power with a pulse repetition rate of 374 MHz and a pulse width of 50 ps. All the data in

this thesis were taken using the RF laser.

2.2.3 LASERS FOR QE SCANS

During the process of making a new photocathode the QE needs to be monitored in order to know when to stop depositing the alkali. Also QE mapping of a photocathode is performed before and after use. There are two small pen lasers for the QE measurement, one for the gun chamber and one for the photocathode preparation chamber. They are like laser pointers of 5 mW power and commercially available. The laser spot *rms* size on the photocathode is about 0.2 mm.

2.3 PHOTOCATHODE PREPARATION CHAMBER

The photocathode preparation chamber, as shown in Figure 5, is where new photocathodes are made and stored. The chamber, 20.3 cm in diameter and 38.1 cm long, was made

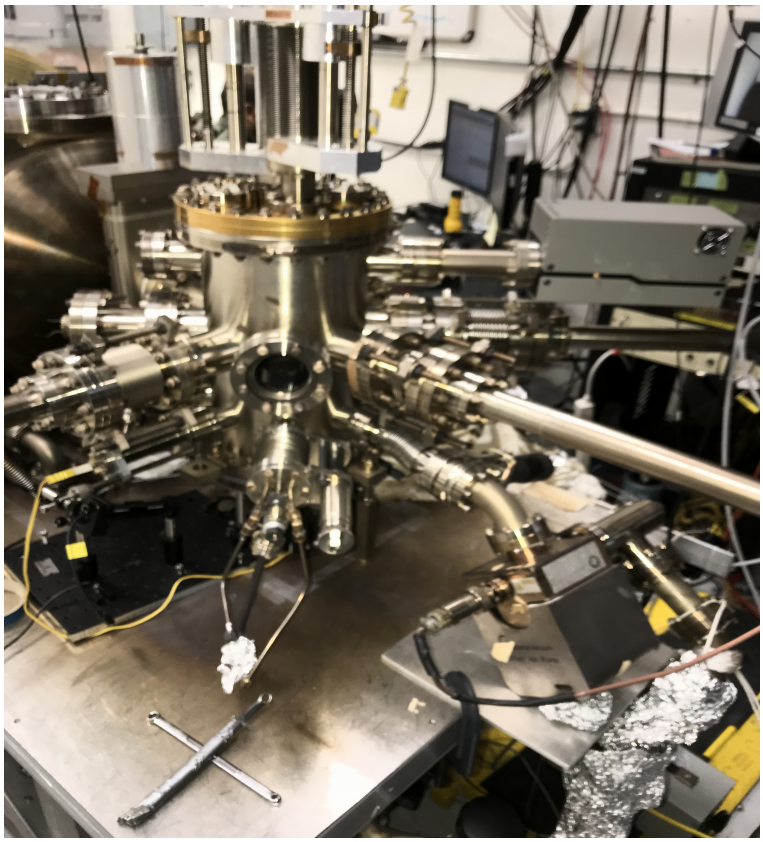

FIG. 5: The preparation chamber where photocathodes are made.

from 304L stainless steel sheet, 0.48 cm thick with a 0.8 μm root mean square (rms) surface finish that was rolled into a cylinder and welded. It consists of an antimony source, an alkali (cesium and potassium) source, two heaters, four manipulators, two non-evaporable getter (NEG) pumps, a mask, an ion pump, a residual gas analyzer (RGA), and three thermocouples. It is separated from the gun chamber using a gate valve. The chamber has several viewer ports made of Kodial Glass (alkali borosilicate 7056). Making photocathodes in a separate chamber isolates processing chemicals from the gun chamber so the gun chamber remains clean. The preparation chamber can serve as storage for processed and unprocessed cathodes as it can hold five pucks. The vacuum is maintained at 10^{-11} Torr using NEG pumps and an ion pump. Figure 6 is a schematic model of the preparation chamber.

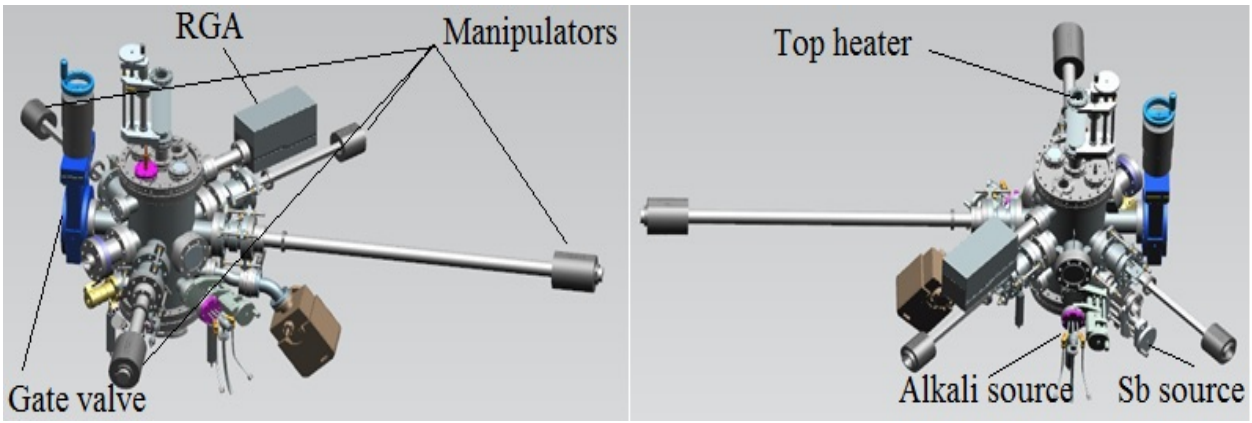

FIG. 6: The preparation chamber at a different viewing angle.

2.3.1 ANTIMONY SOURCE

Figure 6 shows that the Sb source assembly is attached to the prep chamber on the side. Inside the preparation chamber is a crucible made of aluminum oxide similar to the one shown in Figure 7. It sits in a tungsten evaporation basket that also serves as a heater. The crucible holds high-purity (99.9999%) Sb pellets from Alfa Aesar. The linear actuator inserts the basket into the center of the chamber during the deposition process or retracts it to the garage position when not in use. The crucible is resistively heated by applying current to the tungsten wire basket. The current is from a regulated DC power supply (Electronic Measurements, Inc., TCR 40S45-1DOVDC power supply 0-40 V, 0-45 A, 1800 W).

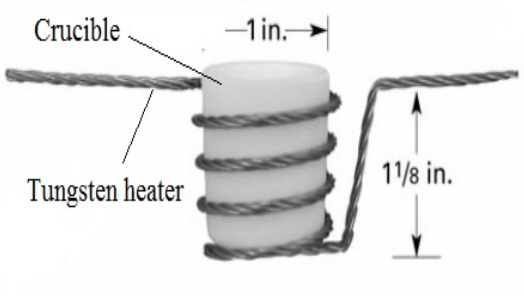

FIG. 7: A crucible in a tungsten heater.

2.3.2 ALKALI SOURCE

Figure 6 shows that the alkali source assembly is attached to the preparation chamber next to the antimony source. Figure 8 shows the alkali source assembly. An effusion type

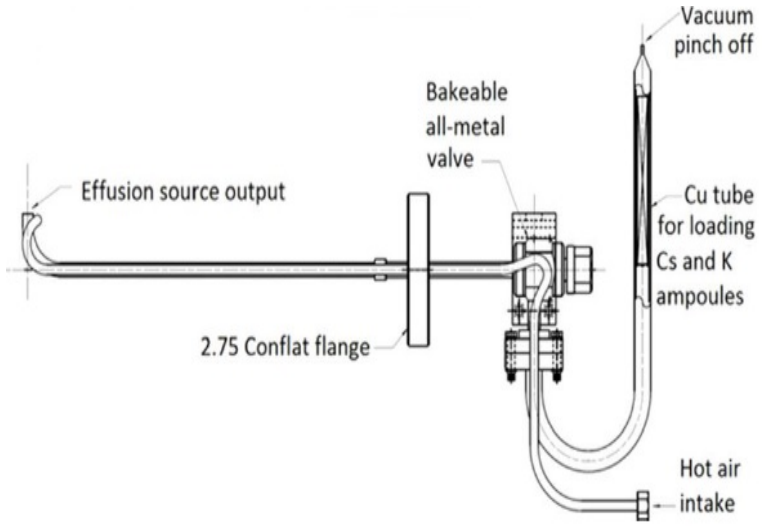

FIG. 8: An effusion-type alkali dispenser used for co-evaporation of K and Cs.

reservoir contains both K (99.95% purity) and Cs (99.9% purity) in 1 g break-seal ampules from ESPI metals and Strem Chemicals, Inc. [4]. During the deposition of Cs and K the hot air (or nitrogen) keeps the dispenser hot. Tape heaters are needed to heat the reservoir during the deposition. The effusion output nozzle can be inserted into the center of the chamber during the deposition via a linear actuator, or retracted when not in use. The Cs

and K are in the same tube. When heated, the vapor of both elements (Cs and K) emerges at the dispenser tip at the same time so they are deposited on the substrate simultaneously. The element ratio of Cs and K is not controlled during the deposition. This process is called co-deposition. Cs and K can also be independently controlled using two dispensers as there is a spare dispenser installed on the other side of the preparation chamber. In this research only one dispenser was used.

2.3.3 HEATERS

There are two heaters inside the chamber. The heater inserted from the bottom flange is for heat cleaning the puck (substrate) prior to fabricating a photocathode, and the one inserted from the top flange as shown in Figure 9 is for heating up the puck during fabrication

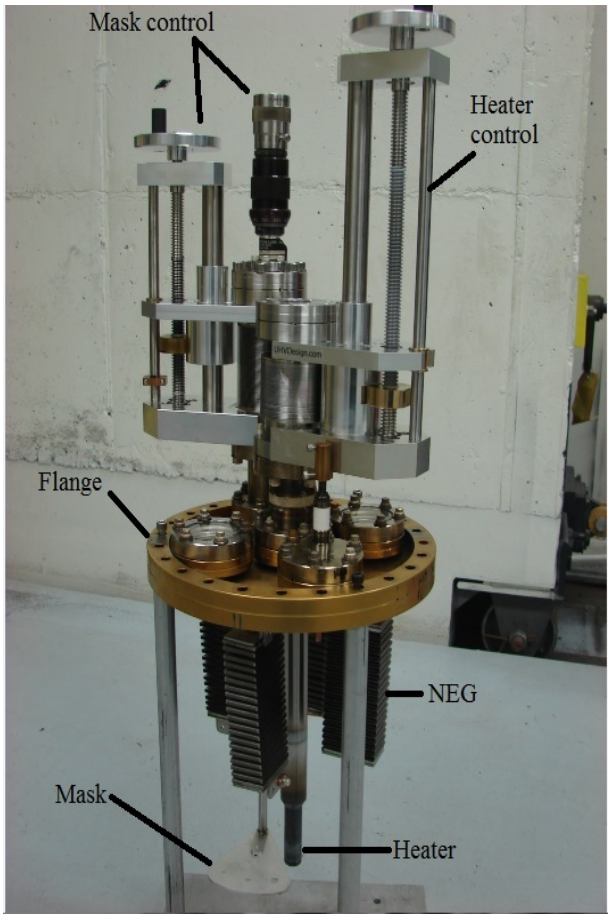

FIG. 9: Six NEG modules lie on the bottom of the gun chamber.

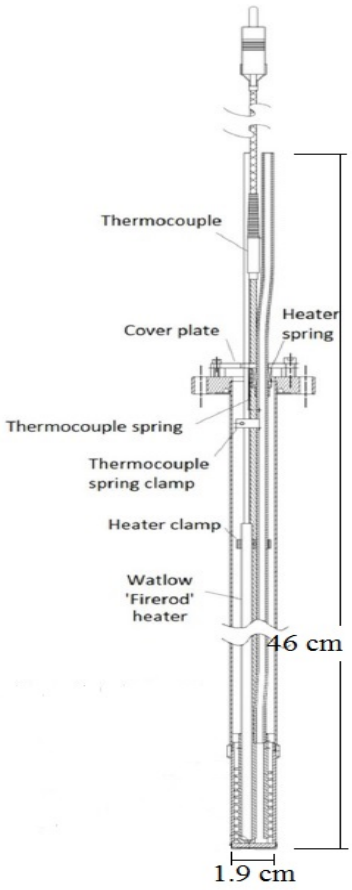

FIG. 10: A heater attached to the top flange.

of a photocathode. Both heaters can be moved up and down to the desired vertical positions. Each heater has a thermocouple which monitors the temperature and is used for the control system. The bottom heater faces up so that the puck can sit on top of it during the heat cleaning. The top heater faces down and has a grabbing system attached to it as shown in Figure 11. It can grab a puck and holds it tight against the heater so that the puck can be heated during the deposition of Sb or K and Cs. Figure 10 show details of the top heater.

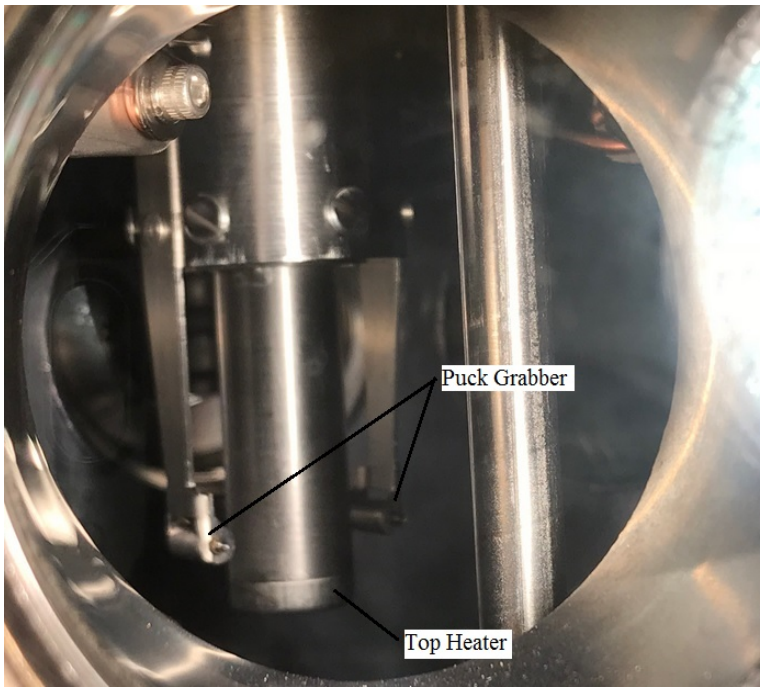

FIG. 11: A puck grabber attached to the top heater.

2.3.4 NEG PUMPS

Non-evaporable getter (NEG) pumps are based on the principle of metallic surface sorption of gas molecules, and mostly are constructed from porous alloys or powder mixtures of Al, Zr, Ti, V, and Fe. They help establish and maintain vacuum by soaking up or bonding to any gas molecules that remain within a vacuum system. This is done through the use of materials that readily form stable compounds with active gases. They are important tools for improving the performance of many vacuum systems. Usually they are activated during a bake of the vacuum system. There are four NEG modules installed onto the top flange of the preparation chamber as shown in Figure 9 on page 13.

2.3.5 MASK

The mask is a stainless steel metal plate with three holes in it. The holes have diameters of 1, 3, and 5 mm. It is used when one wants to make a photocathode with only small active area. When the mask is positioned between the puck and the Sb or K and Cs source only a small portion of the substrate is exposed to the deposition source. One can select a desired active area by aligning one of the three holes with the puck and the source during the deposition. The mask can be moved up or down via a linear actuator, or rotated via a rotation vernier. Figure 9 on page 13 shows how it is installed.

2.3.6 MANIPULATORS

There are four manipulators as shown in Figure 6 that can be inserted or retracted through a magnetized drive mechanism. Three of the manipulators can each hold three pucks. Two of those serve as storage and one is used to orient the pucks for heating and transfer. The last manipulator, which is the longest, is used to transfer a puck between the gun chamber and the photocathode preparation chamber. This longest manipulator can hold one puck. While the two storage manipulators can only move linearly the other two can move both linearly and rotationally. Figure 12 shows one of the manipulators.

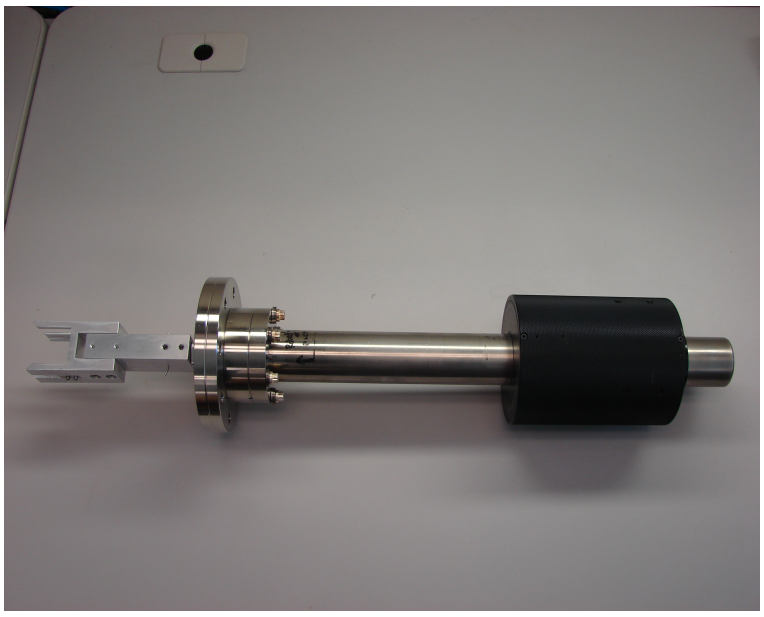

FIG. 12: One of the puck manipulators.

2.3.7 ION PUMPS

There is one ion pump for the prep chamber, one for the gun chamber, and five others positioned along the beamline. The ion pumps used at the GTS are made by Gamma Vacuum as shown in Figure 13. They have a pumping speed of 40 liters per second with an operating range from 10^{-6} to 10^{-12} Torr.

FIG. 13: An ion pump made by Gamma Vacuum.

2.3.8 RESIDUAL GAS ANALYZER

A residual gas analyzer, SRS model RGA200, works like a mass spectrometer and provides detailed gas analysis of vacuum. RGAs are used in most cases to monitor the quality of the vacuum and detect minute traces of impurities in the low-pressure gas environment. They can also be used as a sensitive leak detectors commonly using helium. During the process of making photocathodes a RGA is used to monitor the partial pressures of Sb, Cs, and K.

2.3.9 THERMOCOUPLES

A thermocouple is an electrical device consisting of two dissimilar electrical conductors forming an electrical junction. A thermocouple produces a temperature-dependent voltage as a result of the thermoelectric effect, and this voltage can be measured to determine the temperature. Thermocouples are a widely used type of temperature sensor. Thermocouples are used to monitor and control the temperatures of the puck and reservoir of the Cs and K while making a new photocathode.

2.4 PHOTOGUN VACUUM CHAMBER

The photogun vacuum chamber as shown in Figure 14 is connected to the beamline on the anode side, and to the photocathode preparation chamber on the opposite side. There is a gate valve on either side of the gun chamber so it can be isolated from the beamline or the photocathode preparation chamber. Inside the chamber there are an inverted insulator, a shed, a cathode electrode, and an anode. The chamber has the shape of a cylinder and is made of type 304L stainless steel. Its diameter is 46 cm and its length is 36 cm.

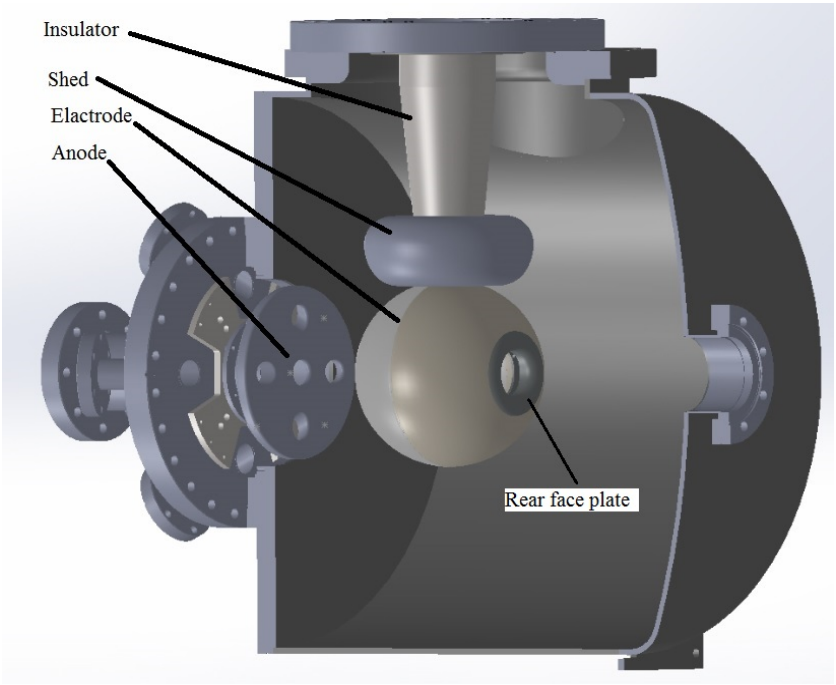

FIG. 14: Gun chamber section view: insulator, shed, cathode electrode, and anode.

2.4.1 ANODE

There are five holes in the anode plate as shown in Figure 14. The photoemitted electron beam passes through the large center hole and the other holes (two horizontal ones) provide a means to deliver a laser light to the photocathode at a 25° angle of incidence and to pass the unabsorbed reflected light outside the photogun as shown in Figure 15. The anode is electrically isolated from ground using sapphire balls, to provide a means to measure incident field emission. During high current runs the anode is positively biased to repel the ions created by the beam along the beamline. The top hole is used as a view port to monitor the laser spot location on the photocathode. The bottom hole is for the feedthrough to connect the anode electrically.

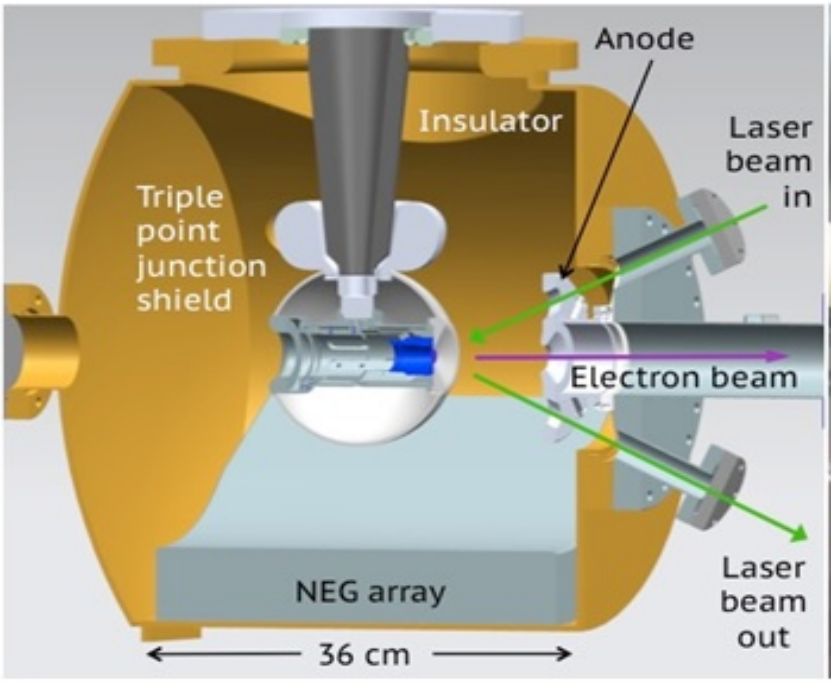

FIG. 15: The laser beam pass: Laser beam comes in from one port, hits the photocathode, and comes out from another port.

2.4.2 INVERTED INSULATOR, SHED, AND CATHODE ELECTRODE

The cathode electrode is spherical, six inches in diameter, and made of type 304L stainless steel. It is barrel polished to a mirror-like condition. A spherical shape for the cathode electrode is the best choice since it needs to sustain high operating voltage with low surface

field. In this research the cathode voltage will not exceed -300 kV. In order to bias the electrode inside the gun vacuum chamber there must be a transition from the high voltage cable outside the vacuum chamber to the cathode electrode inside the vacuum chamber. The gun vacuum chamber must remain at low vacuum of about 10^{-11} Torr to prevent degradation of the processed photocathode material. The gun vacuum chamber also must be electrically grounded and isolated from the high voltage cable and the electrode. This transition is achieved by introducing an insulator with one end welded onto a 25.4 cm flange as shown in Figure 16, with the other end connected to the electrode. The high voltage cable plugs into the insulator from the air side, which is the center of the flange, and electrically connects to the electrode at the other end of the insulator. The flange seals the vacuum chamber from the top.

FIG. 16: An insulator is welded on a 25.4 cm flange.

The 15.25 cm diameter cathode electrode is hollow. The narrow end of the conical insulator passes through a hole in the cathode electrode and mates to an internal fixture (locking device) as shown in Figure 17 that holds the photocathode puck. The spherical electrode possesses a front face with 1.28 cm opening and 25° focusing geometry which is the front piece. Spring-loaded sapphire rollers push the photocathode puck against the back of the focusing faceplate. Interior components of the electrode are held in place using a rear face plate, as shown in Figure 14, that also smooths the electrostatic field. Figure 18 shows the cathode electrode and its associated parts.

The region where the insulator meets the electrode ball is metal. Past experiences indicate that the electric field in this region is very high once the electrode is biased to a high voltage.

This high field broke down the insulator. The breakdown penetrated the insulator and caused vacuum leaks. In order to reduce the electric field in this region where the insulator and the electrode ball meets a metal piece, called a shed, is added as shown in Figure 19. The shed is attached to the electrode using screws. The shed looks like a doughnut and is designed using POISSON as part of this thesis work, to reduce the maximum field near the metal surface.

Figures 20 and 21 show all the parts assembled together. Figure 20 also shows the position of the photocathode when it is loaded into the cathode electrode. Figure 21 indicates where a photocathode is loaded into the cathode electrode.

FIG. 17: A locking device used to hold the photocathode puck.

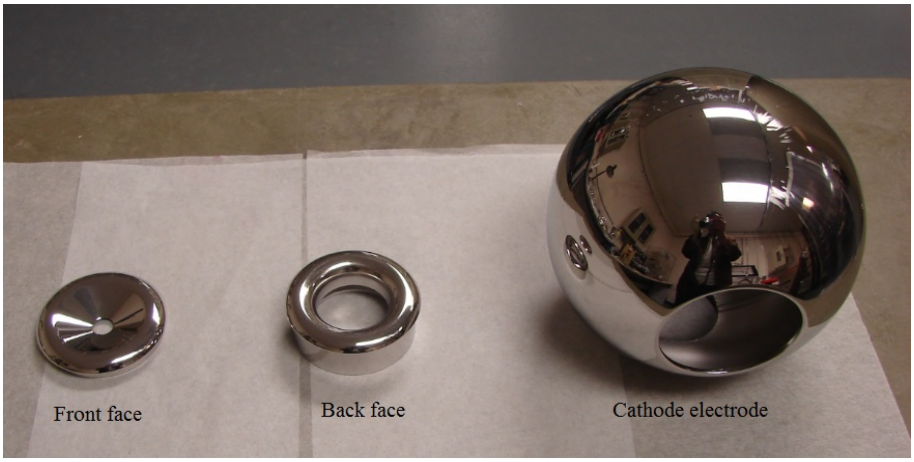

FIG. 18: The cathode electrode and its associated parts, front face, and back face.

FIG. 19: The shed with different view angles.

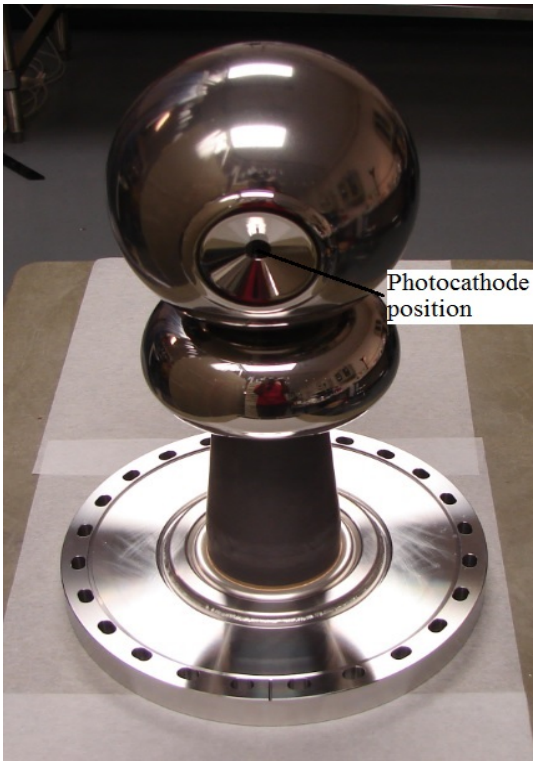

FIG. 20: All the parts assembled, facing front.

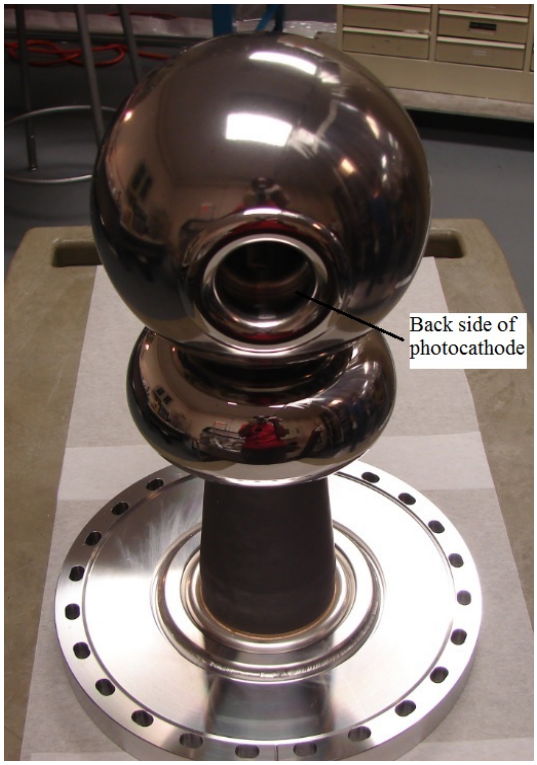

FIG. 21: All the parts assembled, facing back.

2.4.3 PUCKS

Pucks are made of molybdenum or stainless steel, and used to support the photocathode substrates. They have a cylinder-like shape as shown in Figure 22 and are hollow inside, with 2.87 cm height and 3.18 cm diameter. Prior to putting a puck inside the photocathode preparation chamber a substrate is secured to the top of the puck using a tantalum puck holder. Figure 22 (a) shows the top of a used puck with burn marks. Figure 22 (b) shows the hollow side of the puck, in which a heater can be inserted when transferring or heating up the puck.

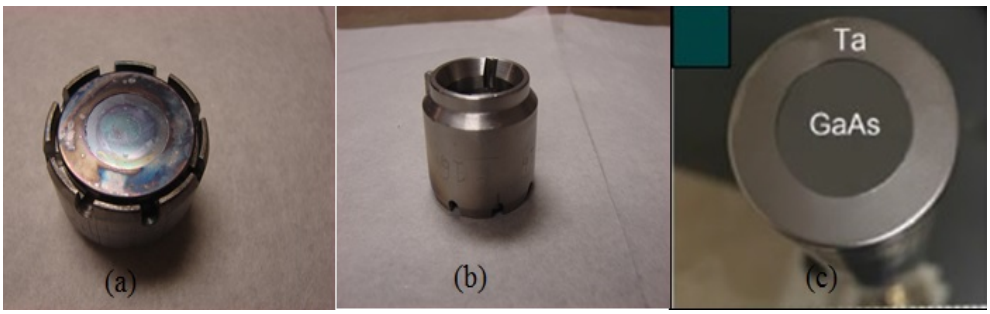

FIG. 22: A puck with different view angles. (a) Puck facing up. (b) Puck facing down. (c) Puck with Ta cup holding GaAs substrate. Note: Not to scale.

2.4.4 NEG PUMPS

As shown in Figure 23 the bottom half of the gun chamber is lined with an array of six non-evaporable getter (NEG) pump modules (SAES WP1250 with ST707 material) to provide an estimated pump speed of 4000 l/s for hydrogen, which is the dominant gas species inside the vacuum chamber. The NEG modules are activated during a bake-out and help maintain the vacuum afterwards. The NEGs are electrically isolated from the chamber since otherwise they cannot be activated. Figure 24 shows that a perforated ground screen covers the NEG modules to minimize the likelihood that NEG particulates become electrostatically charged and attracted to the cathode electrode initiating field emission. The NEG and ion pumps together maintain good vacuum in the photogun chamber (10^{-11} Torr).

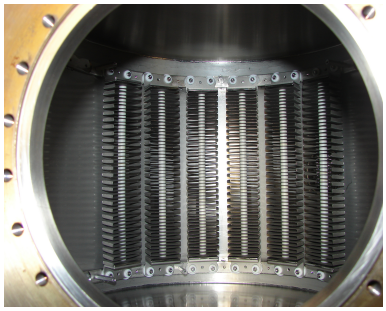

FIG. 23: Six NEG modules lie on the bottom of the gun chamber.

FIG. 24: A perforated metal sheet covers the NEG modules.

2.4.5 VARIABLE LEAK VALVE

All-metal leak valves are specifically designed to control gas admission into high vacuum systems. They are manually actuated and ideally suited for handling gases commonly used in demanding research environments. The valve body is constructed of type 304 stainless steel and fitted with a knife-edge seat made of a durable Stellite super-alloy. Valve leak rates can be adjusted down to a minimum leak of 7.5×10^{-8} Torr l s^{-1}. Leak rate is controlled by relieving the pressure applied to a replaceable nickel diaphragm. There is one leak valve installed on the gun chamber like the one shown in Figure 25. In this research the leak valve is used to introduce krypton gas into the gun chamber for the high voltage conditioning process. The valve has a precision control mechanism.

FIG. 25: A leak valve made by Kurt J. Lesker company

2.4.6 ION PUMPS AND TURBO PUMPS

There are two ion pumps attached to the gun vacuum chamber. One is used to maintain the vacuum of the chamber and is on at all times. The other is used during a bake-out. After a bake-out this ion pump is valved off, although the pump itself remains on. All the ion pumps used in the GTS are identical as shown in Figure 13 on page 16.

There is one turbo pump connected to both the gun chamber and photocathode preparation chamber. The operating pressure range is from one atmosphere to 10^{-8} Torr. The turbo pump is used to establish good enough vacuum (i.e., as a roughing pump) before turning on the ion pumps.

2.5 MAJOR BEAMLINE COMPONENTS

The beamline as shown in Figure 26 is relatively short, about 4.5 meters long from the gun chamber exit to the end of the beam dump. It is laid out on a straight line, i.e., it has

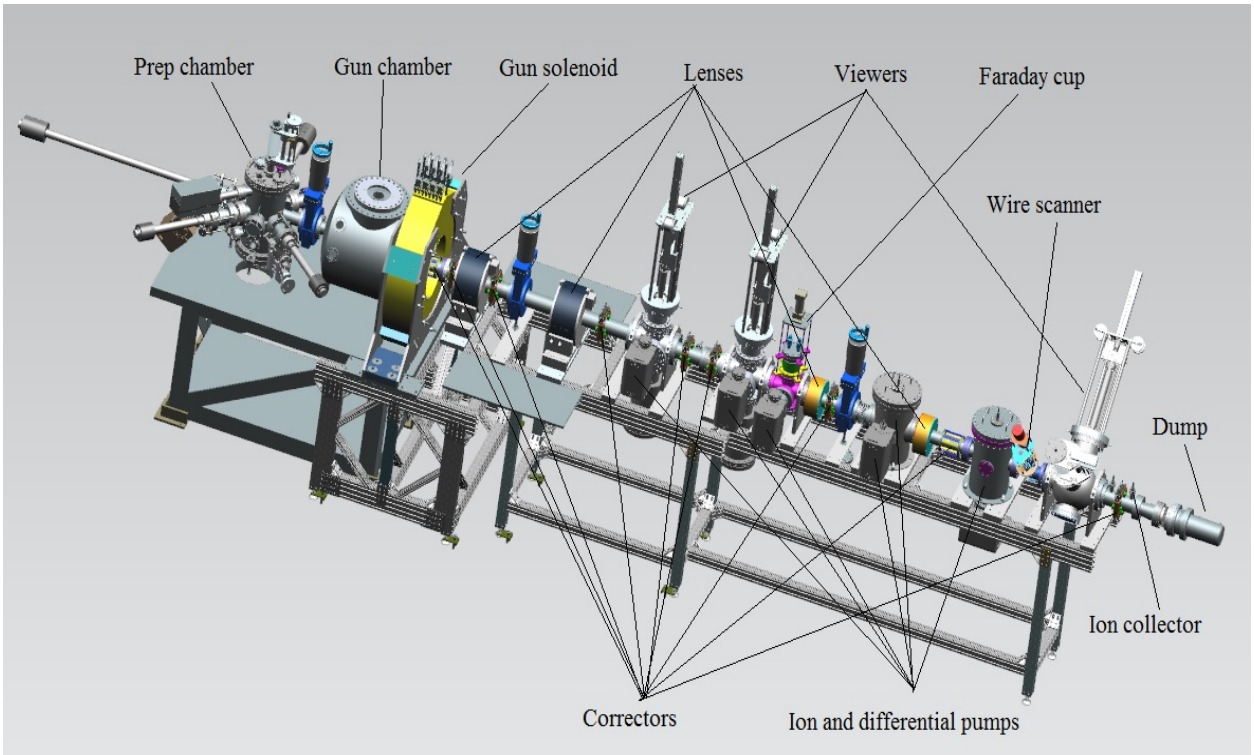

FIG. 26: The GTS beamline is about 4.5 m long from photocathode to dump.

no bends. On the beamline are one gun solenoid, four lenses (small solenoids), nine corrector pairs, three viewers, two slits, two ion collectors, two differential pumps, five ion pumps, two NEG pumps, one wire scanner, one Faraday cup, and one beam dump. There is no accelerating component aside from the gun high voltage so the beam energy remains the same from the beginning to the beam dump.

2.5.1 GUN SOLENOID

Figure 27 (a) and (b) show the gun solenoid on the test stand and installed in the beamline. The inner diameter of the gun solenoid is 30 cm, the outer diameter is 70 cm, and the length in the longitudinal direction is 16 cm. The coil has 16 layers and each layer has 20 turns. The coil consists of 500 meters of copper wire with cross-sectional area of 0.53 square centimeters. The solenoid is water cooled when operated, and weights 560 lbs. The

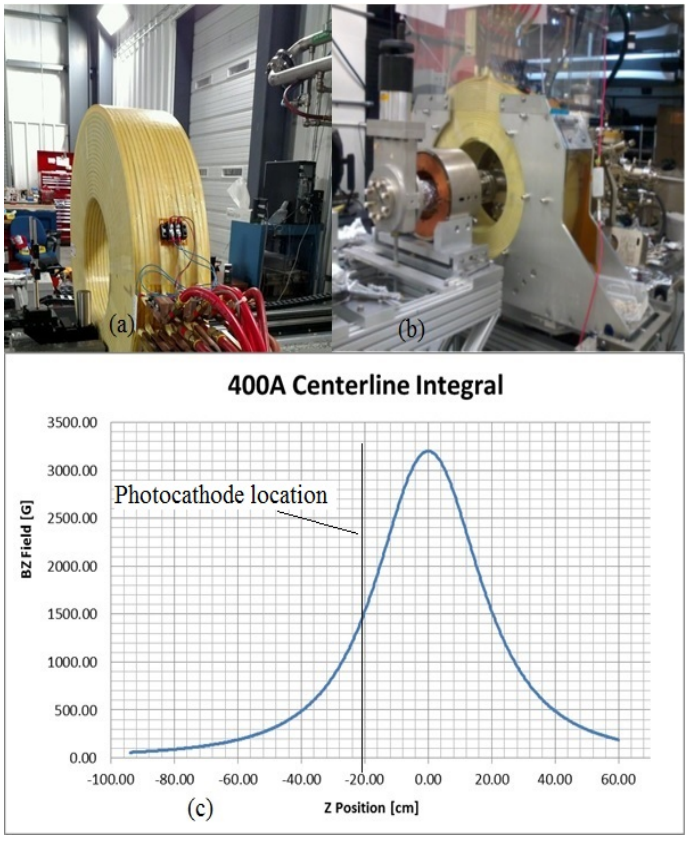

FIG. 27: The gun solenoid and its field map. (a) Before installation. (b) Installed in beamline. (c) Field map along z axis.

gun solenoid uses a spare CEBAF dogleg magnet power supply of 500 A and 80 V. The operating voltage was up to 79 V and current up to 400 A. When the gun solenoid is energized magnetized beam is created. It is de-energized for non-magnetized beam. Figure 27 (c) is the longitudinal magnetic field map along the z axis when operated at 400 A. The distance between the photocathode and the geometric center of the gun solenoid is about 20.3 cm. So the photocathode is immersed in the magnetic field of the solenoid. When the solenoid is energized at 400 A the magnetic field at the photocathode is about 1400 G.

2.5.2 LENSES-SMALL SOLENOID MAGNETS

A solenoid magnet is a tightly wound helical coil of wire whose diameter is small compared to its length. The magnetic field generated in the center is directed along the axis of the solenoid. Outside the solenoid, the magnetic field is far weaker. A solenoid is often used to focus low energy charged particle beams. The focal length f of a thin lens solenoid can be calculated (see Chapter 5) using

$$1/f = (e/2p)^2 \int_{-\infty}^{\infty} B^2 dz$$

with e being the electron charge, p the electron beam momentum, and $\int_{-\infty}^{\infty} B^2 dz$ the longitudinal field integral. There are four solenoid magnet lenses along the beamline. Figure 28 shows the first lens in the beamline and its field on axis when operated at 4 A. The windings are in metal housings as shown in the picture. The housing confines the field so that it will not extend much at both ends. In this research the first lens is used to measure the beam emittance by varying the strength of the lens and measuring the corresponding beam sizes downstream using beam profiling diagnostics.

2.5.3 STEERING MAGNETS

When an electron beam comes out the photogun it may not travel in the direction desired. The earth's magnetic field is strong enough to deflect the electron beam. Steering magnets, commonly called correctors, are needed to make corrections. Nine pairs of steering magnets are for the angular correction of the beam orbit. Two pairs are air-core magnets, and seven are iron-core ones. The correctors only make minor corrections of the beam trajectory. They do not change the beam properties, such as beam emittance, energy spread, etc., significantly.

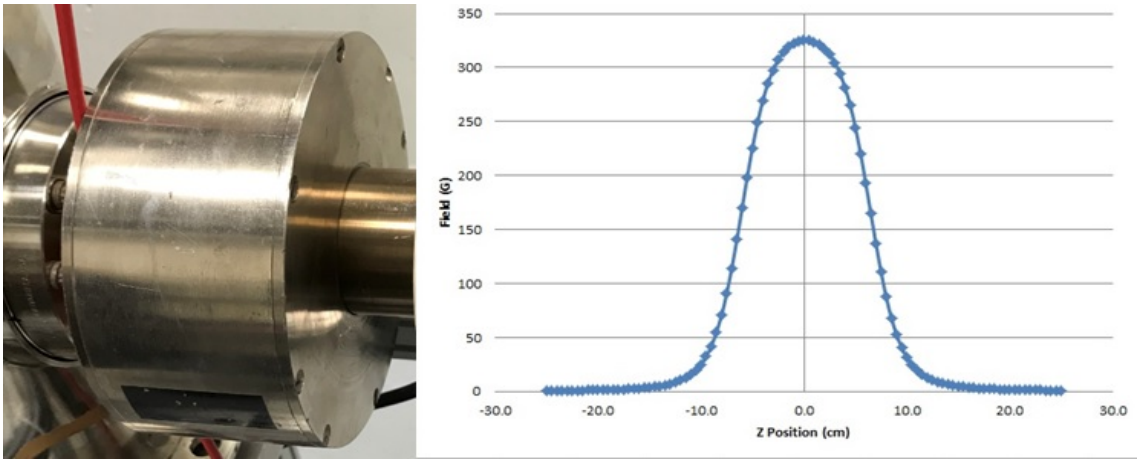

FIG. 28: Left: A lens installed in beamline. Right: Its field on axis at 4 A.

Air-core steering magnet

There are two BH (Jefferson Lab type designation) steering magnets manufactured by Haimson Research as shown in Figure 29. Each magnet is made of 100 turns #24 AWG copper magnet wire. Two diametrically opposed inner coils (Model 334) mounted on the surface of a 6.35-cm diameter beamline provide a transverse magnetic field, say, in the x direction; and two diametrically opposed outer coils (Model 335) mounted on the 8.23-cm outer diameter of the inner coils provide an orthogonally oriented transverse magnetic field

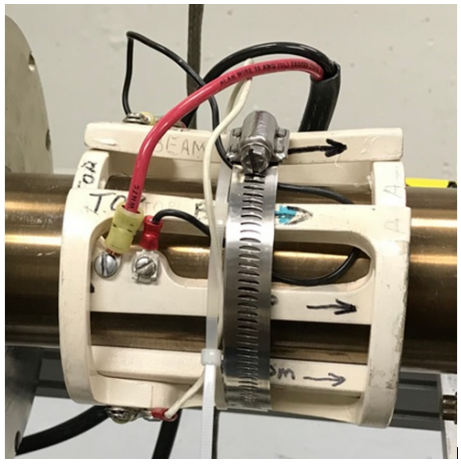

FIG. 29: Haimson steering magnets installed in the beamline.

in the y direction. The characteristics of these magnetic dipole steering coils are defined as follows: with the 200 mA rated current flowing in series through each pair of dipole coils (connected so as to provide boosting, rather than bucking magnetic fields), the transverse momentum imparted to a traversing 100 keV electron will result in angular deflections of 33 mrad in the x direction and 29 mrad in the y direction. The maximum operating current is 1000 mA.

Iron-core steering magnet

There are seven iron-core steering magnets made by Radiabeam installed on the beamline. The coils are directly wrapped on nickel-plated steel yokes and then impregnated with epoxy. The design lends itself to traditional base mounting while optional clamps allow the magnet to be mounted directly to the beamline. The picture below is the transverse magnetic field map of the magnet on axis. The integrated field is 401 G cm with the peak field of 31.6 G. The maximum current per axis is 3.4 A with fixed voltage of 0.5 V. The physical length is 2.8 cm with transverse size of 16.3 x 14.2 cm and bore of 8.6 cm. The calibration is 118 G cm/A. With 100 keV electron beam and 200 mA current the deflection angle is about 37 mrad in both x and y planes. Figure 30 shows the magnet and its field profile. Usually an iron-core corrector is stronger than an air-core corrector.

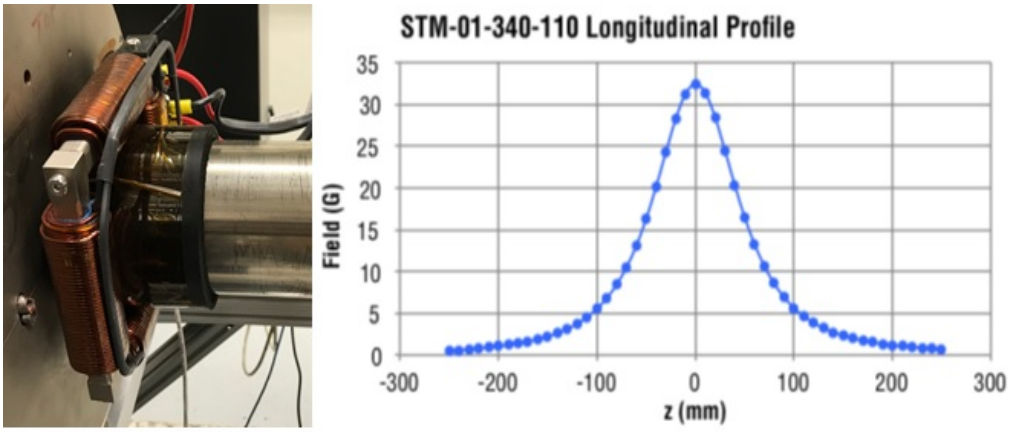

FIG. 30: Left: An iron core steering magnet installed in the beamline. Right: Its field profile.

2.5.4 WIRE SCANNER

A wire scanner, also commonly called a harp, consists of three mounted thin round wires which are passed in a controlled manner through the electron beam. The harp is driven by a stepping motor. A linear potentiometer position measurement system is used and the device has a limit switch at both ends to protect the driving mechanism. As the wire intercepts the beam a current is generated. The beam-induced current, as a function of wire position, produce a functional $x - y$ plot with a peak being produced when the wire is in contact with the beam. The measured current as a function of position yields the current profile of the beam. Then the beam size can be extracted from the measured data. It is assumed that the signal response will be proportional to the portion of the beam that is intercepted by the wire. For fitting the data, the electron beam is assumed to have a Gaussian profile.

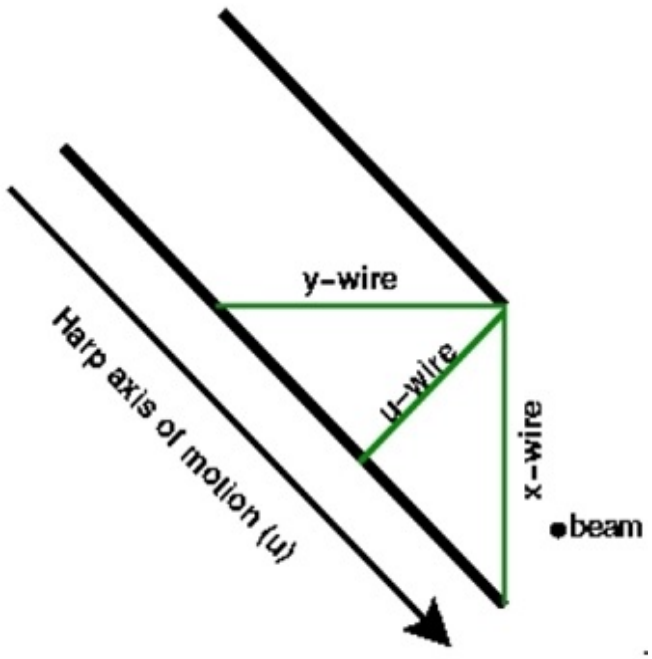

FIG. 31: A wire scanner has three tungsten wires of diameter of 20 μm.

Note that the wire diameter of 20 μm is much smaller than the measured beam size, and as such the signal response represents a sampling of the beam distribution. In order to measure distinct two or three one-dimensional beam profiles, the wire scanners use two or three wires with different orientations employed on the mounting fork. The GTS wire scanner employs

a horizontal (x), 45 degree (u), and vertical (y) wire on a motion mechanism that has a 45 degree orientation with respect to the accelerator reference frame as shown in Figure 31. When the wire scanner fork moves with velocity, v, the velocities of the x and y wires in the accelerator reference frame are $v \cos 45°$. The use of wire scanners to measure the beam size is common in electron accelerators. To trigger a measurement a real-time clock is used from the beam synchronized source for pulse mode operation or a free-running oscillator source for CW beam mode measurements. The clock is also software programmable. The mounting fork should be metal so that it can be vacuum baked.

Wire scanners provide a simple and yet reliable way to measure the size and position of an electron beam. They are invasive devices; during the measurements the beam is interrupted. The beam current range could be from a few nA to a few dozen μA. At Jefferson Lab wire scanners are used to measure the size of the electron beam in the main accelerator.

2.5.5 VIEWERS AND CAMERAS

As shown in Figure 32, viewers are another type of invasive diagnostic device installed in the beamline which can be used to measure the beam profile and position. A viewer consists of a viewer screen which fluoresces when struck by an electron beam, a mirror, and an optical camera. The viewer screen is inserted into the beam path and glows at the location where the electrons hit it. The screen is made of yttrium aluminum garnet (YAG) single crystals of 0.1 mm thickness. It is mounted on a round metal frame of 50.8 mm diameter. Behind the viewer screen is the mirror attached to the frame forming a 45 degree angle with the viewer screen. The incoming beam is perpendicular to the viewer screen. The mirror guides the light from the viewer screen to the camera outside the beam pipe through a view port. The screen is inserted by an air piston which is part of the mechanical assembly attached to the beam pipe. Figure 33 shows how a viewer works. There are three viewers installed in the beamline. An optical camera is used to image the viewer screen. The cameras for the first two viewers do not have a trigger. The camera for the third viewer has a trigger so it is synchronized with beam.

Usually when using a viewer one has to make sure the power is low as intense beam could saturate the viewer and the measurement would not be accurate. Also beams will melt a viewer if the power exceeds the viewer power limit.

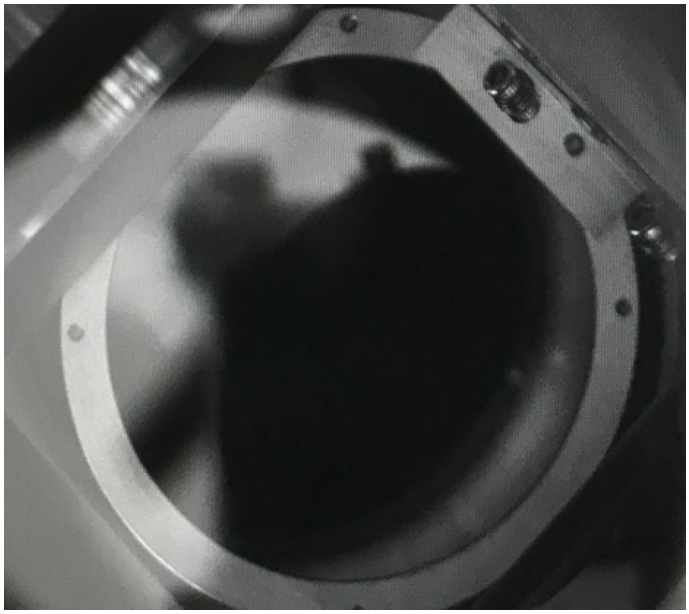

FIG. 32: A viewer in the GTS beamline.

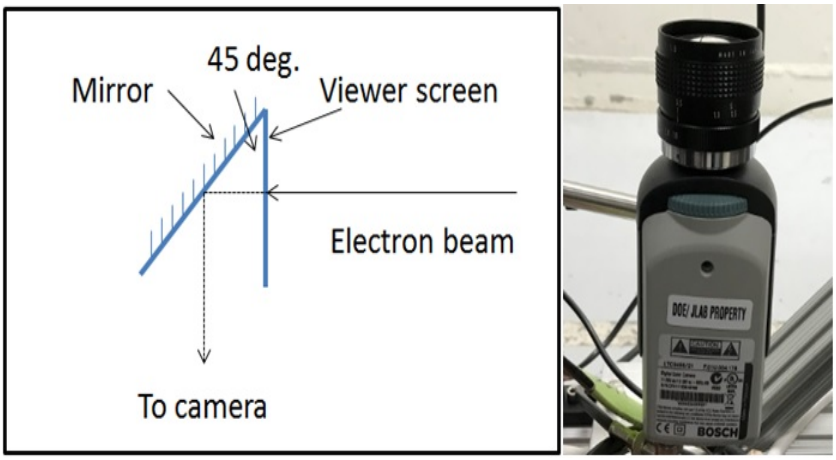

FIG. 33: Schematics of viewer system and camera used in GTS.

2.5.6 FARADAY CUP AND BEAM DUMP

One Faraday cup, as shown in Figure 34, and one beam dump, as shown in Figure 35, are on the beamline. The Faraday cup and beam dump are the beam termination points. Both are electrically isolated so the beam current can be measured when the beam is delivered

to the Faraday cup or the beam dump. The Faraday cup is installed in the middle of the beamline and retractable. The beam dump is at the end of the beamline and fixed. Both are cooled using low conductivity water (LCW). The rated power of the Faraday cup is 200 W and that of the dump is 2.5 kW. The dump can accept up to 8 mA CW beam if the beam energy is 300 keV. Figure 36 show the schematics of the Faraday cup and the dump.

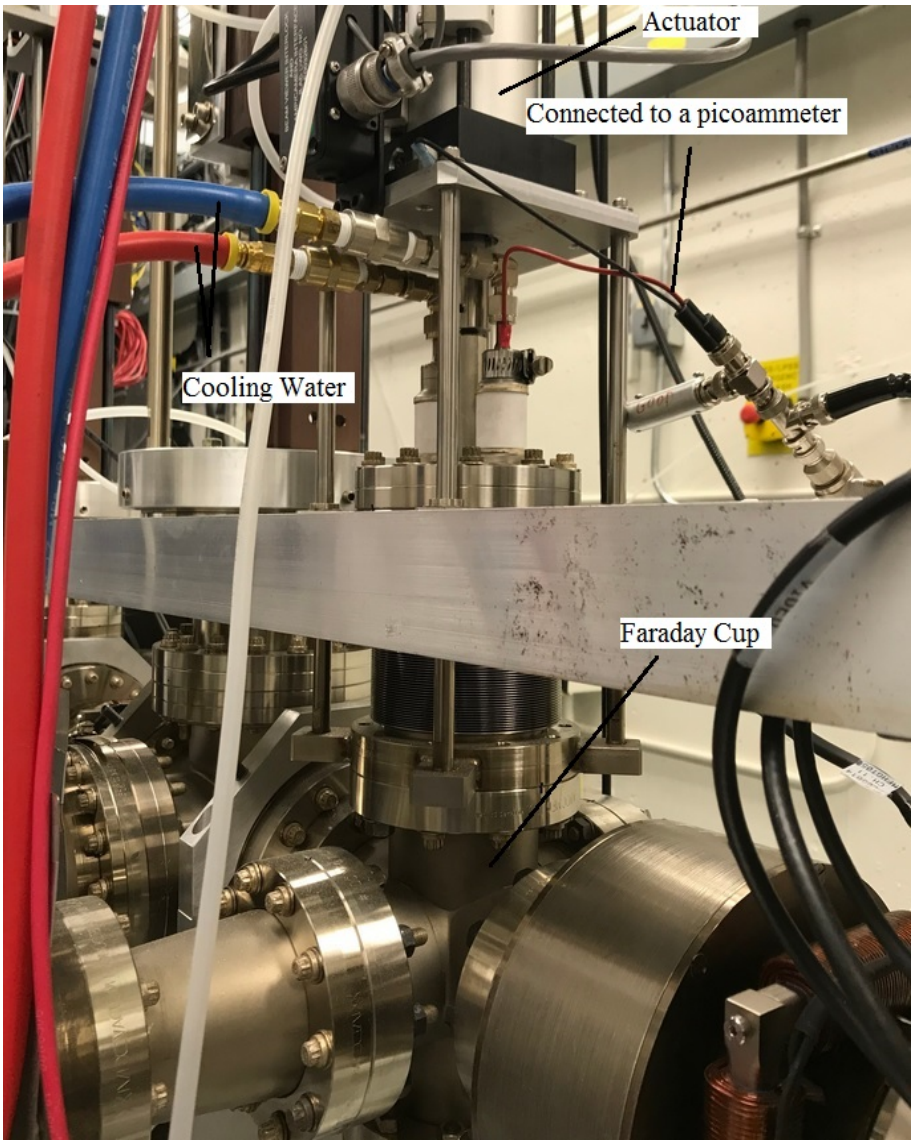

FIG. 34: A Faraday cup installed in the beamline.

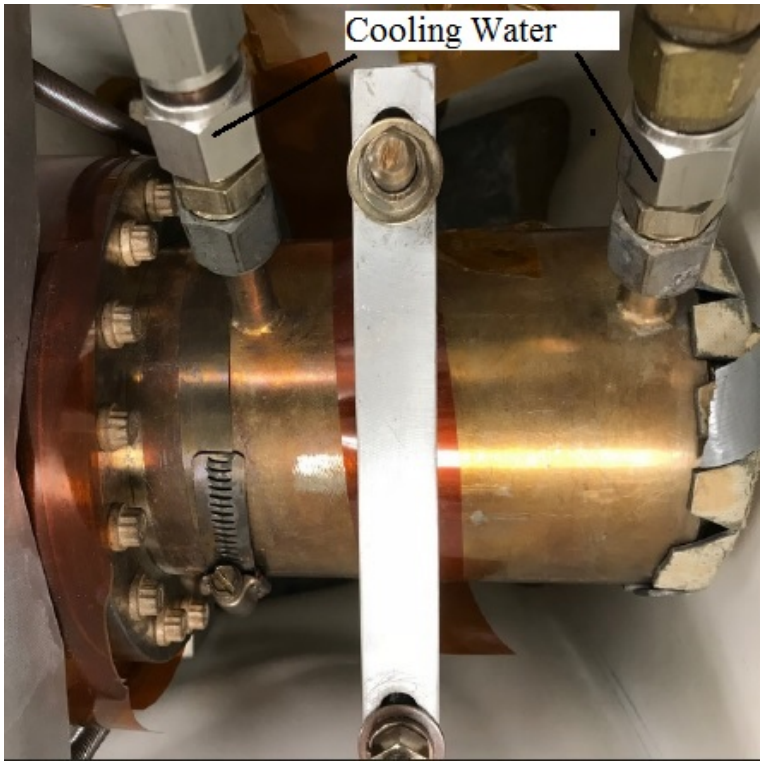

FIG. 35: A beam dump installed at the end of the beamline.

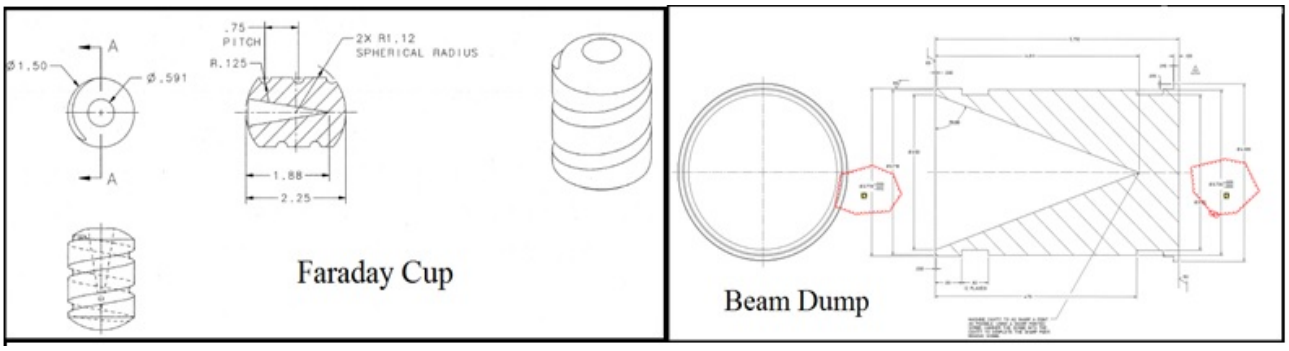

FIG. 36: Schematics of Faraday cup and beam dump.

CHAPTER 3

DESIGN AND PERFORMANCE OF THE HIGH VOLTAGE PHOTOGUN

High voltage DC photoguns are utilized for a variety of basic research and industrial applications. Guns of older design are either bulky or the voltage is still relatively low. This research aims to build a compact -300 kV DC photogun that will be reliable, have a long lifetime with no or minimal field emission, and deliver high quality electron beam. Based on the desired voltage, the new design involves the size and shape of the gun vacuum chamber and the cathode electrode, and the way that the high voltage is applied to the cathode electrode.

The size and shape of the chamber and electrode affect the electric potential and field inside the gun chamber. Because the gun chamber is electrically grounded, when the high-voltage electrode is biased there is a very steep potential drop. This poses a design challenge. Past experience indicates that no breakdowns occur if the static electric field inside the gun chamber is about 10 MV/m or lower. If the electric field exceeds this approximate threshold electrical breakdown is likely to happen. A good photogun should have no or minimal uncontrolled field emission, as field emission shortens the photocathode lifetime because the field-emission generated ions hit the photocathode and cause damage.

A compact DC high voltage photogun with inverted-insulator geometry was designed, built, and operated reliably at -300 kV bias voltage using alkali-antimonide photocathodes. Figure 37 (a) shows the new design of a -300 kV DC gun. High voltage is applied to the cathode electrode using a cable, which does not require an SF_6 tank at the photogun to suppress corona discharge. An inverted-insulator geometry is used for connection of the cathode electrode to the high voltage cable. The design advantages include compact size with relatively small surface area compared to the photogun designs that employ large cylindrical insulators, which is good from a vacuum perspective. Because the insulator supports the cathode electrode, there is less metal biased at high voltage, which serves to minimize field emission. Figure 37 (b) shows the old design with a large insulator stack and long metal rod for high voltage connection for comparison.

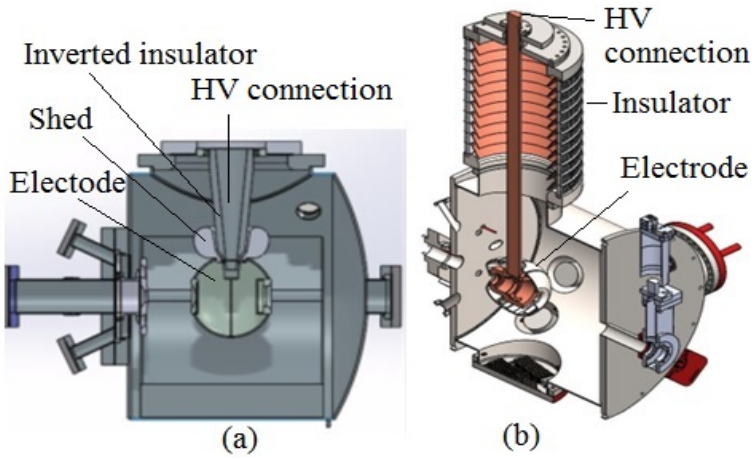

FIG. 37: Gun designs. (a) New inverted insulator geometry. (b) Old gun design. Note: not to scale.

3.1 POISSON AND GPT SIMULATION

Simply put, a photogun has a grounded gun vacuum chamber with a cathode electrode inside. To reduce the peak surface electric field due to enhancement at corners the cathode should be spherical. Figure 38 shows a section view of simplified photogun with a spherical shape and a cubic shape. Software simulations were used to quantitatively study the strength and distribution of the electric field and potential inside the photogun vacuum chamber.

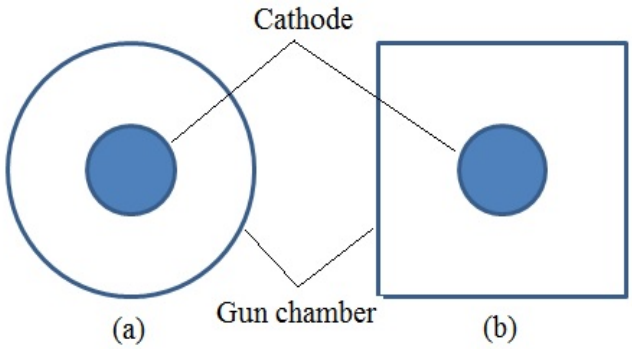

FIG. 38: A gun chamber with cathode. (a) Spherical shape. (b) Cubic shape.

POISSON-SUPERFISH models were created to model and calculate the electric field and potential distributions. Because of symmetry, a 2D model can be used for calculations. From

Figure 39, the three-dimension results can be visualized by rotating around the vertical axis 360 degrees. Figure 39 shows calculation of just a cathode electrode inside the photogun vacuum chamber. In Figure 39 (a), both the cathode (15.24 cm diameter) and chamber (36 cm diameter) are spherical. In Figure 39 (b), the cathode is spherical (diameter 15.24 cm) and the chamber is cubic (36 × 36 × 36 cm). The arrows present the direction and strength of the electric field. The lines between the cathode and chamber are the surfaces of constant electric potential.

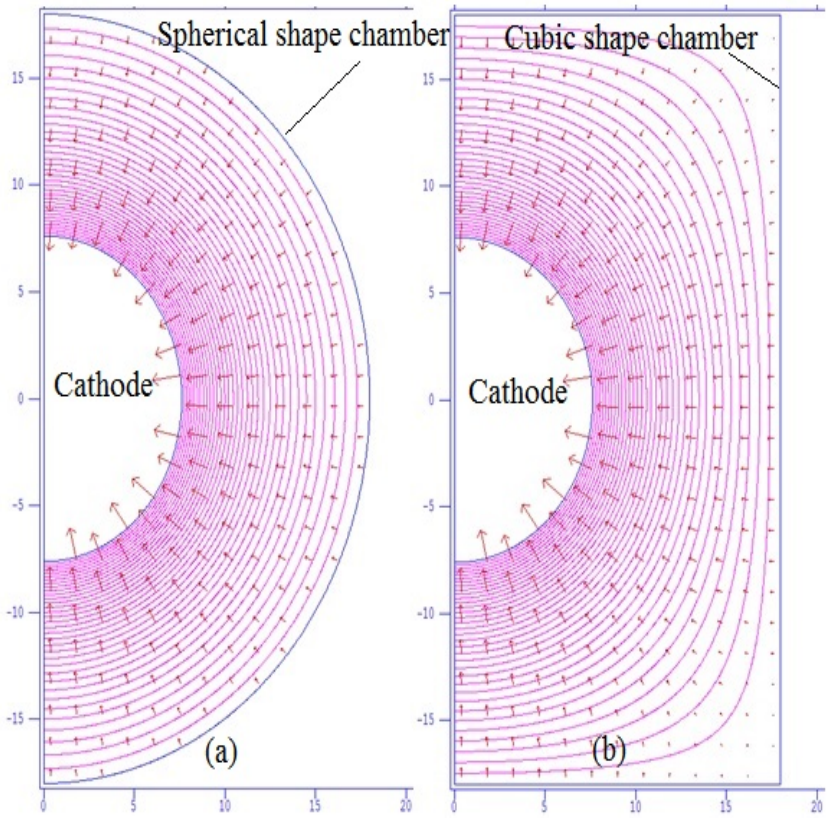

FIG. 39: A spherically shaped chamber (a) (36 cm diameter) and a cubic shaped chamber (b) (36 × 36 × 36 cm) have identical field and potential distributions in the acceleration region. The cathode diameter is 15.24 cm.

From physics point of view, a cubic shaped chamber and a spherically shaped chamber have identical distributions of the electric field and potential around the cathode location. At corners of the cube the field and potential distributions are different but not in the region electrons are accelerated.

From engineering point of view it is not easy to make a spherically shaped chamber. Figure 40 shows the shape of the photogun chamber used in this research. It is cylindrical with a diameter of 46 cm and a length of 36 cm. It is easy to make a spherical shaped cathode electrode. Figure 18 (d) on page 20 shows the cathode electrode used in this research.

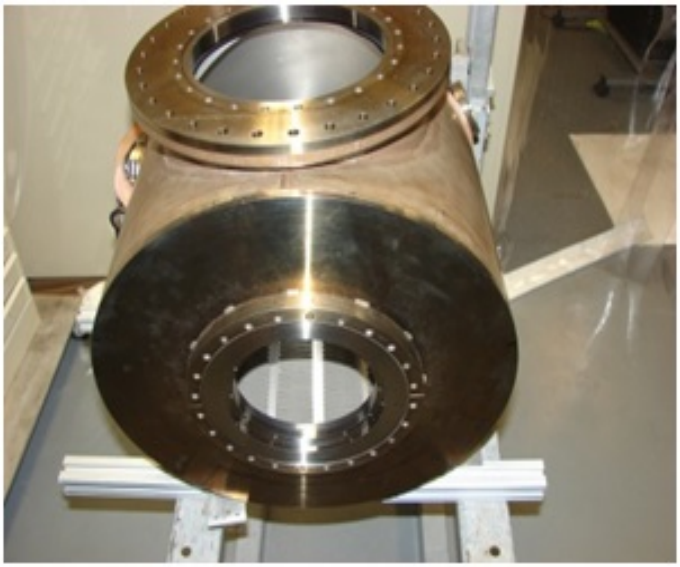

FIG. 40: A cylindrically shaped gun chamber with diameter of 46 cm and length of 36 cm.

Given the shape and dimensions described above, Table 1 shows the highest field obtained from POISSON simulation in the chamber when the cathode electrode is biased to -300 kV. Inside the cathode electrode the electric field is zero. The highest field is outside the electrode but near its surface.

Table 1 shows that when the electrode is biased to -400 kV the maximum field in the gun is 9.07 MV/m and when the voltage is -300 kV the highest field is only 6.80 MV/m. As discussed previously, a design goal is to keep the field below 10 MV/m. However the calculation shown above is an ideal case because it does not consider how the high voltage is applied to the electrode and the anode plate is not included. Also the shape of the electrode needs to be modified to accommodate the photocathode. As next level of detail, include the insulator and the anode plate in the gun chamber as shown in Figure 14 on page 17. Also, the high voltage cable can plug into the insulator from the air side as shown in Figure 4 on page 9. The new way to use the insulator is different from the old way as shown in Figure 37 (b) on page 35. The new design applies the high voltage to the electrode from the air side in an inverted-insulator geometry.

TABLE 1: Maximum electric fields at electrode surface with different bias voltages.

V (kV)	-300	-350	-400
E (MV/m)	6.80	7.96	9.07

Figure 41 (a) shows the calculation result with the insulator, high voltage cable, and anode installed in the gun chamber. To simplify the simulation, a 2D model is used, rotationally symmetrical about a vertical axis along the biasing wire. Figure 41 (b) shows the electric potential lines, and the electric field at several points of interest. The region closer

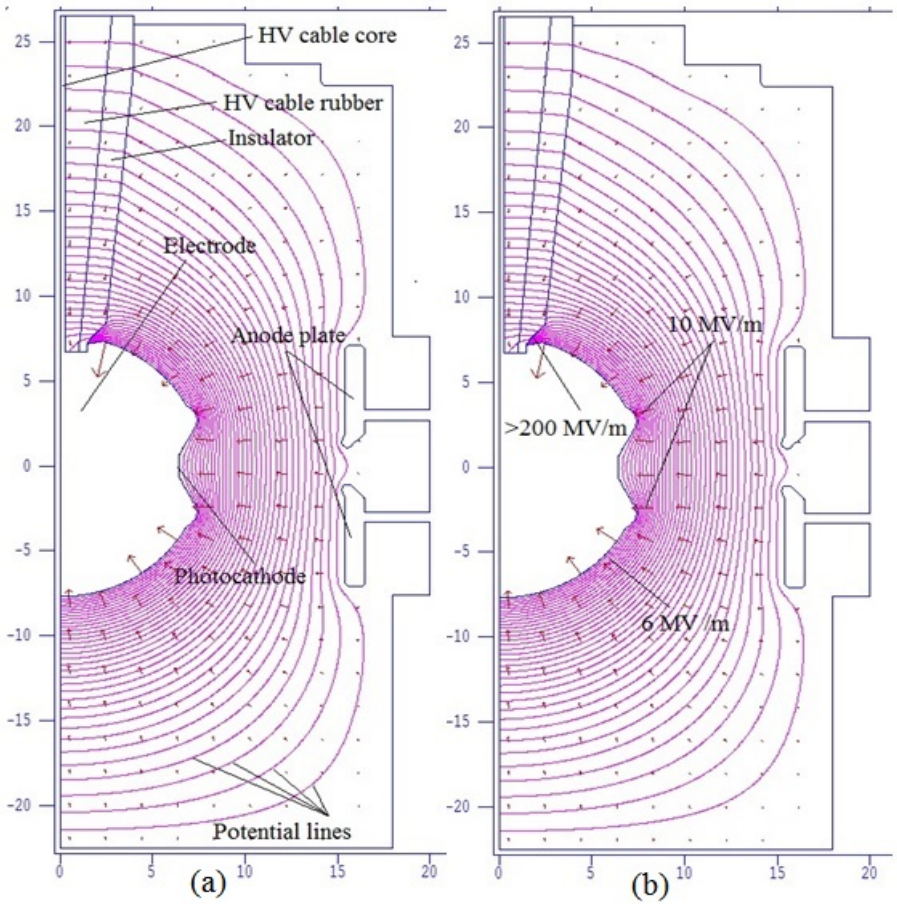

FIG. 41: Distribution of he electric field and potential inside the gun chamber. (a) The HV cable, cable rubber, insulator, anode, and photocathode, potential lines. (b) The field strength at different locations when gun is biased at -300 kV.

to the surface of the electrode has stronger electric field. In particular, the fields at the triple-point-junction (ceramic-electrode-vacuum interface), the front face of the electrode, and the surface of the electrode are 200 MV/m, 10 MV/m, and 6 MV/m, respectively. The field at the triple-point-junction is much larger than elsewhere; breakdowns are expected to be much more likely to occur in this region than elsewhere. Also, in the past insulators were damaged in this region, from field emission driven by the high field. In Figure 41 one can also see that the potential lines along the insulator surface are not evenly spaced. This means that the potential drop along the insulator is not linear and thus the electric field not uniform.

To increase resistance to breakdown, the field at the triple-point-junction must be reduced. A metal shed as shown in Figure 19 on page 21 was designed and installed between the insulator and electrode. Figure 42 shows the POISSON simulation result with the shed

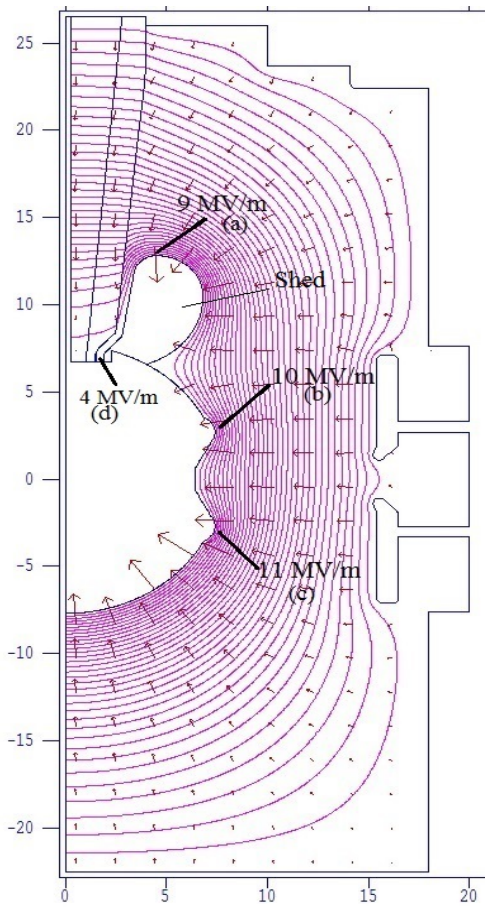

FIG. 42: Simulation at -300 kV with a protective shed.

installed. Due to the installation of the shed, the electric field symmetry between the photocathode and anode may be slightly affected. If the field symmetry in this acceleration region is affected too much the electron beam may not be able to go through the anode. This possibility was checked via GPT and shown to be manageable experimentally.

In Figure 42, a 2D calculation of the field is presented. The field at the cathode front face varies because of the symmetry-breaking from the insulator and shed. The field at the top of the cathode is 10 MV/m, the field at the bottom is 11 MV/m. Figure 43 shows the electric fields around the shed and the triple-point junction. The shed lowers the field at the triple-point region from 200 MV/m to 4 MV/m at -300 kV. Table 2 shows the fields at point (a), (b), (c), and (d) in Figure 42 at -300 kV and -350 kV. With the addition of the shed to the design, the electric field are reduced to below 10 MV/m everywhere outside of the photocathode region.

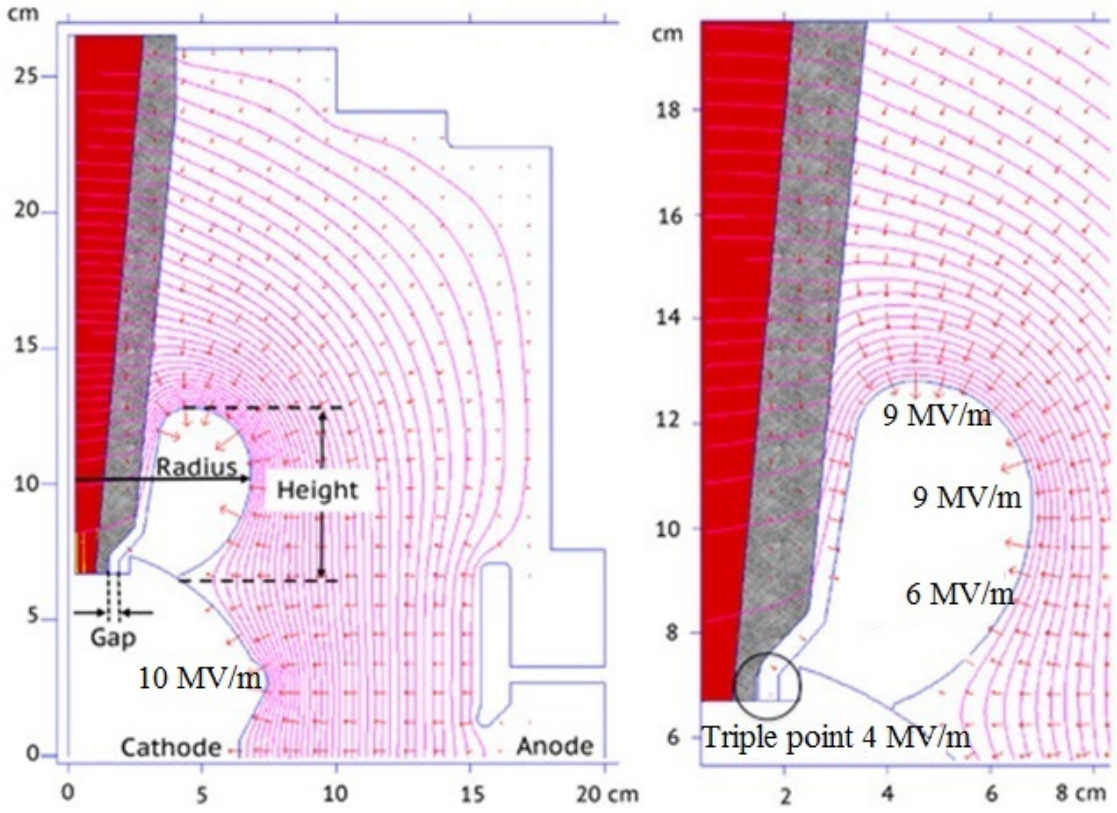

FIG. 43: A closer look at fields near shed and triple-point junction stimulation at -300 kV. The shed dimensions: gap = 0.4 cm, height = 6.3 cm, radius = 6.8 cm.

TABLE 2: Fields at different bias voltages.

V (kV)	-300	-350
E (MV/m) at (a)	9.0	10.0
E (MV/m) at (b)	10.0	12.0
E (MV/m) at (c)	11.0	12.5
E (MV/m) at (d)	4.0	4.5

POISSON [5] generates a field map of the gun model. The gun field map then is then fed to the General Particle Tracking (GPT) [6] simulation tool to check the electron beam trajectory. Figure 44 shows the simulation results.

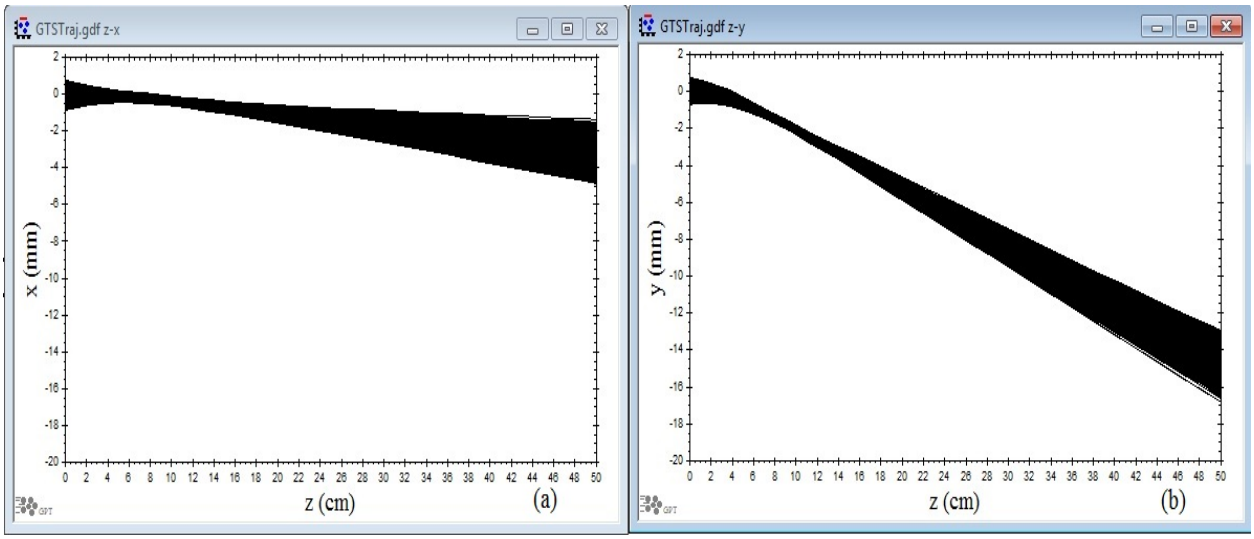

FIG. 44: A GPT simulation indicates both x and y trajectories are affected by the gun field. (a) x orbit displaced -3 mm at $z = 50$ cm. (b) y orbit displaced -14 mm at $z = 50$ cm.

In this simulation the gun is biased to -300 kV and no other beamline element is used, i.e., correctors and lenses are off. The simulation z range is 50 cm, the anode is located at $z = 9$ cm. The x orbit is displaced -0.3 mm and the y orbit -1.5 mm there. The opening on the anode plate has a diameter of 20 mm; so the electron beam will traverse the anode and exit the gun chamber. If not corrected the x orbit would be displaced -3 mm and the y orbit -15 mm when beam travels 50 cm. There is a pair of correctors right at the gun exit. The broken symmetry has no significant impact on beam transport and beam quality.

Given the geometry of the insulator, shed, and NEG pumps, the electric field symmetry in both x and y planes should be affected as one can see in Figures 45 and 46. Figure 45 (left) shows the insulator and shed affect the electric field symmetry in y plane. Figure 45 (right) shows installation of the NEG pump was not symmetric at the bottom of the gun chamber. The asymmetric installation is due to the fact that the NEG activation feedthrough is in the way. Figure 46 is the GTS gun field map indicating the electric field asymmetry in both x and y planes.

One can add another metal piece at the bottom of the cathode electrode to compensate for the electric field change caused by the insulator and shed. Figure 47 shows that the added metal piece corrects this asymmetry issue in the acceleration region. The potential line distribution near the dotted line is symmetric, which means that the electric fields in the region are symmetric. Such a correction was not implemented in this gun but may be deployed in future guns.

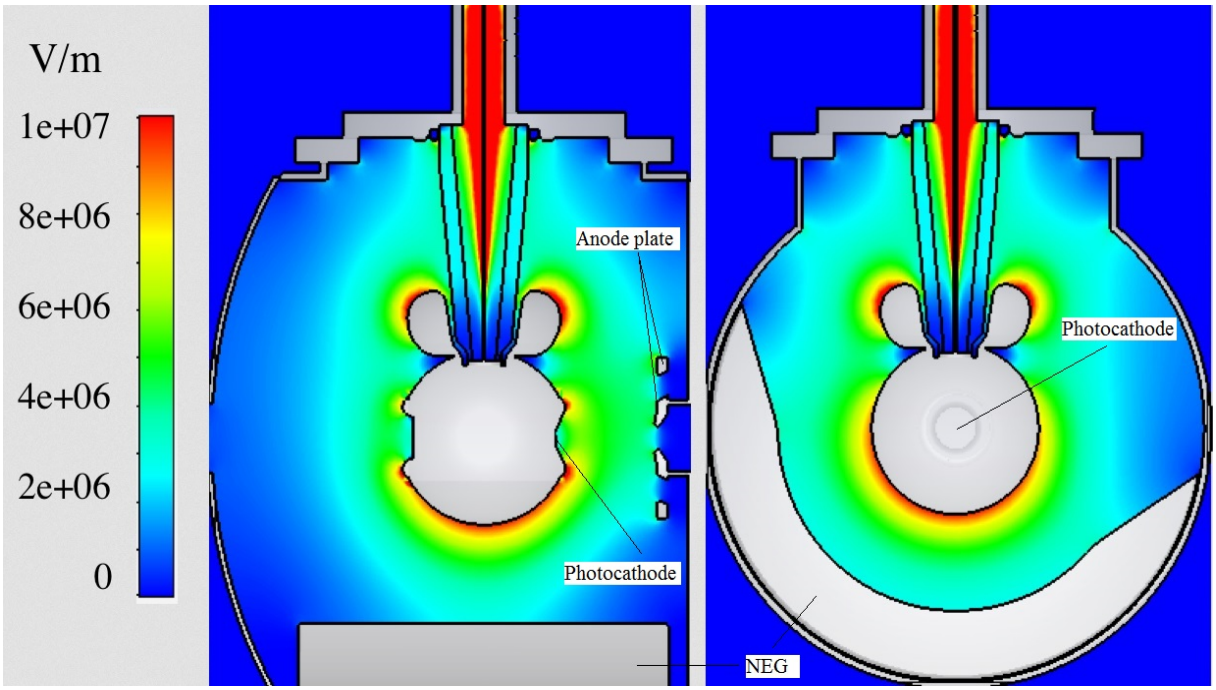

FIG. 45: Left: The shed affects the field symmetry in y plane. Right: The NEG affects the field symmetry in x plane (courtesy of Gabriel Palacios).

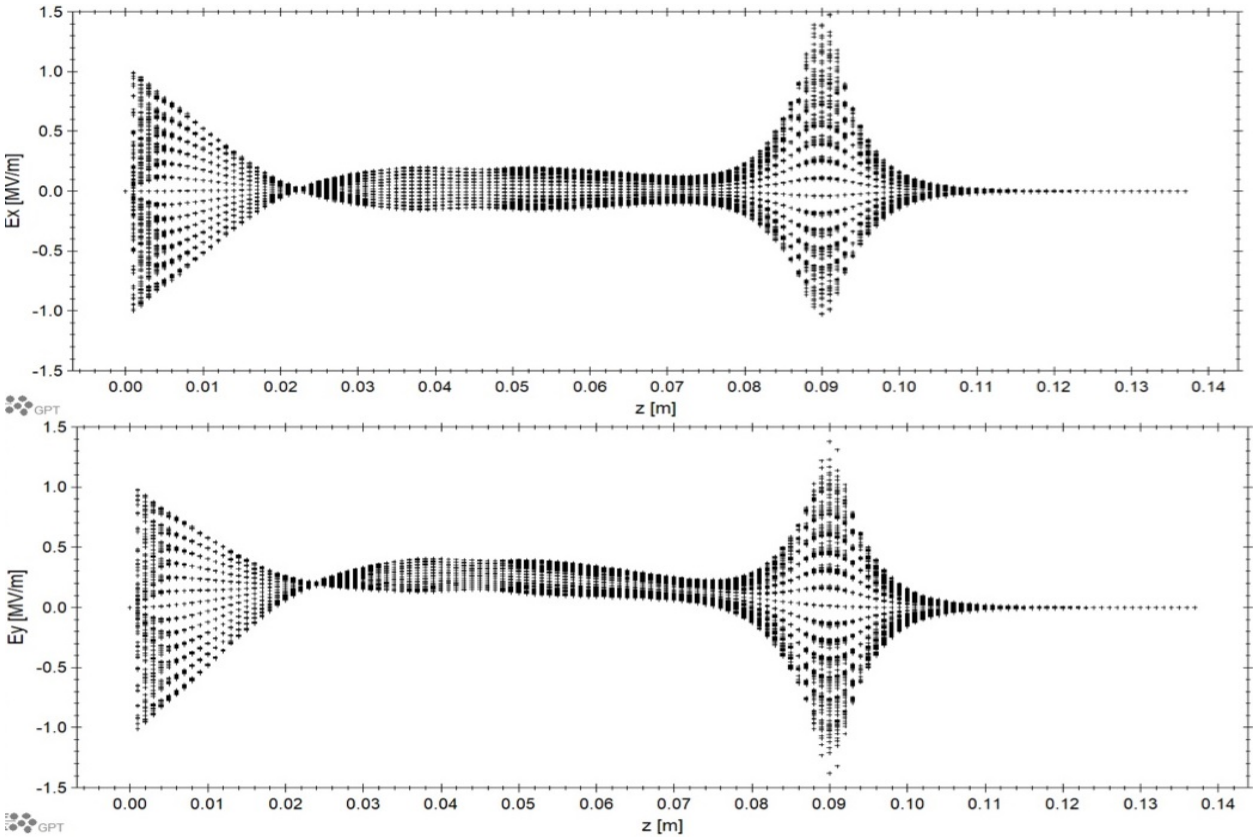

FIG. 46: GTS gun field map: Top: Electric field in x plane. Bottom: Electric field in y plane.

The shed by design improves the linearity of the potential drop along the insulator surface. Figure 48 show the comparison of the potential drops with and without the shed. Therefore the electric field is more uniform along the insulator surface and the insulator is not so greatly stressed. During tests prior to this work insulators were damaged, likely due to the fact that the potential drop was not linear, leading to excessive electric fields in the insulator regions.

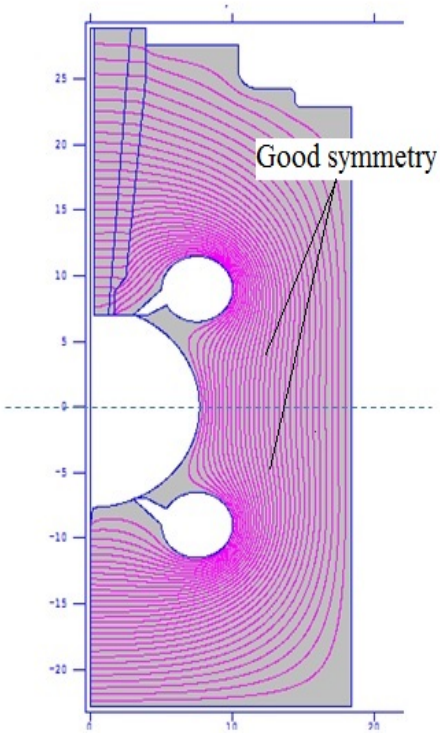

FIG. 47: A metal piece on bottom of the electrode corrects the field symmetry problem. The potential lines near the dotted line which is the acceleration region indicates that the electric fields in the region are symmetric.

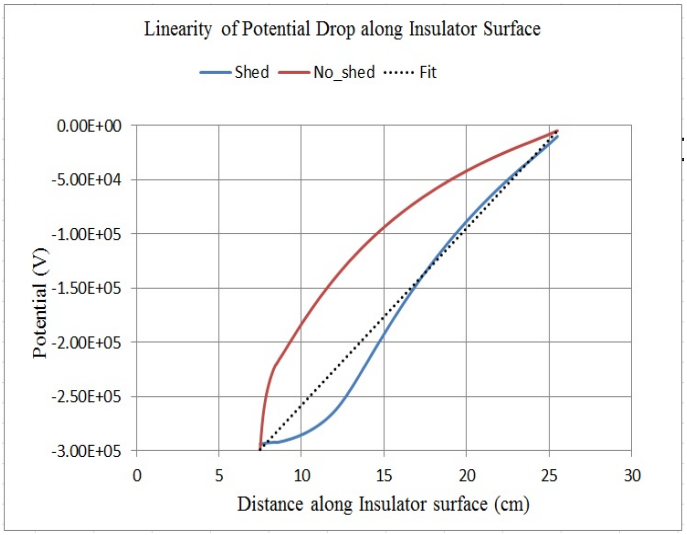

FIG. 48: The shed improves the linearity of potential drop along insulator surface.

3.2 BARREL POLISHING

All parts in the photogun chamber, especially the parts biased to high voltage, must be surface polished to reduce field emission. The photogun chamber interior surface does not have to be polished to mirror like conditions because the electric field is lower there and the field pushes electrons into the metal.

The centrifugal barrel-polishing machine was used to polish the cathode electrode, the shed, and their associated parts [7]. It employs plastic barrels filled with dry polishing media, in which the electrode was immersed. The machine used at Jefferson Lab holds up to four barrels that are attached to a spinning drum as shown in Figure 49. Viewed from the side, the configuration looks like a Ferris wheel. As the drum rotates in one direction, the barrels rotate in the opposite direction, which causes the media and parts to rub against one another randomly and repeatedly. The barrel-polishing technique reduced polishing time from weeks to hours while providing surface roughness comparable to that obtained with diamond-paste polishing. The time depends on electrode size and mass, which are important

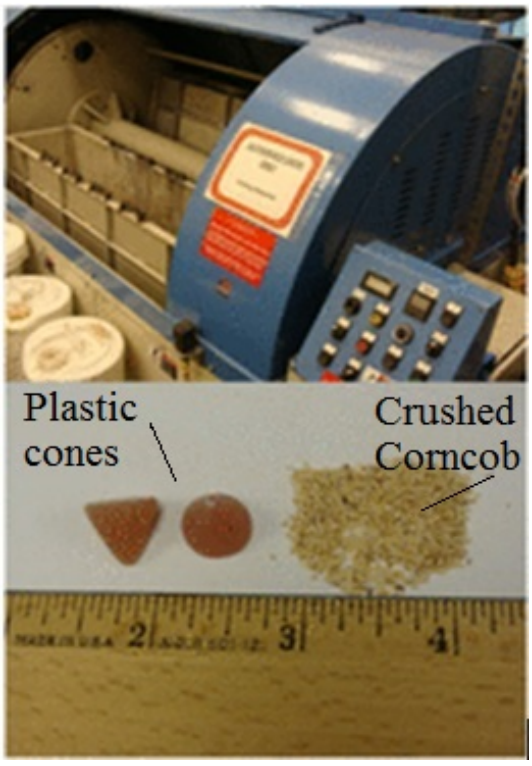

FIG. 49: The barrel polishing machine was used to polish the gun parts.

factors in the polishing process. Two types of polishing media were suggested by the vendor: plastic cones and crushed corncob. To prevent cross contamination from the residue, each media had its own barrel. Between polishing intervals, the part was wiped clean with lint-free tissue soaked in 2-propanol prior to immersion in the fresh media-filled barrel. All the parts were vacuum degassed at 900 °C before polishing.

After polishing, the surface finish was evaluated by measuring the roughness average (Ra) using two non-contact methods: optical profilometry with a Veeco WYKO NT1100 optical profiling system and atomic force microscopy (AFM) with a Nanoscope Dimension 3100. The roughness average (Ra) represents the average of all peak and valley deviations from a centerline across a sampling line. Each part was manufactured with 32 finish specification, meaning 32 micro-inches roughness average surface finish, equivalent to 0.8 μm. After barrel polishing the roughness average is better than 100 nm. The centrifugal barrel polishing with plastic cones and corncob media provides a mirror-like surface finish in hours, comparable to the surface finish attained with diamond-paste polishing.

3.3 PHOTOGUN ASSEMBLY

After manufacturing and vacuum degas at 900 °C, each electrode was barrel polished and finally cleaned in an ultrasonic bath of 2-propanol. The ceramic was thoroughly cleaned using lint-free wipes soaked in 2-propanol. The photogun was fully assembled in a class 1000 clean room. High pressure rinsing was not used on the electrodes. Instead the insulator-electrode assembly was additionally cleaned using a CO_2 jet nozzle just prior to being integrated to the photogun vacuum chamber to minimize the amount of dust particulates. After assembly, the photogun was moved to a radiation shielded test enclosure and vacuum baked at 200 °C until the pressure change was less than 10% in 24 h. The NEG modules were activated at 450 °C for 45 minutes at the end of the bake with the resulting vacuum in the low 10^{-11} Torr range.

3.4 GUN HV CONDITIONING WITH KRYPTON

Before a DC high voltage photogun can be used as an electron source, the electrodes must be high voltage conditioned [8] to eliminate field emission which can lead to catastrophic damage to the photogun when encountered at high levels.

Three signals related to field emission were monitored during conditioning: field emission current, photogun vacuum levels, and electron bremsstrahlung x-ray radiation levels. Ideally field emission current should be monitored with a floating ammeter in series with the

conditioning resistor, but this configuration could not be easily implemented. Instead, field emission current was monitored as excess current from the power supply measuring stack, above background levels that were benchmarked with the HVPS as a standalone system. The conditioning resistor limits the current that can be delivered in case of breakdown and also protects the electrode via negative feedback as current is drawn by excessive field emission, the voltage drop across the resistor reduces the voltage applied to the electrode. The cathode electrode is not protected from stored energy within the high voltage cable downstream of the conditioning resistor.

Typical field emitters draw currents of tens of μA, but often sudden processing of an emitter tip (emitter burn-off) can result in a current surge up to 5 mA (the capacity of the HVPS). Such events can induce breakdown at the insulator-cable plug, causing serious damage. To address this possibility, the HVPS current-limit was adjusted to trip off at 500 μA. In addition, x-ray dose is measured in counts per second (CPS) by Geiger-Muller tubes (Gamma sensitivity Co60 18 CPS/mR/h) placed around the gun vacuum chamber and the vacuum levels are monitored by the photogun ion pump using a customized controller capable of reading ion current at the pico-Ampere level. These measurements indicate the presence or absence of field emission.

Initially, voltage was increased under vacuum conditions (3×10^{-11} Torr) at a rate of 10 kV/min up to -200 kV, and then in steps of 5 kV at a rate of 1 kV/min when the first vacuum disturbance was encountered at around -225 kV. The x-ray radiation signal tracked the vacuum activity, with both signals indicating field emission. Then the voltage was increased slowly to process out field emitters, with the rate at which the voltage was increased depending on the vacuum level. The procedure was to increase the voltage in steps of 1 kV/min and to let the vacuum recover to 1×10^{-10} Torr before taking the next step, to minimize the risk of developing new field emitters. Prior research indicates that a field emitter is eliminated when the electric field at the nm-size tip is sufficiently high to produce a current density of the order 10^{12} A/m^2, which can slowly melt the tip producing a blunter topography. The high current density can destroy the emitter but also draw current that exceeds the current-limit of the HVPS.

Field emission current levels upon restoring the voltage after a current-limit trip are usually lower, but in some instances higher, reaching hundreds of μA. When this happens, further vacuum high voltage conditioning is not as effective. An efficient complementary conditioning technique is gas high voltage conditioning. Krypton [9] gas is added to the photogun vacuum chamber at pressure about 5×10^{-5} Torr, and then the voltage was

raised from 0 to the last voltage setting reached under vacuum conditions at a rate of 100 kV/min and then more slowly at a rate of 0.5 kV/min. Gas conditioning serves to eliminate stubborn field emitters through ion bombardment. Field-emitted electrons ionize the Kr gas resulting in localized sputtering of the emitter and also suppressing field emission via ion implantation which serves to increase the local work function. When radiation levels decrease to background levels (less than 5 CPS), the voltage was turned off, and the krypton gas pumped away. Voltage could then be applied at a higher value. The photogun was then allowed to soak at high voltage under vacuum conditions for several hours. If more field emitters developed during the soak, gas conditioning was repeated.

As an example, Figure 50 shows some field emitters developed after the gun was biased to -300 kV during a gun high voltage conditioning period. Two radiation monitors indicated that the field emission counts were about 40000 counts per second. The field emitter(s) would not go away on their own. So the gun high voltage was turned off to get ready for the krypton processing. Figure 50 (top) shows the field emission level. Figure 50 (bottom) shows the gun high voltage was at -300 kV and then turned off.

After krypton was introduced into the photogun chamber the gun high voltage was turned on. At first the field emission was going higher as the gun bias voltage went up. One of the radiation monitors indicated the field emission counts were close to 100,000 as shown in Figure 51 (top). When the gun bias voltage was raised to -325 kV the gun high voltage tripped off as shown in Figure 51 (bottom). After the gun high voltage was turned on to -350 kV the field emission counts dropped to the background level. This means that any field emitters were burned off. Prior to gun tripping off the gun current spiked. The gun current spike and field emitter burn-off come together.

The photogun was deemed conditioned at a particular voltage when radiation levels were indistinguishable from background levels. For example, even though the -300 kV target voltage was reached after 60 h, radiation levels were 20 CPS higher than background, indicating that further gas conditioning at higher voltage was required. Figure 52 shows the voltage vs. time for the entire high voltage conditioning process.

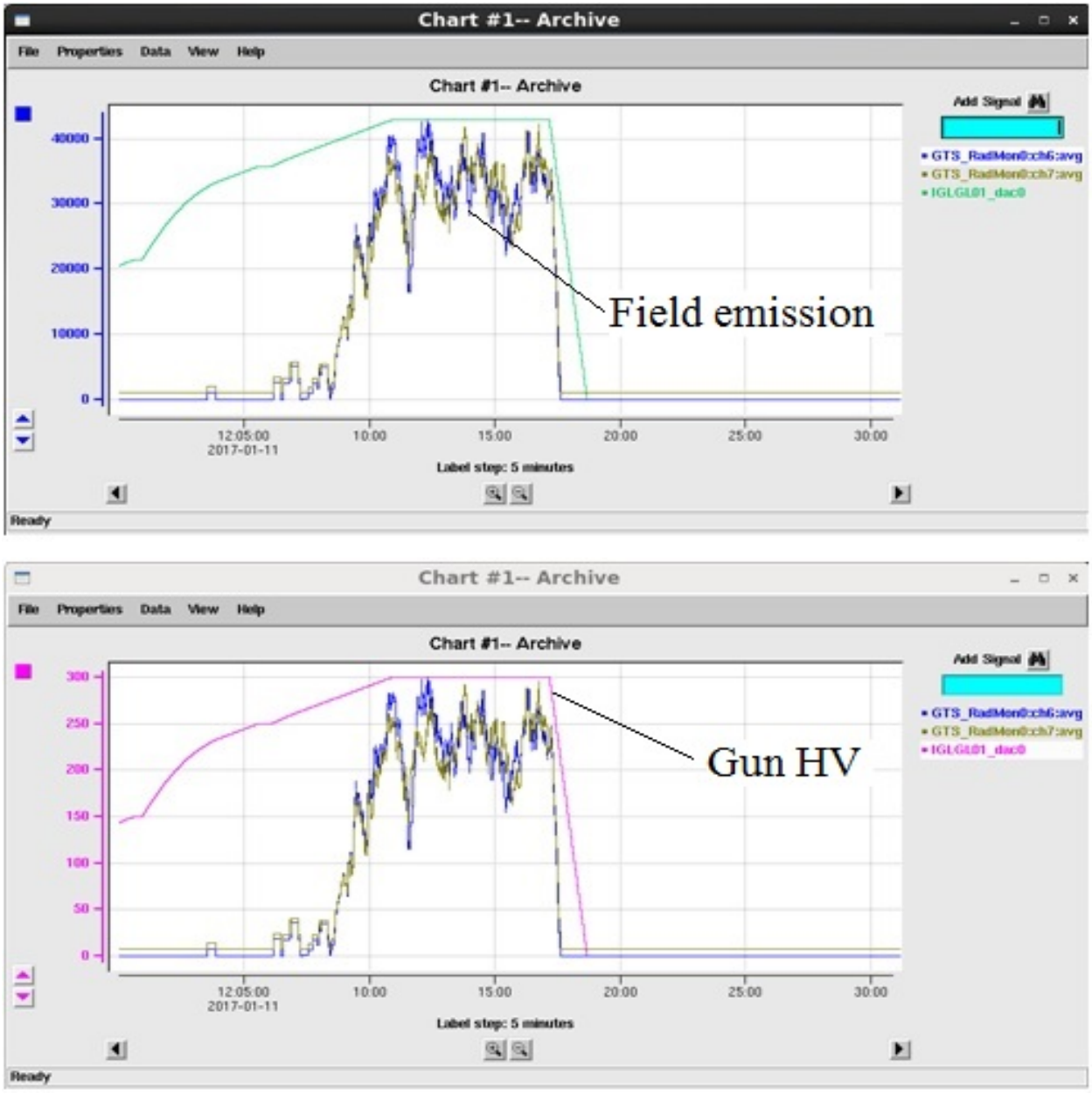

FIG. 50: Field emitters developed after the gun was biased at -300 kV. Top: Field emission counts are about 40000 counts per second. Bottom: Gun is biased at -300 kV.

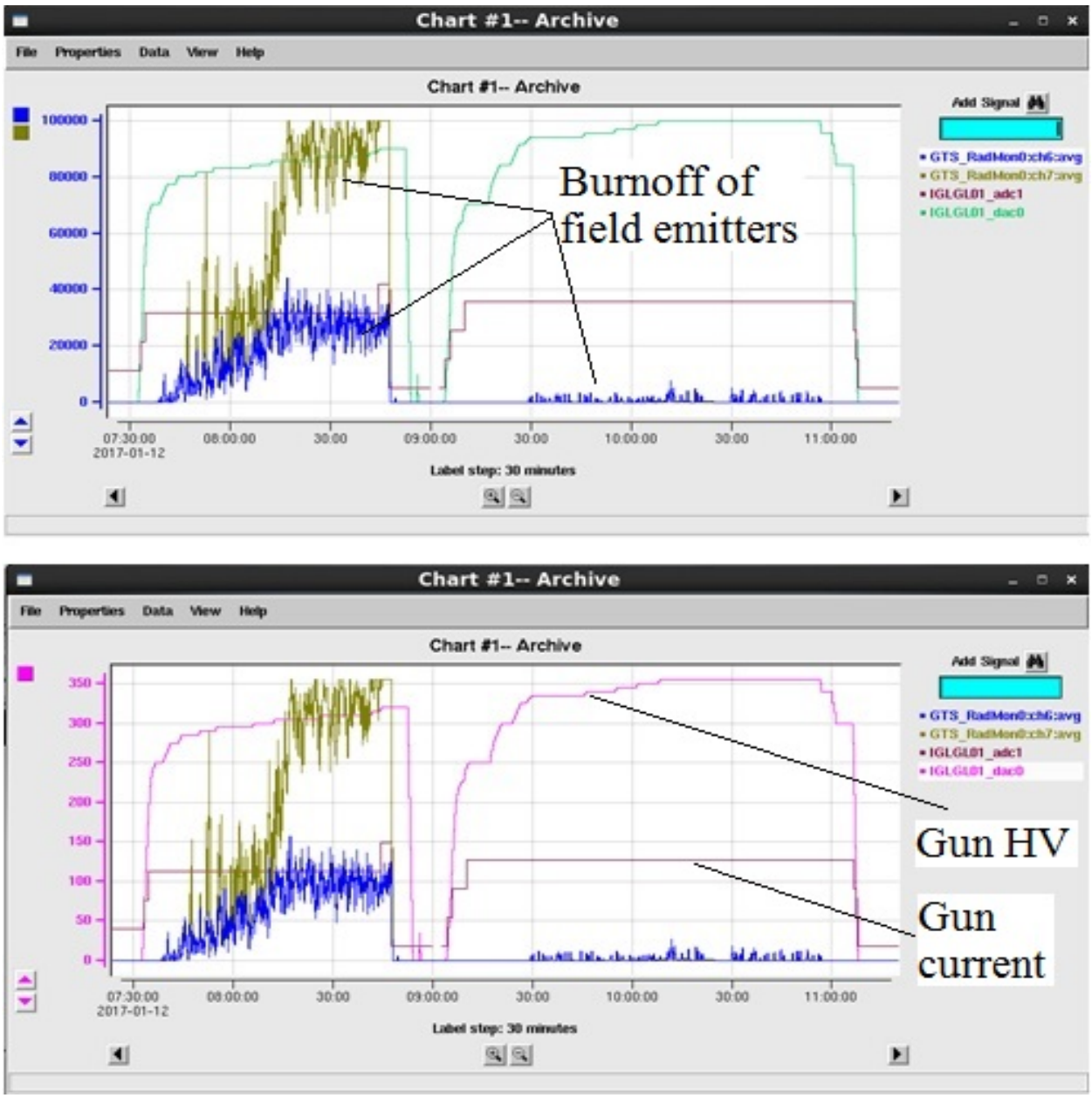

FIG. 51: A burn-off of field emitters trips off the gun high voltage. Top: Field emission counts before and after the burn-off of emitters. Bottom: The gun current jumps prior to gun high voltage trips off.

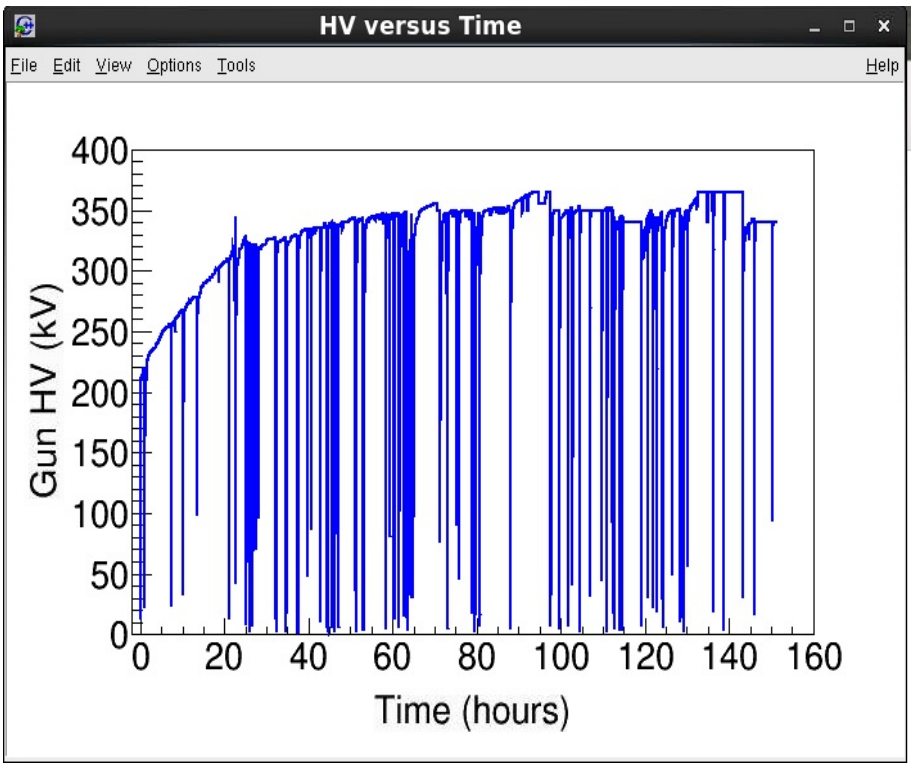

FIG. 52: Gun conditioning time: about 150 hours were spent to high voltage condition the gun. Note: The vertical axis uses the absolute values of the gun bias voltage.

3.5 INITIAL BEAMLINE COMMISSIONING

During the gun high voltage conditioning the real photocathode was not in the gun. Instead a dummy photocathode was installed. Once the photogun was high voltage conditioned it could be used for beam operations. A photogun must work together with a photocathode and a laser system to generate electron beam; the photocathodes will be discussed in Chapter 4. After finishing conditioning the photogun the dummy photocathode was taken out and a real photocathode was put in. After turning on the gun high voltage to -300 kV beamline commissioning was started.

First, a very low-power beam was sent to the first viewer in the beamline located 147 cm downstream of the photocathode. As predicted from the POISSON calculation beam was kicked downward due to the field asymmetry in the region between the photocathode and anode. The downward kick was compensated for using the first pair of correctors, and a slight correction was needed for the horizontal direction. After finding beam on the first viewer, the beam was centered on lens #1 and lens #2. Then beam was steered onto the

second viewer, which is 197.8 cm downstream of the photocathode. After beam was steered onto the last viewer, which is 375.6 cm downstream of the photocathode, beam was centered on lens #3 and lens #4. With beam viewers the polarities of the correctors were checked; a couple of them were found to have wrong polarities. The polarities were corrected by swapping the leads.

Second, a beam with slightly higher power was sent to the Faraday cup located 219.89 cm downstream of the photocathode and the current readback was recorded. Then beam was sent to the beam dump, which is 455.34 cm downstream of the photocathode. The beam dump is the final beamline component where beam stops. By adjusting the beam orbit to make sure the current readback from the dump is the same as that from the Faraday cup, one ensures the beam is transported cleanly from the beginning of the beamline to the beam dump, i.e., with no beam loss.

After beam transported cleanly to the dump the beam current was raised to a few μA. While beam was delivered to the beam dump the vacuum signals were monitored to make sure beam transported well and the system was stable. If the system is not stable or beam scrapes the beampipe the vacuum level will be elevated.

The beamline was successfully commissioned with the gun biased at -300 kV. This means that from the gun to the beam dump every components worked as designed. The high current runs were not tried until a later time when the photocathode lifetimes were measured.

3.6 BEAM OPERATIONS

After the beamline was successfully commissioned we tried to measure the beam emittance using the scan-solenoid technique described later in this thesis. At first we used the DC laser, lenses, and viewers. Later the RF puled laser was built and installed in the GTS. To support precise emittance measurements a wire scanner was installed upstream of viewer #3. Then we started to measure beam emittance using the RF laser, lenses, viewers, and the wire scanner. For beamline commissioning and emittance measurements the beam current was low, usually in the nano Ampere range. During the photocathode QE lifetime measurements the current was up to 28 mA.

3.7 SUMMARY OF NEW GUN PERFORMANCE

During beam operations, the gun high voltage was stable with minimal field emission. Overall the gun performed well. Since the beam operations started in 2016 two insulators have been used. The first one failed. The second one is still in use.

The first insulator failed after about 1400 hours of beam operations over a period of fourteen months. Then there was an arc inside the photogun vacuum chamber. At the time it failed the gun current spiked which tripped off the gun high voltage. Subsequent attempts to turn on the gun high voltage failed.

Past experience shows that a failure of a high voltage gun has happened at two places. One location is the cable and its plugs connecting the HVPS to the gun chamber. Another location is at the insulator near the triple-point region to the top flange. An inspection of the cable showed that the cable and its plugs were intact. But damage on the insulator could be seen clearly. An arc damaged the insulator. The arcing clearly started from high voltage end of the plug, traveled towards ground, and punched through the ceramic insulator about 2 cm from the flange as shown in Figure 53. The root cause of the failure is the grounding of the photocathode. The day before the failure happened a QE mapping of a photocathode was performed. The photocathode was electrically grounded during the QE mapping. After finishing the QE mapping the grounding was not removed.

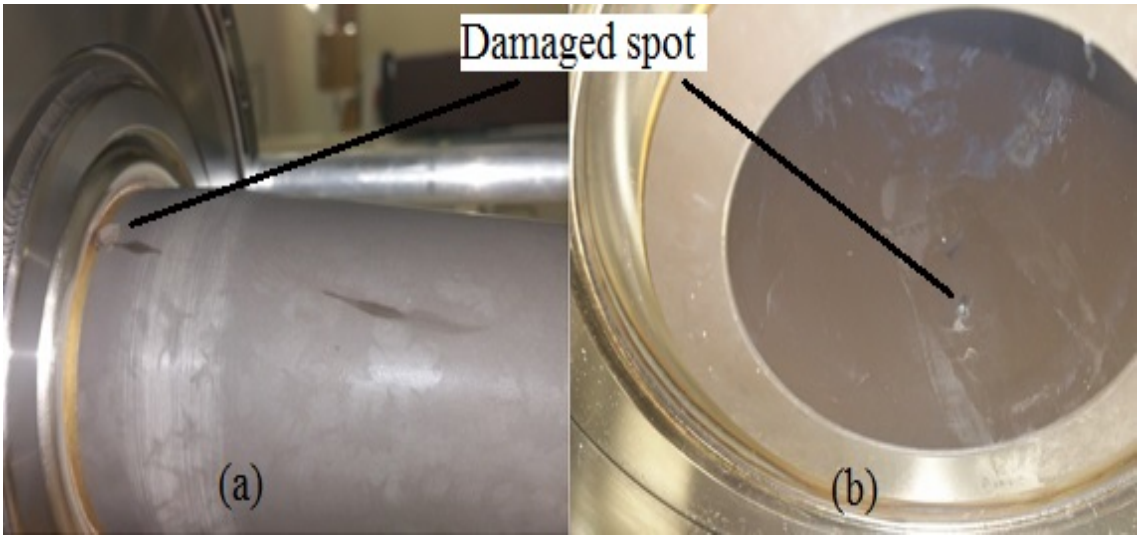

FIG. 53: A damaged insulator: (a) vacuum side (b) air side.

The next day the gun high voltage was energized with the photocathode still grounded. The gun high voltage would not ramp up due to an over-current fault. A few more attempts gave the same results. After realizing that the cathode electrode was grounded the grounding was removed. Then one was able to ramp up the gun high voltage to -300 kV and conditions looked normal at first. Twenty minutes later the gun suddenly tripped off on an over-current fault. An arc caused the gun current to reach the pre-set trip limit of 5 mA. No precursor

was observed. After the trip the gun could not be turned on any more. It was believed that turning on the gun high voltage with the cathode grounded caused the first damage.

Figure 54 shows about 1400 hours of beam operation for the first insulator with the photogun voltage between -150 to -300 kV. During this period most times the gun was operated at -300 kV and sometimes at lower bias voltages based on the program needs.

When the insulator was damaged there was a vacuum leak through the pin hole caused by the arcing. The damaged insulator could not be repaired and was replaced. This means venting the gun chamber, replacing the insulator, baking the gun chamber, etc.

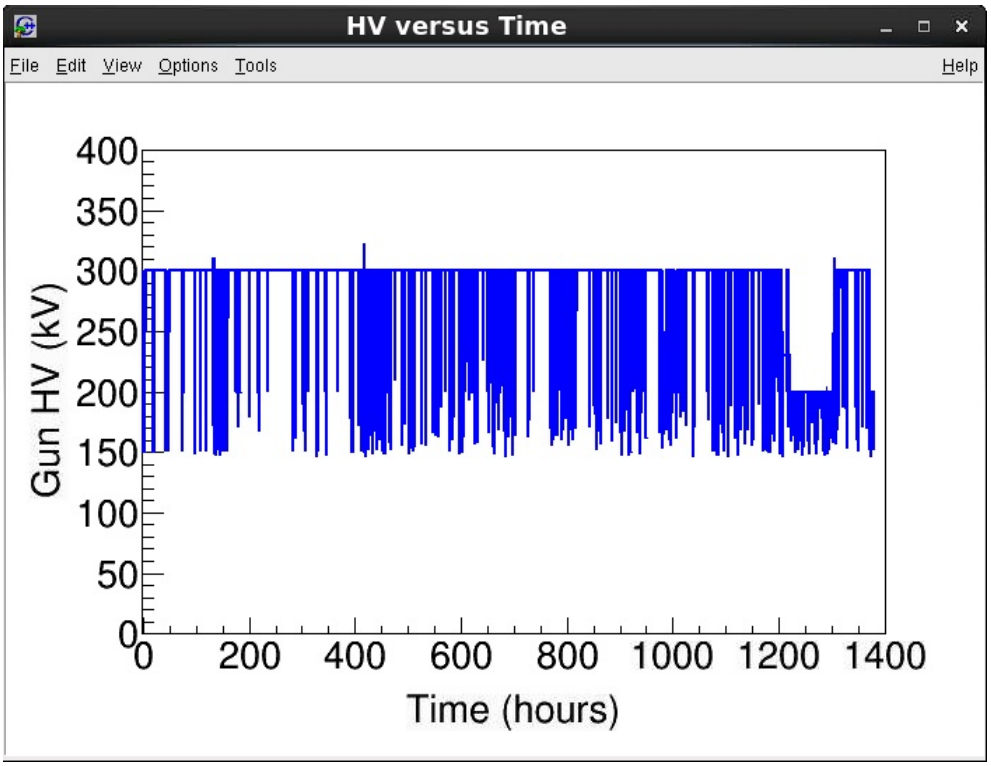

FIG. 54: The beam operation time of the first insulator with high voltage above -150 kV. Note: The vertical axis uses the absolute values of the gun bias voltage.

Since the failure was not caused by design flaws no change was made to the system. The faulty insulator was replaced with a new one, the gun vacuum chamber was baked, and the gun was high voltage conditioned. The gun has been working fine since the second insulator was installed. In about six months period the gun was operated about 590 hours.

After the second insulator was installed the photocathode lifetimes were measured on all the photocathodes. All the lifetime measurements were done with beam current less than the high voltage power supply current limit of 5 mA. Subsequently the power supply was

replaced with a Spellman power supply to increase the current limit. With the new power supply the current was run up to 28 mA. During this high current run period the running time was about 300 hours. The gun has sustained hundreds of hours of high current runs, and performed well as its current is limited only by the power supply.

CHAPTER 4

ALKALI ANTIMONIDE PHOTOCATHODES

A photocathode is an important part of a photogun. As an electron source a photogun must have a photocathode and accompanying laser system in order to produce and deliver electron beam. When a photocathode is struck by a quantum of light (photon), the absorbed energy causes electron emission due to the photoelectric effect. The photocathode is a practical method for converting light to an electron current. Photocathodes are divided into two broad groups: transmission photocathodes and reflective photocathodes. A transmission type photocathode is typically a coating upon a glass window in which the light strikes one surface and electrons exit from the opposite surface. A reflective type is typically formed on an opaque metal electrode base, where the light enters and the electrons exit from the same side. Reflective type photocathodes are made and used at the GTS. The effectiveness of a photocathode is commonly expressed as Quantum Efficiency (QE), that being the ratio of the number of emitted electrons over the number of impinging quanta (of light).

There are many photocathode materials. For example, GaAs is used to produce polarized electrons in the Jefferson Lab accelerator. This photocathode material covers a wide spectral response range from 930 nm to ultraviolet. One of the important properties of a GaAs photocathode is that it can achieve Negative Electron Affinity when Cs is deposited on the surface. However GaAs photocathodes are very delicate and lose QE easily. Ion back bombardment is the main cause of GaAs photocathode QE decay.

Alkali antimonide photocathodes have gained a lot of attention in recent years because of their high QE, high current achieved, and robustness. JLEIC electron cooling ring requires a robust, high average current, magnetized electron beam, and thus alkali antimonide photocathodes are good candidates for the JLEIC cooler. In this work Cs_xK_ySb photochodes were made and some beam based studies were conducted. Green laser of 532 nm wavelength was used for the beam studies. Those beam studies include beam emittance and lifetime measurements, which are discussed in Chapter 6.

Photocathodes operate in a vacuum. From photocathode fabrication to the beam production, all processing is completed under vacuum conditions. Photocathodes are fabricated in a dedicated photocathode preparation chamber. After a photocathode is made it can be transferred into the gun vacuum chamber or stored in the preparation chamber for later use.

A dedicated chamber for making photocathodes has some advantages. Fabricating photocathodes involves vapor deposition of Sb, Cs, and K on substrates. Without isolation this process would contaminate other parts in the chamber. If the deposition were completed in the gun vacuum chamber it would be difficult to maintain a good vacuum due to the vapor contamination especially when the gun is biased to a high voltage, and inadvertent exposure of alkali metals onto the cathode electrode can lead to field emission, and accidental deposition of metals onto the insulator can lead to breakdown. After a photocathode is made usually it takes many hours for the vacuum to recover. So having a dedicated photocathode preparation chamber allows the gun chamber to remain clean and saves time for beam operations.

4.1 SUBSTRATES

During fabrication of alkali antimonide photocathodes, first an antimony layer needs to be grown on a substrate. In this research two types of substrates were used. One is GaAs, the other is molybdenum. Figure 55 shows (a) a GaAs substrate and (b) a molybdenum substrate.

The GaAs substrate is a single-side polished, p-doped, single-crystal GaAs (100) wafer of 0.5 mm thickness that was procured from AXT Company. The wafer was cleaved into square-shaped pieces, 15 mm × 15 mm. Each piece is then attached to a puck. The molybdenum substrate is made by the machine shop at Jefferson Lab having dimensions of 1 mm × 15 mm × 15 mm. It is diamond paste polished to a mirror like condition.

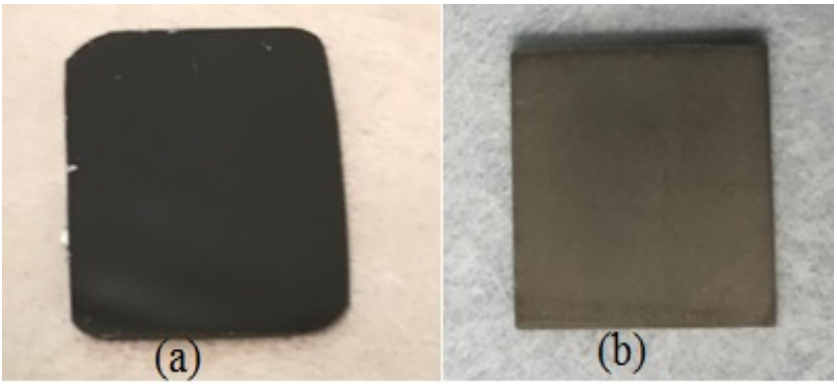

FIG. 55: The substrates used in this research. (a) GaAs. (b) Molybdenum.

When a substrate is attached to a puck a small amount of indium is applied between the puck and the substrate so that the substrate can have an even contact with the puck and the

substrate can be uniformly heated during a heat cleaning and deposition of the chemicals.

During beam based studies photocathodes with different substrates will be compared to see how the beam quality varies. The substrate could affect beam emittance and photocathode QE lifetime.

4.2 ANTIMONY AND ALKALI

Antimony, cesium, and potassium are three chemical elements needed to fabricate alkali antimony photocathodes. They must be loaded into their containers in advance. Antimony is put in the crucible as shown in Figure 6 on page 11. The procedure for loading antimony is documented in Appendix E.

Traditionally procedures for fabrication of the alkali-antimonide photocathodes employ sequential deposition of Cs and K on a Sb film. To make our photocathodes we use a new technique, co-deposition of Cs and K. Consequently Cs and K are loaded into the same source reservoir. Figure 8 on page 12 shows the effusion type alkali dispenser. The procedure for loading Cs and K is documented in Appendix F.

4.3 FABRICATION OF PHOTOCATHODES

The photocathode substrates are attached to the pucks in the assembly room prior to putting the pucks into the preparation chamber. To begin, five pucks are loaded into the photocathode preparation chamber. One is the dummy puck used to high voltage condition the gun already mentioned. The surface of the dummy puck is a piece of polished stainless steel. The next puck has a molybdenum substrate and the other three have GaAs substrates. There are two major steps involved in the process of fabricating a photocathode. The first step is to deposit Sb on a substrate. The second step is to co-deposit Cs and K on the Sb layer.

Figure 56 (a) shows the setup for depositing Sb. The puck is positioned up-side down so that the substrate faces down. This is achieved using the top heater. Attached to the end of the top heater is a grabbing device as shown in Figure 11. The grabbing device holds the puck firmly up-side down. The puck can then be moved up or down linearly via the linear actuator attached to the top heater. The linear actuator is fixed on the flange. The puck and heater move together. After the puck is in the predetermined position the mask can be moved into position, about 1 mm beneath the puck. One can place one of the mask holes in the center of the puck. If a full activation is needed the mask would be in the same location vertically but would be beside the puck instead of underneath it (this is for the purpose of

measuring the QE). A full activation means that the photocathode active area has the size of the whole exposed substrate, which is 12.8 mm in diameter. Once the puck and mask are in position the pre-heated Sb source can be moved in. The Sb source can only move horizontally. The distance between the puck and the Sb source is about 3.8 cm. Since the Sb source is pre-heated the deposition starts once the Sb source is in position.

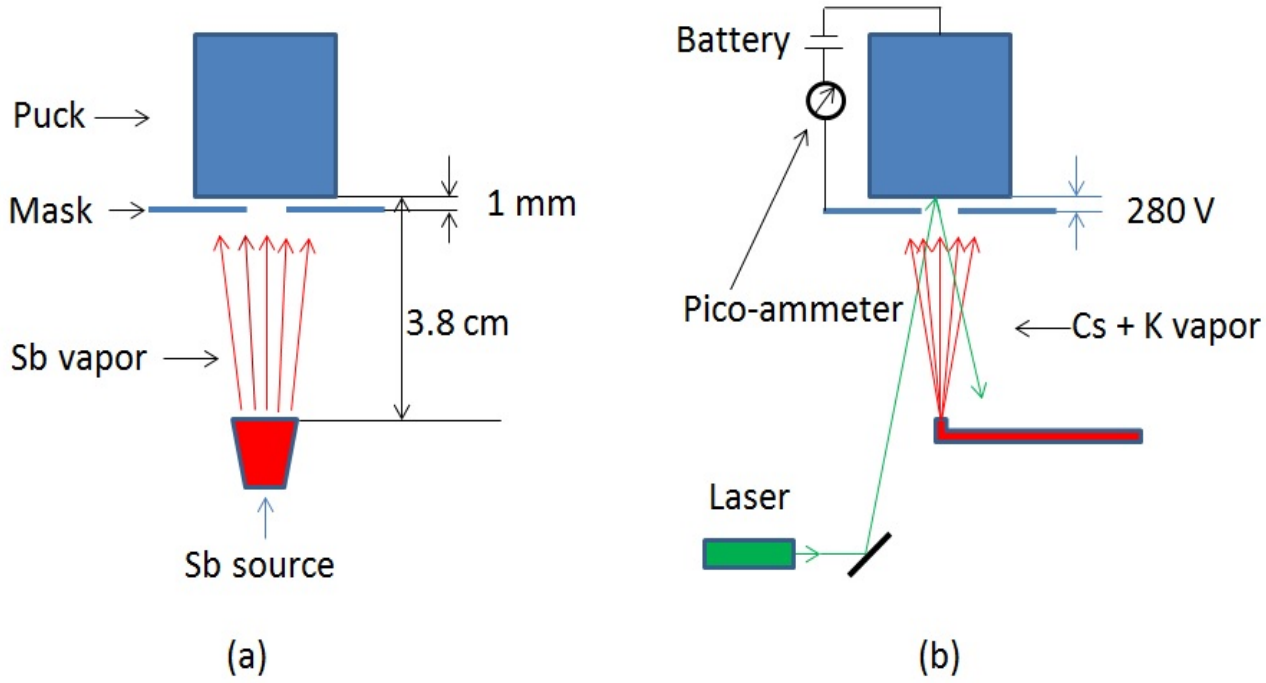

FIG. 56: Two major steps of fabricating photocathodes. (a) Deposition of Sb. (b) Co-deposition of Cs and K.

Figure 56 (b) shows the setup for co-deposition of Cs and K. After the deposition of Sb is finished the Sb source is retracted to the garage position via the linear actuator and the power to the heater discontinued. The mask and puck remain at the same positions. The Cs and K source is moved into position. The Cs and K source can only be moved horizontally. In order to monitor the photocurrent a laser and a pico-ammeter are needed. Then a bias between the mask and the puck can be activated. The distance between the mask and the Cs and K dispenser tip is the same as that between the mask and the Sb source. The 0.2 mW probe laser is pre-aligned. The QE of the photocathode can be calculated using the laser power and the measured instantaneous photocurrent.

In the initial part of the exposure the QE increases. The QE eventually stabilizes. It will eventually begin to decrease. At this time the Cs and K source is retracted to the garage position to stop depositing Cs and K. The heat to the Cs and K reservoir should be turned off and the valve between the dispenser and the reservoir is closed to isolate the photocathode.

After the co-deposition of Cs and K the pressure of the preparation chamber is still elevated even though the heat sources are off. It takes several hours to pump down to the prior-to-fabrication vacuum condition. Once the preparation chamber vacuum achieves good conditions again, the photocathode can be transferred to the photogun chamber for use.

From prior work at Cornell University [23], it is expected that the thickness of the antimony layer affects the beam quality and the performance of the photocathode [10], but so far no systematic beam based studies have been done to measure this effect. In this research photocathodes with different thickness of antimony layers were made. To obtain a variety of antimony film thicknesses, the current applied to the Sb heater basket was set constant and the deposition time was varied with other conditions the same. The thickness of the antimony layer depends on the deposition time. The longer the deposition time the thicker the antimony layer. When making photocathodes with GaAs substrates, 10, 20, 30, 60, and 90 minutes deposition time were used to make the antimony layers. Only one photocathode with molybdenum substrate was made and the deposition time for the antimony layer was 10 minutes. Appendix G has the detailed procedure of fabrication of photocathodes.

The photocathode surface roughness can be evaluated by shining the laser light on the photocathode with the photocathode in the gun vacuum chamber. The light absorption rate can be calculated from the measured incident laser power and the reflected laser power. The light absorption rates would the same if the surface roughnesses of the photocathodes with different thicknesses of the Sb layers are the same since the photocathodes are made from identical materials.

4.4 EVALUATION OF PHOTOCATHODES

The main parameters used to evaluate photocathode quality are quantum efficiency (QE) and QE lifetime. High QE and long lifetime are desired. Quantum efficiency, the ratio between the number of photoemitted electrons and the incoming photons, can be calculated using the equation

$$\mathrm{QE}(\%) = ((Ihc)/(\lambda eP)) \times 100\% = 124I/(\lambda P) \tag{4.1}$$

where P (mW) is laser power, I (μA) is the measured photocurrent, λ is the laser wavelength

(532 nm), h is Planck's constant (6.626×10^{-34} J s), e is the electron charge (1.6×10^{-19} C), and c is the speed of light (2.998×10^{8} m s^{-1}). While fabricating a photocathode the QE is monitored in the photocathode preparation chamber.

If the laser is scanned across the whole photocathode surface a QE map of the photocathode can be obtained. This is done in the photogun chamber. Figure 57 shows the setup of QE mapping of photocathodes. The photocathode is grounded using the long manipulator. The anode plate is positively biased to 284 V. The photocurrent is read via the pico-ammeter.

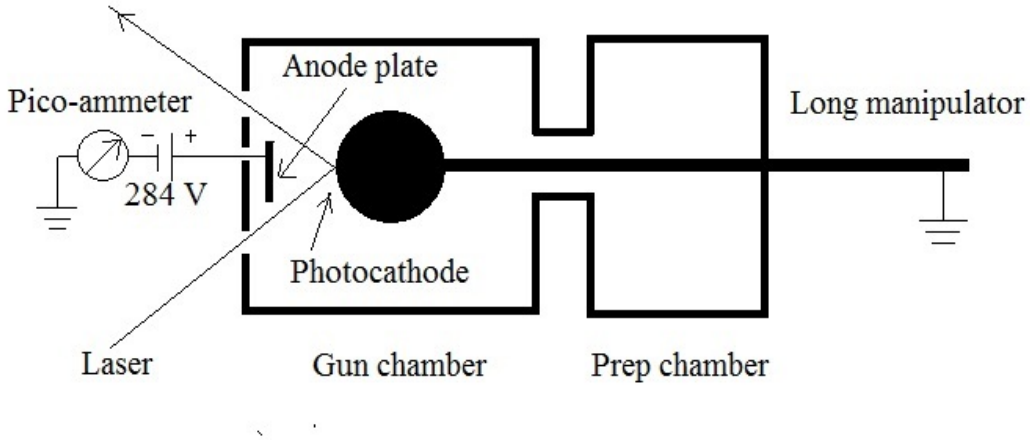

FIG. 57: A setup for QE mapping

The QE laser must be aligned prior to a QE mapping of a photocathode. First the laser light must go into the photogun chamber from one of the horizontal view port, hit the photocathode, and exit from another horizontal view port. Second the scan range must be correct. Scanning the laser is controlled through two stepper-motors. One stepper-motor drives a mirror to move the laser in x plane, and another stepper-motor drives a mirror to move the laser in y plane independently. Initially the laser is positioned at the start point by setting the x/y stepper-motors controls to zero. This point corresponds to point A in Figure 58. Then the laser is positioned to the finish point by setting the x/y stepper-motors controls to 2000. This point corresponds to point B in Figure 58. This is to make sure the laser scans the area that is defined by the dotted line and covers the whole photocathode area as shown in Figure 58. Figure 59 is a QE mapping of a photocathode. The QE mapping procedure is described in Appendix H. The QE lifetime measurement will be discussed in

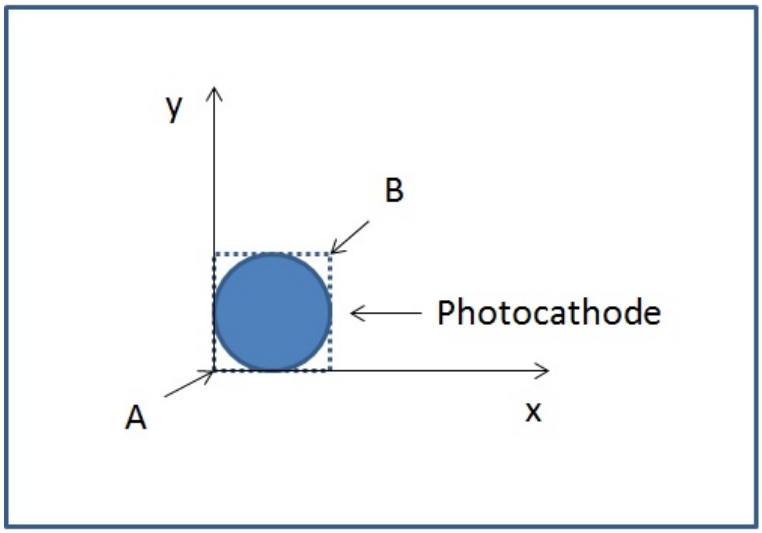

FIG. 58: Point A is the QE scan start position, and point B is end position.

The QE mapping just gives a rough idea what the QE is at each point on the photocathode. The values are usually lower than the actual QE values because the anode plate may not collect every electron from the photocathode since the 284 V bias voltage is relatively low. Sometimes it can be up to 40% lower than the actual QE. More accurate QE can be determined by turning on the gun high voltage and sending beam to the Faraday cup. When beam transports cleanly to the Faraday cup, one can calculate the QE using the beam current to the Faraday cup and the input laser power. The drawback of this method is that only one location can be measured each time so it is not easy to map the whole photocathode. Even if the gun high voltage is on, the beam current may not include all the electrons coming out of the photocathode since the anode plate could intercept some electrons. But if beam transports cleanly the interception on the anode is very small, less than 0.1%.

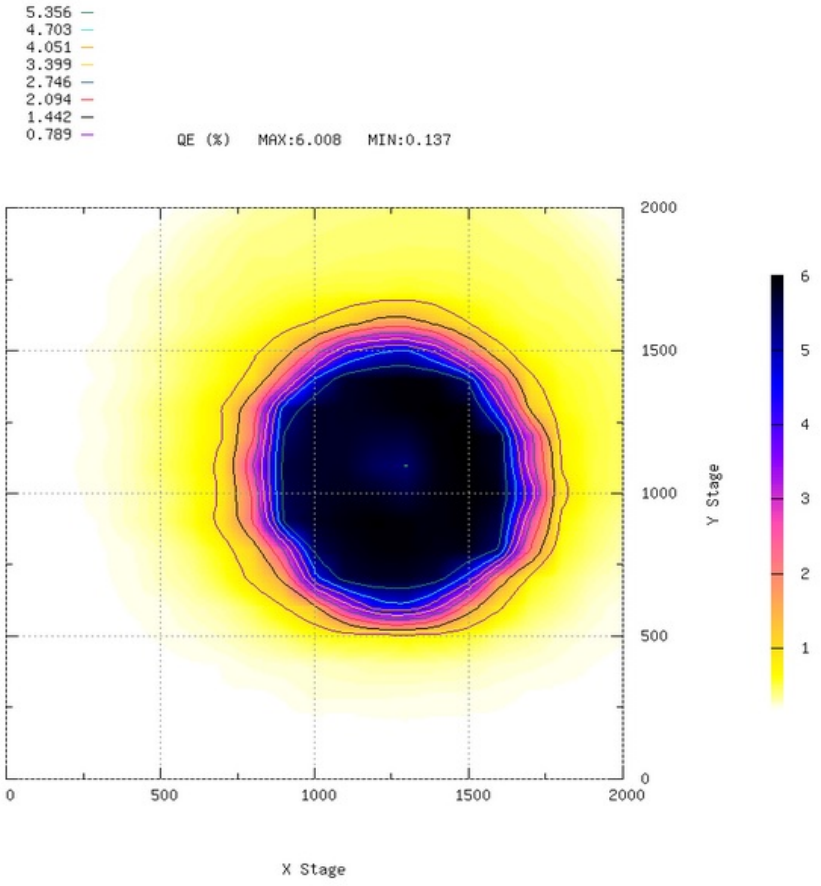

FIG. 59: A QE map shows the QE information of a photocathode.

CHAPTER 5

BEAM DYNAMICS AND OPTICS

In this chapter some basic concepts about the behavior of an electron beam in electromagnetic fields will be introduced. Only linear beam motion will be discussed. The phase space, beam matrix, and beam emittance will be introduced and the procedure for measuring the beam emittance will be given.

5.1 PARTICLE DYNAMICS IN ELECTROMAGNETIC FIELDS

A beam of charged particles is expected by design to follow closely a prescribed path along a desired beam transport line. The Lorentz forces bend and direct the charged particle beam or provide focusing to hold particles close to the ideal path. The Lorentz forces are derived from electric and magnetic fields through the Lorentz equation. For a particle carrying a single basic unit of electrical charge the Lorentz force is expressed by

$$\boldsymbol{F} = e\boldsymbol{E} + e[\boldsymbol{v} \times \boldsymbol{B}] \tag{5.1}$$

where e is the electrical charge, the vectors $\boldsymbol{E}$ and $\boldsymbol{B}$ are the electrical and magnetic field vectors, respectively, and $\boldsymbol{v}$ is the velocity vector of the particle. Such Lorentz forces will be applied not only to guide particles along a pre-defined path but will also be used for beam focusing to confine a beam of particles to within a narrow vicinity of the ideal path. The evolution of particle trajectories under the influence of Lorentz forces is called beam dynamics or beam optics. The basic formulation of beam dynamics relies on linear fields which are independent of or only linearly dependent on the distance of a particular particle from the ideal trajectory. The mathematical description of particle trajectories in the presence of such linear fields is called linear beam dynamics.

The Lorentz force has two components originating from either an electrical field $\boldsymbol{E}$ or a magnetic field $\boldsymbol{B}$. For relativistic particles ($v \approx c$) the force from a magnetic field of 1 T is equivalent to that for an electrical field of 300 MV/m. Since it is technically easy to generate magnetic fields of the order of 1 T, but rather difficult to establish the equivalent electric fields of 300 MV/m, it becomes apparent that most beam guidance and focusing elements for relativistic particle beams are based on magnetic fields.

5.2 LINEAR EQUATION OF MOTION

The horizontal or vertical differential equation of particle motion is given by Hill's equation [11–14]:

$$\frac{d^2u}{ds^2} + K(s)u = 0, \tag{5.2}$$

where u stands for x or y, K is assumed to be constant, and s is the distance along the beam path. The principal solutions of this differential equation are for $K > 0$

$$C(s) = \cos(\sqrt{K}s), S(s) = \frac{1}{\sqrt{K}}\sin(\sqrt{K}s) \tag{5.3}$$

and for $K < 0$

$$C(s) = \cosh(\sqrt{-K}s), S(s) = \frac{1}{\sqrt{-K}}\sinh(\sqrt{-K}s) \tag{5.4}$$

These linearly independent solutions satisfy the following initial conditions:

$$\begin{aligned} C(0) = 1, C'(0) = \frac{dC}{ds} = 0, \\ S(0) = 0, S'(0) = \frac{dS}{ds} = 1. \end{aligned} \tag{5.5}$$

Any arbitrary solution $u(s)$ can be expressed as a linear combination of these two principal solutions

$$\begin{aligned} u(s) = C(s)u_0 + S(s)u_0', \\ u'(s) = C'(s)u_0 + S'(s)u_0'. \end{aligned} \tag{5.6}$$

where u_0, u_0' are arbitrary initial parameters of the particle trajectory and derivatives are taken with respect to the independent variable s.

The solution (5.6) of the equation of motion (5.2) may be expressed in matrix formulation as

$$\begin{pmatrix} u(s) \\ u'(s) \end{pmatrix} = \begin{pmatrix} C(s) & S(s) \\ C'(s) & S'(s) \end{pmatrix} \begin{pmatrix} u_0 \\ u_0' \end{pmatrix} \tag{5.7}$$

If one calculates the principal solutions of (5.2) for individual magnets only, one can obtain such a transformation matrix for each individual element of the beam transport system. Noting that within each of the beam line elements, whether it is a drift space or a magnet, the restoring forces are indeed constant, one may use within each single beam line element the simple solutions (5.3) or (5.4) to solve the equation of motion (5.2). With these solutions, one can immediately get transformation matrices for each beam line element. In matrix formalism, one can follow a particle trajectory along a complicated beam line by repeated

matrix multiplications from element to element. Using this method one has completely eliminated the need to solve the differential equation (5.2) at every s. The simple solutions (5.3), (5.4) will suffice to treat the beam transport problems in this thesis.

In the case of focusing, $K > 0$, from Equations 5.3 and 5.7, one obtains

$$M = \begin{pmatrix} C(s-s_0) & S(s-s_0) \\ C'(s-s_0) & S'(s-s_0) \end{pmatrix} = \begin{pmatrix} \cos(\sqrt{K}(s-s_0)) & \frac{1}{\sqrt{K}}\sin(\sqrt{K}(s-s_0)) \\ -\sqrt{K}\sin(\sqrt{K}(s-s_0)) & \cos(\sqrt{K}) \end{pmatrix}. \quad (5.8)$$

In the thin lens approximation, $l = s - s_0 \longrightarrow 0$, while keeping the focal strength constant,

$$\frac{1}{f} = Kl = \quad \text{constant}, \quad (5.9)$$

Equation 5.8 becomes

$$M = \begin{pmatrix} 1 & 0 \\ -1/f & 1 \end{pmatrix}, \quad (5.10)$$

where f is the focal length of the lens. This approximation is appropriate, as in light optics, when the transverse offset does not change significantly as the lens is traversed.

For a zero-field drift space region, $s - s_0 = L$, and $K = 0$, one obtains

$$M = \begin{pmatrix} C(s-s_0) & S(s-s_0) \\ C'(s-s_0) & S'(s-s_0) \end{pmatrix} = \begin{pmatrix} 1 & L \\ 0 & 1 \end{pmatrix}. \quad (5.11)$$

5.3 BEAM DYNAMICS OF A SOLENOID

A solenoid magnet may be used to focus an electron beam. It works as a beam optical lens. A sketch of a solenoid and its field is shown in Figure 60. In addition to the magnetic

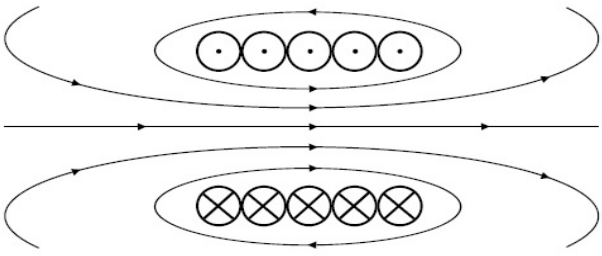

FIG. 60: Magnetic field lines of a solenoid.

field B_z along the beam line a radial field B_r exists. The rotationally symmetric fields can be expanded in a polynomial series [15]:

$$\begin{aligned} B_z(z,r) &= B_{z,0} - \frac{r^2}{4}\frac{\mathrm{d}^2 B_z(z)}{\mathrm{d}z^2} + \frac{r^4}{64}\frac{\mathrm{d}^4 B_z(z)}{\mathrm{d}z^4}..., \\ B_r(z,r) &= -\frac{r}{2}\frac{\mathrm{d}B_z(z)}{\mathrm{d}z} + \frac{r^3}{16}\frac{\mathrm{d}^3 B_z(z)}{\mathrm{d}^3 z} - \frac{r^5}{384}\frac{\mathrm{d}^5 B_z(z)}{\mathrm{d}^5 z}..., \\ B_\theta &= 0. \end{aligned} \tag{5.12}$$

with z as the principal axis of the magnet, r as the transverse distance from the symmetry axis, and $B_{z,0}$ as the on-axis magnetic field in the z-direction. The strength at the center of a solenoid magnet is $B_0 = \mu_0 \mu_r J$, with μ_0 being permeability of free space, μ_r relative permeability, and J the total solenoid current per unit length. Radial field B_r components appear whenever the longitudinal field strength varies as is the case in the fringe field region at the end of the solenoid. The azimuthal field component obviously vanishes because of symmetry.

Because of the geometry of a solenoid it is useful to choose cylindrical coordinates. The correspondence between cylindrical and Cartesian coordinates is defined as:

$$\boldsymbol{r} = \begin{pmatrix} r\cos\theta \\ r\sin\theta \\ z \end{pmatrix}. \tag{5.13}$$

The unit vectors are defined as

$$\hat{\boldsymbol{r}} = \begin{pmatrix} \cos\theta \\ \sin\theta \\ 0 \end{pmatrix}, \quad \hat{\theta} = \begin{pmatrix} -\sin\theta \\ \cos\theta \\ 0 \end{pmatrix}, \quad \hat{z} = \begin{pmatrix} 0 \\ 0 \\ 1 \end{pmatrix}. \tag{5.14}$$

The position vector $\boldsymbol{r}$ can be written as

$$\boldsymbol{r} = r\hat{\boldsymbol{r}} + z\hat{\boldsymbol{z}}. \tag{5.15}$$

The first and second time derivatives of the vector $\boldsymbol{r}$, denoted with a dot:

$$\frac{\mathrm{d}\boldsymbol{r}}{\mathrm{d}t} = \dot{r}\hat{\boldsymbol{r}} + r\dot{\theta}\begin{pmatrix} -\sin\theta \\ \cos\theta \\ 0 \end{pmatrix} + \dot{z}\hat{\boldsymbol{z}} = \dot{r}\hat{\boldsymbol{r}} + r\dot{\theta}\hat{\theta} + \dot{z}\hat{\boldsymbol{z}} \tag{5.16}$$

$$\begin{aligned} \frac{\mathrm{d}^2\boldsymbol{r}}{\mathrm{d}t^2} &= \ddot{r}\hat{\boldsymbol{r}} + \dot{r}\dot{\theta}\hat{\theta} + \dot{r}\dot{\theta}\hat{\theta} + r\ddot{\theta}\hat{\theta} - r\dot{\theta}^2\hat{\boldsymbol{r}} + \ddot{z}\hat{\boldsymbol{z}} \\ &= (\ddot{r} - r\dot{\theta}^2)\hat{\boldsymbol{r}} + (2\dot{r}\dot{\theta} + r\ddot{\theta})\hat{\theta} + \ddot{z}\hat{\boldsymbol{z}}. \end{aligned} \tag{5.17}$$

Because there is no electric field Equation 5.1 on page 64 becomes

$$\boldsymbol{F} = e\boldsymbol{v} \times \boldsymbol{B}. \tag{5.18}$$

Using Equation 5.16, one obtains

$$\begin{aligned} \boldsymbol{F} &= \gamma m_0 \ddot{\boldsymbol{r}} = e\dot{\boldsymbol{r}} \times \boldsymbol{B} \\ &= e[(r\dot{\theta}B_z - \dot{z}B_\theta)\hat{r} + (\dot{z}B_r - \dot{r}B_z)\hat{\theta} + (\dot{r}B_\theta - r\dot{\theta}B_r)\hat{z}]. \end{aligned} \tag{5.19}$$

Now as $B_\theta = 0$ and $B_r(z, r)$ can be approximated by the linear part of the second equation of 5.12, the following equations are obtained:
Radial focusing:

$$\gamma m_0(\ddot{r} - r\dot{\theta}^2) = er\dot{\theta}B_z \tag{5.20}$$

Rotation:

$$\gamma m_0(2\dot{r}\dot{\theta} + r\ddot{\theta}) = -e(\frac{r\dot{z}}{2}B_z' + \dot{r}B_z) \tag{5.21}$$

Acceleration:

$$\gamma m_0 \ddot{z} = \frac{1}{2}er^2\dot{\theta}B_z' \tag{5.22}$$

These identities are linear approximations which only hold for electrons near the z-axis of the solenoid. To determine the Larmor angle, θ_L, only the equation for the rotation is needed. With

$$\begin{aligned} \frac{\mathrm{d}}{\mathrm{d}t}(r^2\dot{\theta}) &= r^2\ddot{\theta} + 2r\dot{r}\dot{\theta}, \\ \frac{\mathrm{d}}{\mathrm{d}t}(r^2 B_z) &= r^2\dot{B}_z + 2r\dot{r}B_z, \\ \dot{B}_z = \frac{\mathrm{d}B_z}{\mathrm{d}t} &= \frac{\mathrm{d}B_z}{\mathrm{d}z}\frac{\mathrm{d}z}{\mathrm{d}t} = B_z'\dot{z}, \end{aligned} \tag{5.23}$$

It follows

$$\begin{aligned} \frac{\gamma m_0}{r}(2r\dot{r}\dot{\theta} + r^2\ddot{\theta}) &= -\frac{e}{2r}(r^2\dot{z}B_z' + 2r\dot{r}B_z), \\ \frac{\gamma m_0}{r}\frac{\mathrm{d}}{\mathrm{d}t}(r^2\dot{\theta}) &= -\frac{e}{2r}\frac{\mathrm{d}}{\mathrm{d}t}(r^2 B_z), \\ r^2\dot{\theta} &= -\frac{e}{2\gamma m_0}r^2 B_z. \end{aligned} \tag{5.24}$$

Therefore

$$\theta_L = -\frac{e}{2\gamma m_0}\int B_z \mathrm{d}t = -\frac{e}{2\gamma m_0}\int B_z \frac{\mathrm{d}t}{\mathrm{d}z}\mathrm{d}z = -\frac{e}{2\gamma m_0}\int B_z \frac{\mathrm{d}z}{\dot{z}} = -\frac{e}{2p_z}\int B_z \mathrm{d}z. \tag{5.25}$$

The Larmor rotation is proportional to the integral of the magnetic field.

The focusing strength can be calculated using Equation 5.25 and the focusing Equation 5.20:

$$\begin{aligned}
\gamma m_0(\ddot{r} - r\dot{\theta}^2) &= er\dot{\theta}B_z, \\
\ddot{r} &= -\frac{e^2 r}{2(\gamma m_0)^2}B_z^2 + \frac{e^2 r}{4(\gamma m_0)^2}B_z^2 = -\frac{e^2 r}{4(\gamma m_0)^2}B_z^2, \\
\dot{r} &= -\frac{e^2}{4(\gamma m_0)^2}\int r B_z^2 \mathrm{d}t, \\
r' &= -\frac{e^2}{4}\int \frac{r B_z^2}{(\gamma m_0 \dot{z})^2}\mathrm{d}z
\end{aligned} \tag{5.26}$$

A thin lens approximation is possible assuming r is constant in the vicinity of the solenoid. The thin lens focusing strength is given as

$$\frac{1}{f} = -\frac{r'}{r} = \left(\frac{e}{2p_z}\right)^2 \int B_z^2 \mathrm{d}z. \tag{5.27}$$

Assuming that the energy spread is small and the particle momentum p_z can be replaced by the total momentum p, Equations 5.25 and 5.27 are good approximations to determine the Larmor angle and the focusing strength of a solenoid. Because of symmetry a solenoid focuses the beam in both transverse directions once it is energized.

Because of the Larmor rotation, a solenoid introduces a x/y coupling when an electron beam passes through it. One way to eliminate this coupling is to use a counter-wound solenoid because the opposite currents from the counter-wound wiring cause the net Larmor rotation to vanish. Because the solenoid focal length or the strength involves the magnetic field squared, the focal length or strength is not canceled. Another way to mitigate the effect of the Larmor rotation is to make the beam round. Otherwise the Larmor rotation effect has to be incorporated into the solenoid transformation matrix.

The GTS beamline solenoids are single-wound, i.e., not counter-wound. Because the electron beam is round the Larmor rotation should not affect the measurements of the beam emittance.

5.4 PHASE SPACE

The motion of charged particles in a beam can be described completely by the six degrees of freedom in phase space, i.e., the position (x, y, z) and momentum (p_x, p_y, p_z) in Cartesian coordinates. The coordinate system is defined as horizontal, vertical, and longitudinal (along the beam) axes represented by x, y, and z, respectively. Phase space is the space in which all possible states of motion are represented. Focusing magnets or accelerating elements are able

to shape the phase space distribution. Liouville's theorem states that the six dimensional phase space density of noninteracting particles is conserved in time. A result following from Liouville's theorem is the volume V in phase space is a constant of motion if one excludes interactions between electrons:

$$\frac{dV}{dt} = 0, \tag{5.28}$$

If correlations between the two dimensional phase spaces (x, p_x), (y, p_y), and (z, p_z) are not present, this result holds for each subspace, separately considered. In this case the total phase space density of particles can be written as the product of the three subspace densities,

$$f(x, p_x, y, p_y, z, p_z) = f(x, p_x) \times f(y, p_y) \times f(z, p_z), \tag{5.29}$$

and each two-dimensional phase space density ($f(x, p_x), f(y, p_y)$, or $f(z, p_z)$) is conserved.

Liouville's theorem provides a powerful tool to describe a beam motion in phase space. Knowledge of the area occupied by particles in phase space at the beginning of a beam transport line will allow one to determine the location and distribution of the beam at any other place along the transport line without having to calculate the trajectory of every individual particle

Because $p_x \simeq p_0 x'$ and $p_y \simeq p_0 y'$ with $x' = \dfrac{dx}{ds}$ and $y' = \dfrac{dy}{ds}$, one can use the slope of the trajectories x', y' instead of the transverse momenta as coordinates, which are proportional to the transverse momenta in the particle phase space.

It has become customary to surround all particles of a beam in phase space by an ellipse called the phase ellipse (Figure 61) described by

$$\gamma x^2 + 2\alpha x x' + \beta x'^2 = \varepsilon, \tag{5.30}$$

where α, β, γ, and ε are ellipse parameters. The area enclosed by the ellipse is called the beam emittance ε defined by

$$\int_{ellipse} \mathrm{d}x \; \mathrm{d}x' = \pi\varepsilon \tag{5.31}$$

while the parameters α, β, and γ determine the shape and orientation of the ellipse. In linear optics all particles stay on their individual ellipses in phase space. If one tracks those particles on the largest phase ellipse within a particular beam, all other particles within that ellipse will stay within that ellipse. One is thereby able to describe the collective behavior of a beam formed by many particles by the dynamics of a single particle.

Since all particles enclosed by a phase ellipse stay within that ellipse, one only needs to know how the ellipse parameters transform along the beam line to be able to describe the

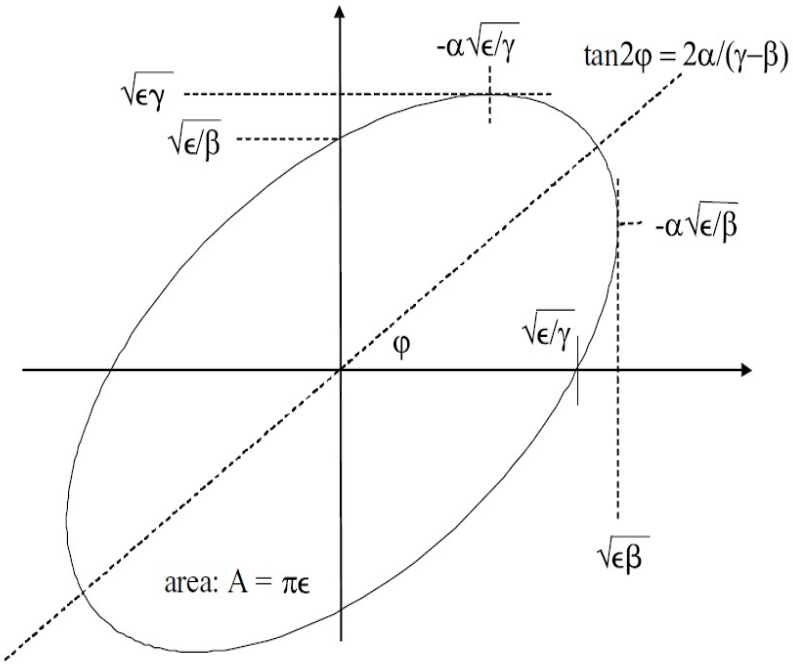

FIG. 61: The phase space defines the beam envelope.

whole particle beam. Let the equation

$$\gamma_0 x_0^2 + 2\alpha_0 x_0 x_0' + \beta_0 x_0' = \varepsilon \tag{5.32}$$

be the equation of the phase ellipse at the starting point $s = 0$ of the beam line. Any particle trajectory transforms from the starting point $s = 0$ to any other point $s \neq 0$ by the transformation

$$\begin{pmatrix} x(s) \\ x'(s) \end{pmatrix} = \begin{pmatrix} C(s) & S(s) \\ C'(s) & S'(s) \end{pmatrix} \begin{pmatrix} x_0 \\ x_0' \end{pmatrix}. \tag{5.33}$$

Solving for x_0 and x_0' and inserting into (5.32), one gets after sorting of coefficients and stopping to show explicitly the s-dependence

$$\begin{aligned} \varepsilon =& (C'^2\beta_0 - 2S'C'\alpha_0 + S'^2\gamma_0)x^2 \\ &+ 2(-CC'\beta_0 + S'C\alpha_0 + SC'\alpha_0 - SS'\gamma_0)xx' \\ &+ (C^2\beta_0 - 2SC\alpha_0 + S^2\gamma_0)x'^2 \end{aligned} \tag{5.34}$$

This equation can be brought into the form (5.30) by replacing the coefficients in (5.34) with

$$\begin{aligned}\gamma &= C'^2\beta_0 - 2S'C'\alpha_0 + S'^2\gamma_0,\\ \alpha &= -CC'\beta_0 + (S'C + SC')\alpha_0 - SS'\gamma_0,\\ \beta &= C^2\beta_0 - 2SC\alpha_0 + S^2\gamma_0,\end{aligned} \tag{5.35}$$

and using the fact that the transformation matrices all have unity determinate [11].

The resulting ellipse equation still has the same area $\pi\varepsilon$ as we would expect, but due to different parameters α, β, γ, the new ellipse has a different orientation and shape. During a transformation along a beam transport line the phase ellipse will continuously change its form and orientation but not its area. In matrix formulation the ellipse parameters, which are also called Twiss parameters, from (5.35) transform as

$$\begin{pmatrix}\beta(z)\\ \alpha(z)\\ \gamma(z)\end{pmatrix} = \begin{pmatrix} C^2 & -2CS & S^2\\ -CC' & CS' + C'S & -SS'\\ C'^2 & -2C'S' & S'^2\end{pmatrix}\begin{pmatrix}\beta_0\\ \alpha_0\\ \gamma_0\end{pmatrix}. \tag{5.36}$$

The orientation, eccentricity, and area of an ellipse is defined by three parameters, while (5.32) includes four parameters α, β, γ, and ε. Since the area is defined by ε one expects the other three parameters to be correlated. From geometric properties of an ellipse one finds that correlation to be

$$\beta\gamma - \alpha^2 = 1. \tag{5.37}$$

The above derivation for the (x, x')-phase space, is also valid for the (y, y')-phase space. Equation (5.35) provides the tool to calculate beam parameters anywhere along the beam line from the initial values β_0, α_0, γ_0.

The phase ellipse in a drift space, for example, becomes distorted in a clock wise direction without changing the slope of any particle as shown in Figure 62. If the drift space is long enough, a convergent beam eventually transforms into a divergent beam, while the angular envelope $x'_{max} = \sqrt{\varepsilon\gamma}$ stays constant.

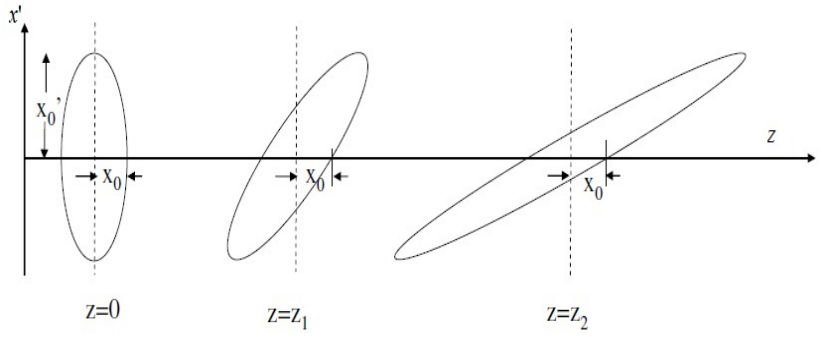

FIG. 62: Development of the phase space distribution through a drift space.

5.5 BEAM MATRIX

Particle beams are conveniently described in phase space by enclosing their distribution with ellipses. The equation for an n-dimensional ellipse can be written in the form

$$u^T \sigma^{-1} u = 1, \tag{5.38}$$

where σ is beam matrix, u^T is the transpose of the coordinate vector u defined by

$$u = \begin{pmatrix} x \\ x' \\ y \\ y' \\ \tau \\ \delta \\ . \\ . \\ . \end{pmatrix}. \tag{5.39}$$

The volume of this n-dimensional ellipse is [11]

$$V_n = \frac{\pi^{n/2}}{\Gamma(1+n/2)} \sqrt{\det\sigma}, \tag{5.40}$$

where Γ is the gamma function.

For the two-dimensional phase space the ellipse equation is

$$u^T\sigma^{-1}u = \begin{pmatrix} x & x' \end{pmatrix} \begin{pmatrix} \sigma_{11} & \sigma_{12} \\ \sigma_{21} & \sigma_{22} \end{pmatrix}^{-1} \begin{pmatrix} x \\ x' \end{pmatrix} = 1. \tag{5.41}$$

Since $\sigma_{12} = \sigma_{21}$ this can be written

$$\sigma_{22}x^2 - 2\sigma_{12}xx' + \sigma_{11}x'^2 = \det\sigma. \tag{5.42}$$

Comparing this to equation (5.32) yields the following relationships between the Twiss parameters and the beam matrix

$$\sigma = \begin{pmatrix} \sigma_{11} & \sigma_{12} \\ \sigma_{21} & \sigma_{22} \end{pmatrix} = \varepsilon_x \begin{pmatrix} \beta_x & -\alpha_x \\ -\alpha_x & \gamma_x \end{pmatrix}. \tag{5.43}$$

The two-dimensional "volume" or phase space area is

$$V_2 = \pi\sqrt{\det\sigma} = \pi\sqrt{\sigma_{11}\sigma_{22} - \sigma_{22}^2} = \pi\varepsilon_x. \tag{5.44}$$

For the homogeneous differential equation 5.2, the solution for a particular particle and its derivative can be described in amplitude-phase form as

$$x_i = a_i\sqrt{\beta}\cos(\psi + \psi_i), \tag{5.45}$$

$$x_i' = a_i\frac{\beta'}{2\sqrt{\beta}}\cos(\psi + \psi_i) - a_i\frac{1}{\sqrt{\beta}}\sin(\psi + \psi_i). \tag{5.46}$$

Using this solution one can define the Twiss parameters in terms of the statistic properties of beam distribution. First average the values of all particles within a well-defined fraction of a beam and obtain

$$\begin{aligned} \langle x_i^2\rangle &= a_i^2\beta\langle\cos^2(\psi + \psi_i)\rangle = \frac{1}{2}a_i^2\beta = \varepsilon\beta, \\ \langle x_i'^2\rangle &= \frac{1}{2}a_i^2\frac{\alpha^2}{\beta} + \frac{1}{2}a_i^2\frac{1}{\beta} = \frac{1}{2}a_i^2\frac{1+\alpha^2}{\beta} = \varepsilon\gamma, \\ \langle x_i x_i'\rangle &= -\frac{1}{2}a_i^2\alpha = -\varepsilon\alpha, \end{aligned} \tag{5.47}$$

where a Gaussian particle distribution is assumed and a beam emittance is defined by $\varepsilon = \frac{1}{2}a_i^2$, $\alpha = \frac{1}{2}\beta'$, and $\gamma = (1+\alpha^2)/\beta$. This definition describes the beam distributions in terms of standard deviation quantities in phase space. The beam matrix elements become

$$\begin{aligned} \sigma_{11} &= \langle x_i^2\rangle = \varepsilon\beta, \\ \sigma_{22} &= \langle x_i'^2\rangle = \varepsilon\gamma, \\ \sigma_{12} &= \langle x_i x_i'\rangle = -\varepsilon\alpha. \end{aligned} \tag{5.48}$$

With this definition, the so-called *rms* beam emittance is

$$\varepsilon^2 = \sigma_{11}\sigma_{22} - \sigma_{12}^2 = \langle x_i^2 \rangle \langle x_i'^2 \rangle - \langle x_i x_i' \rangle^2. \tag{5.49}$$

The transfer matrix, M, for the transverse x plane that describes the particle motion through a beamline consisting of non dispersive elements is given by

$$\begin{pmatrix} x_f \\ x_f' \end{pmatrix} = \begin{pmatrix} M_{11} & M_{12} \\ M_{21} & M_{22} \end{pmatrix} \begin{pmatrix} x_i \\ x_i' \end{pmatrix}. \tag{5.50}$$

Using the identities $I = R^{-1}R = R^T(R^T)^{-1}$ and inserting into equation 5.41 at the initial starting position, it yields

$$\begin{aligned} x_i^T(M^T(M^T)^{-1})\sigma_i^{-1}(M^{-1}M)x_i &= 1 \\ (x_i^T M^T)((M^T)^{-1}\sigma_i^{-1}M^{-1})(Mx_i) &= 1 \\ (Mx_i)^T(M^T\sigma_i M)^{-1}(Mx_i) &= 1 \\ x_f^T(M\sigma_i M^T)^{-1}x_f &= 1 \end{aligned} \tag{5.51}$$

Therefore the beam matrix at the final position, f, is given by

$$\sigma_f = M\sigma_i M^T. \tag{5.52}$$

Equation 5.52 is useful for the experimental measurement of beam emittances.

5.6 BEAM EMITTANCE

Emittance is a property of a charged particle beam in a particle accelerator. It is a measure for the average spread of particle coordinates in position-and-momentum phase space and has the dimension of length times angle (meters times radians).

Emittance is used to describe a beam because unlike the physical dimensions of the beam, which vary with location in an accelerator, emittance is invariant in the absence of dissipative or cooling forces. Sometimes motion in each plane (2 transverse, 1 longitudinal) is very weakly coupled; in this case it may be possible to treat the motion in each plane independently. Only the transverse beam emittances will be studied.

5.6.1 STATISTICAL DEFINITION OF EMITTANCE

A statistical definition of the phase space normalized (n) *rms* emittance is given by equation

$$\varepsilon_{n,x,rms} = \frac{1}{m_0 c}\sqrt{\langle x^2 \rangle \langle p_x^2 \rangle - \langle x p_x \rangle^2} \tag{5.53}$$

where m_0 is the electron rest mass, c is the speed of light, and

$$\begin{aligned}
\langle x^2 \rangle &= \frac{1}{n}\sum_{i=1}^{n} x_i^2 - \left(\frac{1}{n}\sum_{i=1}^{n} x_i\right)^2, \\
\langle p_x^2 \rangle &= \frac{1}{n}\sum_{i=1}^{n} p_{x,i}^2 - \left(\frac{1}{n}\sum_{i=1}^{n} p_{x,i}\right)^2, \\
\langle x p_x \rangle &= \frac{1}{n}\sum_{i=1}^{n} x_i p_{x,i} - \frac{1}{n^2}\left(\sum_{i=1}^{n} x_i \sum_{i=1}^{n} p_{x,i}\right).
\end{aligned} \tag{5.54}$$

for a discrete distribution, or

$$\begin{aligned}
\langle x^2 \rangle &= \frac{\int x^2 \varrho(x,p_x) dx dp_x}{\int \varrho(x,p_x) dx dp_x} - (\frac{\int x \varrho(x,p_x) dx dp_x}{\int \varrho(x,p_x) dx dp_x})^2, \\
\langle p_x^2 \rangle &= \frac{\int p_x^2 \varrho(x,p_x) dx dp_x}{\int \varrho(x,p_x) dx dp_x} - (\frac{\int p_x \varrho(x,p_x) dx dp_x}{\int \varrho(x,p_x) dx dp_x})^2, \\
\langle x p_x \rangle &= \frac{\int x p_x \varrho(x,p_x) dx dp_x}{\int \varrho(x,p_x) dx dp_x} - \frac{\int x \varrho(x,p_x) dx dp_x \int p_x \varrho(x,p_x) dx dp_x}{(\int \varrho(x,p_x) dx dp_x)^2},
\end{aligned} \tag{5.55}$$

for a continuous distribution $\varrho(x,y)$. These expressions assume that the average values of $\langle x \rangle$ and $\langle p_x \rangle$ vanish.

5.6.2 TRACE SPACE EMITTANCE

Experimentally one normally measures x', y' instead of the transverse momenta. Inserting identity $x' = p_x/p_z$ and $y' = p_y/p_z$ into Equation 5.53 one can get the normalized trace space (tr) emittance assuming a small energy spread

$$\varepsilon_{n,x,tr,rms} = \frac{\langle p_z \rangle}{m_0 c}\sqrt{\langle x^2 \rangle \langle x'^2 \rangle - \langle x x' \rangle^2}, \tag{5.56}$$

and the trace space emittance is

$$\varepsilon_{x,tr,rms} = \sqrt{\langle x^2 \rangle \langle x'^2 \rangle - \langle x x' \rangle^2}. \tag{5.57}$$

They differ by the relativistic factor $\beta\gamma$ for the beam.

5.6.3 THERMAL EMITTANCE

The thermal emittance is present at the cathode and imposes a lower limit for the normalized emittance that can be achieved by an injector. The normalized *rms* thermal emittance depends on the emitting area, the momentum distribution, and the angular distribution of

the emitted electrons. The energy and divergence distributions are functions of the cathode material and photon energy.

The thermal emittance can be calculated by assuming the electrons from the cathode are emitted uniformly and isotropically, within a radius r in the presence of an accelerating field. The angular distribution, x', has a Maxwell-Boltzmann distribution and $\langle x'^2 \rangle$ can be calculated as $kT/(mc^2)$, where the cathode is at a temperature T, and $\langle x^2 \rangle = \sigma_0^2 = r^2/4$ [16]. Inserting into Equation 5.58 with $\langle xx' \rangle = 0$, one gets

$$\varepsilon_{th,n,rms} = \sigma_0 \sqrt{\frac{kT}{m_0 c^2}}, \tag{5.58}$$

where σ_0 is the rms size of the emitting area, kT the average thermal energy, m_0 the rest mass of electron, and c the speed of light. At room temperature 25 °C, $kT = 25.7 \times 10^{-3}$ eV, and $m_0 c^2 = 0.511 \times 10^6$ eV one obtains

$$\sqrt{\frac{kT}{m_0 c^2}} = 0.224 \times 10^{-3} \quad \text{rad} = 0.224 \quad \text{mrad}. \tag{5.59}$$

5.6.4 NORMALIZED EMITTANCE

When a beam accelerates, the transverse beam size shrinks. The idea of invariant emittance is still possible if the emittance is scaled according to the beam energy, $\varepsilon_n = \beta\gamma\varepsilon$, where β and γ are the relativistic parameters defined by the beam energy. The normalized emittance, ε_n, is then constant as a beam changes energy. A qualitative idea of the source of the shrinking beam can be seen in Figure 63.

The transverse angles before and after acceleration are given by the following

$$\begin{aligned} x'_0 &= \frac{P_t}{P_0}, \\ x' &= \frac{P_t}{P_0 + eV/c} = \frac{P_t}{P}, \end{aligned} \tag{5.60}$$

where e is the basic unit of electrical charge, c the speed of light, x'_0 and x' transverse angle, P_0 the initial longitudinal momentum, P_t the transverse momentum, P the momentum after the acceleration, and V the accelerating voltage. Since $P_0 < P_0 + eV/c$ therefore $x' < x'_0$, demonstrating that the size of the beam in transverse phase space shrinks with acceleration.

For the case of a relativistic beam, $P \simeq P_{total}$, and

$$x' = \frac{P_t}{P_{total}} = \frac{P_t}{m_0 c \beta\gamma}, \tag{5.61}$$

where m_0 is the rest mass of electron.

Since x' scales as $\frac{1}{\beta\gamma}$ from acceleration, to recover an invariant emittance it is necessary to multiply by a factor of $\beta\gamma$. This relationship will be verified using the experimental data.

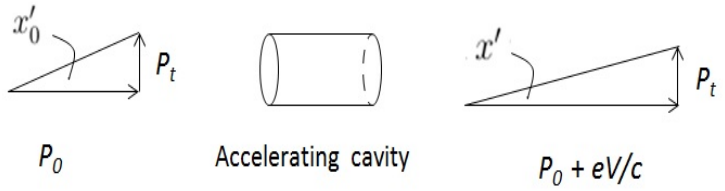

FIG. 63: Acceleration affects beam emittance: x' shrinks due to acceleration.

5.7 MEASURING BEAM EMITTANCE

The beam emittance quantifies both the beam size and the divergence of particles in the beam. While one is able to measure the beam size using a viewer screen or a wire scanner, for example, the beam divergence cannot be measured directly. If, however, the beam size is measured under different focusing conditions such that different parts of the ellipse will be probed by the beam size monitor, the beam emittance can be determined.

From Equation 5.52 the first beam matrix element gives

$$\sigma_{f,11} = M_{11}^2\sigma_{i,11} + 2M_{11}M_{12}\sigma_{i,12} + M_{12}^2\sigma_{i,22}. \tag{5.62}$$

If one has a solenoid (or a quadruple) at P_0 and a viewer (or a wire scanner) at downstream P_1, one can vary the strength of the solenoid and measure the beam size at P_1 as a function of the solenoid strength. The results of n beam size measurements can be expressed by the matrix equation

$$\begin{pmatrix} \sigma_{1,11} \\ \sigma_{2,11} \\ . \\ . \\ . \\ \sigma_{n,11} \end{pmatrix} = \begin{pmatrix} C_1^2 & 2C_1S_1 & S_1^2 \\ C_2^2 & 2C_2S_2 & S_2^2 \\ . & . & . \\ . & . & . \\ . & . & . \\ C_n^2 & 2C_nS_n & S_n^2 \end{pmatrix} \begin{pmatrix} \sigma_{0,11} \\ \sigma_{0,12} \\ \sigma_{0,22} \end{pmatrix} = M_{\sigma,n} \begin{pmatrix} \sigma_{0,11} \\ \sigma_{0,12} \\ \sigma_{0,22} \end{pmatrix}. \tag{5.63}$$

The solution of Equation 5.63 is from simple matrix multiplications

$$\begin{pmatrix} \sigma_{0,11} \\ \sigma_{0,12} \\ \sigma_{0,22} \end{pmatrix} = (M_{\sigma,n}^T M_{\sigma,n})^{-1} M_{\sigma,n}^T \begin{pmatrix} \sigma_{1,11} \\ \sigma_{2,11} \\ . \\ . \\ . \\ \sigma_{n,11} \end{pmatrix} \tag{5.64}$$

Then one can use Equation 5.44 to calculate the emittance of location P_0.

Practically, the evaluation of Equation 5.64 is performed by measuring the beam size $\sigma_{1,11}(K)$ at P_1 as a function of the solenoid strength K and comparing the results with the theoretical expectation, Equation 5.62.

Figure 64 is a simple setup that consists of a single solenoid and a viewer screen at a distance L. Assuming that the length of the solenoid is d, and $L \gg d$, so the thin lens approximation can be used, the total transformation matrix is

$$M = \begin{pmatrix} 1 & L \\ 0 & 1 \end{pmatrix} \begin{pmatrix} 1 & 0 \\ -1/f & 1 \end{pmatrix} = \begin{pmatrix} 1 - L/f & L \\ -1/f & 1 \end{pmatrix}, \tag{5.65}$$

where $f = -\dfrac{1}{Kd}$ is the focal length of the solenoid, and K is the strength of the solenoid. Equation 5.62 becomes

$$\sigma_{1,11}(K) = (1 + dKL)^2 \sigma_{0,11} + 2(1 + dKL)d\sigma_{0,12} + L^2 \sigma_{0,22}. \tag{5.66}$$

After reordering the terms

$$\sigma_{1,11}(K) = (L^2 \sigma_{0,11})(dK)^2 + 2(L\sigma_{0,11} + L^2 \sigma_{0,12})(dK) + (\sigma_{0,11} + 2L\sigma_{0,12} + L^2 \sigma_{0,22}). \tag{5.67}$$

Or one can change Equation 5.67 to

$$\sigma_{1,11}(f) = (L^2 \sigma_{0,11})(1/f)^2 + 2(L\sigma_{0,11} + L^2 \sigma_{0,12})(1/f) + (\sigma_{0,11} + 2L\sigma_{0,12} + L^2 \sigma_{0,22}). \tag{5.68}$$

Fitting $\sigma_{1,11}$ with a parabola

$$\sigma_{1,11} = ax^2 + bx + c \tag{5.69}$$

determines the whole beam matrix σ_0 by

$$\begin{aligned} \sigma_{0,11} &= \frac{a}{L^2}, \\ \sigma_{0,12} &= \frac{b - 2L\sigma_{0,11}}{2L^2}, \\ \sigma_{0,22} &= \frac{c - \sigma_{0,11} - 2L\sigma_{0,12}}{L^2}. \end{aligned} \tag{5.70}$$

By inserting Equation 5.70 into Equation 5.44 one can calculate the emittance of location P_0. The beam matrix not only defines the beam emittance but also the betatron functions

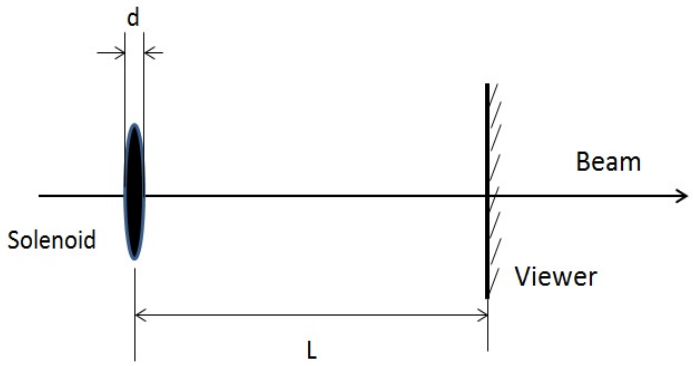

FIG. 64: An emittance measurement setup consists of a solenoid and a viewer ($L \gg d$).

at the beginning of the solenoid in this measurement. With this measurement one gets a full set of initial beam parameters $\alpha_0, \beta_0, \gamma_0, \varepsilon$, and can calculate beam parameters at any point along the transport line thereafter using the transformation matrix.

5.7.1 FITTING OF THE MEASURED DATA

In order to be less sensitive to measurement errors, it is preferable to measure σ_{11} in Equation 5.68, for more than three different transformations and then to find a solution for the beam matrix elements. This can be done using the chi-square (χ^2) method [17] [18]. According to the χ^2 method the best fit is obtained by minimizing the expression

$$\chi^2 = \sum_{i=1}^{N} \left(\frac{f(x_i, \alpha) - y_i}{\sigma_{y,i}}\right)^2, \tag{5.71}$$

where $f(x_i, \alpha)$ is the fit model, x_i is the measured set point, y_i is the measured function value, and $\sigma_{y,i}$ is the estimated error of y_i. α stands for the free parameters of the fit model, and N is the number of data points. Or explicitly, using Equations 5.67 and 5.69:

$$f(x_i, \alpha) = ax_i^2 + bx_i + c, \tag{5.72}$$

where α is the fit parameter a, b, and c, x_i is the solenoid strength, y_i is the measured value $\sigma_{1,11}$, and $\sigma_{y,i}$ is the estimated error of $\sigma_{1,11}$.

5.7.2 ERROR ESTIMATION OF THE FITTED PARAMETERS

The statistical error in the calculated emittance was determined by finding the statistical error in the beam size measurements and propagating that error through the calculations.

Using Equation 5.48 on page 74 and Equation 5.62 on page 78 one obtains

$$\langle x^2 \rangle = M_{11}^2 \langle x_0^2 \rangle + 2M_{11}M_{12}\langle x_0 x_0' \rangle + M_{12}^2 \langle x_0'^2 \rangle. \tag{5.73}$$

If there are n measurements in x,

$$\chi^2 = \sum_{i=1}^{n} \Big[\frac{\langle x_{(i)}^2 \rangle - f_i(\langle x_0^2 \rangle, \langle x_0 x_0' \rangle, \langle x_0'^2 \rangle)}{\sigma^2_{\langle x_{(i)}^2 \rangle}} \Big]^2, \tag{5.74}$$

where $\sigma_{\langle x_{(i)}^2 \rangle}$ is the error of $\langle x_{(i)}^2 \rangle$, and

$$f_i(\langle x_0^2 \rangle, \langle x_0 x_0' \rangle, \langle x_0'^2 \rangle) = (M_{11}^{(i)})^2 \langle x_0^2 \rangle + 2M_{11}^{(i)} M_{12}^{(i)} \langle x_0 x_0' \rangle + (M_{12}^{(i)})^2 \langle x_0'^2 \rangle. \tag{5.75}$$

Equation 5.74 can written in a matrix form:

$$\chi^2 = \sum_{i=1}^{n} \Big[b_i - \sum_{j=1}^{3} B_{ij} a_j \Big]^2, \tag{5.76}$$

where

$$\boldsymbol{a} = \begin{pmatrix} \langle x_0^2 \rangle \\ \langle x_0 x_0' \rangle \\ \langle x_0'^2 \rangle \end{pmatrix}, \tag{5.77}$$

$$\boldsymbol{b} = \begin{pmatrix} \dfrac{\langle x_{(1)}^2 \rangle}{\sigma^2_{\langle x_{(1)}^2 \rangle}} \\ \dfrac{\langle x_{(2)}^2 \rangle}{\sigma^2_{\langle x_{(2)}^2 \rangle}} \\ . \\ . \\ . \\ \dfrac{\langle x_{(n)}^2 \rangle}{\sigma^2_{\langle x_{(n)}^2 \rangle}} \end{pmatrix}, \tag{5.78}$$

$$\boldsymbol{B} = \begin{pmatrix} \frac{(M_{11}^{(1)})^2}{\sigma_{\langle x_{(1)}^2 \rangle}} & \frac{2M_{11}^{(1)}M_{12}^{(1)}}{\sigma_{\langle x_{(1)}^2 \rangle}} & \frac{(M_{12}^{(1)})^2}{\sigma_{\langle x_{(1)}^2 \rangle}} \\ \frac{(M_{11}^{(2)})^2}{\sigma_{\langle x_{(1)}^2 \rangle}} & \frac{2M_{11}^{(2)}M_{12}^{(2)}}{\sigma_{\langle x_{(1)}^2 \rangle}} & \frac{(M_{12}^{(2)})^2}{\sigma_{\langle x_{(1)}^2 \rangle}} \\ . & . & . \\ . & . & . \\ . & . & . \\ \frac{(M_{11}^{(n)})^2}{\sigma_{\langle x_{(1)}^2 \rangle}} & \frac{2M_{11}^{(n)}M_{12}^{(n)}}{\sigma_{\langle x_{(1)}^2 \rangle}} & \frac{(M_{12}^{(n)})^2}{\sigma_{\langle x_{(1)}^2 \rangle}} \end{pmatrix}. \tag{5.79}$$

To minimized χ^2, the derivatives with respect to parameter a_1, a_2, and a_3 have to vanish:

$$\begin{pmatrix} \frac{\partial \chi^2}{\partial a_1} \\ \frac{\partial \chi^2}{\partial a_2} \\ \frac{\partial \chi^2}{\partial a_3} \end{pmatrix} = 2 \begin{pmatrix} \sum_{i=1}^{n} \sum_{j=1}^{3} B_{ij} B_{i1} a_j \\ \sum_{i=1}^{n} \sum_{j=1}^{3} B_{ij} B_{i2} a_j \\ \sum_{i=1}^{n} \sum_{j=1}^{3} B_{ij} B_{j3} a_j \end{pmatrix} - 2 \begin{pmatrix} \sum_{i=1}^{n} b_i B_{i1} \\ \sum_{i=1}^{n} b_i B_{i2} \\ \sum_{i=1}^{n} b_i B_{j3} \end{pmatrix} = \begin{pmatrix} 0 \\ 0 \\ 0 \end{pmatrix}. \tag{5.80}$$

This equation can be written as

$$\boldsymbol{B}^T \boldsymbol{b} = (\boldsymbol{B}^T \boldsymbol{B}) \boldsymbol{a}, \tag{5.81}$$

or

$$\boldsymbol{a} = (\boldsymbol{B}^T \boldsymbol{B})^{-1} \boldsymbol{B}^T \boldsymbol{b}. \tag{5.82}$$

The squared error of a function $g(x_1, x_2, ..., x_n)$ can be determined by error propagation as

$$\sigma_g^2 = \sum_{i=1}^{n} (\frac{\partial g}{\partial x_i})^2 \sigma_{x_i}^2 + \sum_{i=1}^{n} \sum_{j=1, j \neq i}^{n} (\frac{\partial g}{\partial x_i})^2 (\frac{\partial g}{\partial x_j})^2 \mathrm{cov}(i, j), \tag{5.83}$$

where the first sum represents the variance of the function g, the second sum is the contribution of the covariances. Using Equations 5.48 on page 74 and 5.49 on page 75, the beam Twiss parameter can be written as

$$\begin{pmatrix} \beta_{x_0} \\ \alpha_{x_0} \\ \varepsilon_{x_0, rms} \end{pmatrix} = \begin{pmatrix} a_1 / \sqrt{a_1 a_3 - a_2^2} \\ -a_2 / \sqrt{a_1 a_3 - a_2^2} \\ \sqrt{a_1 a_3 - a_2^2} \end{pmatrix}, \tag{5.84}$$

where a_1, a_2, and a_3 are the components of $\boldsymbol{a}$ (Equation 5.77). The variances and covariances of a_1, a_2, and a_3 are needed for the error calculation. The variance of a_k is

$$\sigma_{a_k}^2 = \sum_{i=1}^{n} (\frac{\partial a_k}{\partial \langle x_{(i)}^2 \rangle})^2 \sigma_{\langle x_{(i)}^2 \rangle}^2. \tag{5.85}$$

Using Equation 5.82 with the abbreviation $\boldsymbol{C} = (\boldsymbol{B}^T\boldsymbol{B})^{-1}$, one can write a_k as

$$a_k = \sum_{j=1}^{3} C_{kj}[\boldsymbol{B}^T\boldsymbol{b}]_j, \tag{5.86}$$

where $\boldsymbol{b}$ and $\boldsymbol{B}$ are given by Equations 5.78 and 5.79, respectively. The partial derivative of a_k with respect to $\langle x_{(i)}^2 \rangle$ is then

$$\frac{\partial a_k}{\partial \langle x_{(i)}^2 \rangle} = \frac{1}{\sigma_{\langle x_{(i)}^2 \rangle}} \sum_{j=1}^{3} C_{kj} B_{ij}. \tag{5.87}$$

Inserting Equation 5.87 into Equation 5.85 leads to the final result for the variance of a_k:

$$\begin{aligned}
\sigma_{a_k}^2 &= \sum_{i=1}^{n} (\sum_{j=1}^{3} C_{kj} B_{ij})^2 \\
&= \sum_{i=1}^{n} \sum_{j=1}^{3} \sum_{l=1}^{3} C_{kj} C_{kl} B_{ij} B_{il} \\
&= \sum_{j=1}^{3} \sum_{l=1}^{3} C_{kj} C_{kl} (\sum_{i=1}^{n} B_{ij} B_{il}) \\
&= \sum_{j=1}^{3} C_{kj} \sum_{l=1}^{3} C_{kj} [\boldsymbol{C}^{-1}]_{lj} \\
&= C_{kk}.
\end{aligned} \tag{5.88}$$

Equation 5.88 states that the diagonal elements of $\boldsymbol{C}$ are the variances of the fitted parameters a_i. It can be shown that the off-diagonal elements C_{ij} are the covariances between a_i and a_j. By knowing matrix $\boldsymbol{B}$, one can determine $\boldsymbol{C} = (\boldsymbol{B}^T\boldsymbol{B})^{-1}$, whose elements are the variances and covariances of the fitted parameters a_i. When the variances and covariances of the parameters a_1, a_2, and a_3 are known, one can calculate the errors of the emittance and of the Twiss parameters by applying Equation 5.83 to Equation 5.84.

CHAPTER 6

EMITTANCE AND LIFETIME MEASUREMENTS

After the photogun was built and successfully high voltage conditioned it is natural to conduct beam based studies. Other research groups have been studying topics related to high voltage DC photogun technology, beam emittance, and photocathode quantum efficiency. In particular, a Cornell university research group measured thermal emittance of a cesium potassium antimonide photocathode. The gun voltage was -230 kV. They reported that the measured thermal emittance was 0.56 $\pm$ 0.03 mm mrad [19] [20].

JLEIC requires high brightness and high current electron beams for its collider cooler. It is necessary to demonstrate that Jefferson Lab has the capability of providing the required electron beam. To achieve an electron beam of high brightness the beam emittance must be small. The beam emittance can be affected by the cathode electrode, the gun high voltage, and the photocathode materials. In order to sustain long delivery of high current beam, photocathodes must have long quantum efficiency lifetimes.

Thorough studies were performed using in-house made alkali antimonide photocathodes. The beam based studies concentrated on how the new gun design affects the beam transport and beam emittance. The beam based studies also examined other factors which affects beam emittance: bunch charge, gun bias voltage, laser spot size on the photocathode, and photocathode surface roughness. Photocathodes with different substrate materials (GaAs and molybdenum) were compared.

Ion bombardment is a major concern during high current beam operations because the beam-induced ions can travel into the photogun chamber and damage the photocathode. An effective way to prevent the beam-induced ions from entering the gun chamber was identified and implemented, which made high current runs a success.

In this chapter the measurement data of beam emittance, QE and QE lifetime, and high current are presented. The emittance data were taken using solenoid scan technique [21] [22]. The solenoid is 50.00 cm downstream of the photocathode. A downstream viewer and a wire scanner were used to measure the beam size. The distance between the solenoid and the wire scanner is 302.43 cm. The distance between the solenoid and the viewer is 326.55 cm.

6.1 PHOTOCATHODES

Table 3 shows the preparation conditions for six photocathodes studied in detail experimentally. Molybdenum and GaAs are the two materials used as substrates. The antimony

TABLE 3: Photocathodes.

Substrate	Sb deposition time (min)	Heating (A)	Active area (mm)	QE (%)
Moly	10	25	5	8.25
GaAs	10	25	12.8	5.17
GaAs	20	25	12.8	5.70
GaAs	30	25	5	5.23
GaAs	60	25	5	8.79
GaAs	90	25	5	6.30

deposition time is the duration of the deposition of Sb vapor onto the substrate when fabricating the photocathode. The heating current is the current applied to the antimony heater. The active area shows the diameter of active photocathode area. With a mask there are two sizes, 3 mm and 5 mm. Without the mask the active area would be the largest, with a diameter of 12.8 mm. Figure 65 shows the measured QE versus the Sb deposition time for

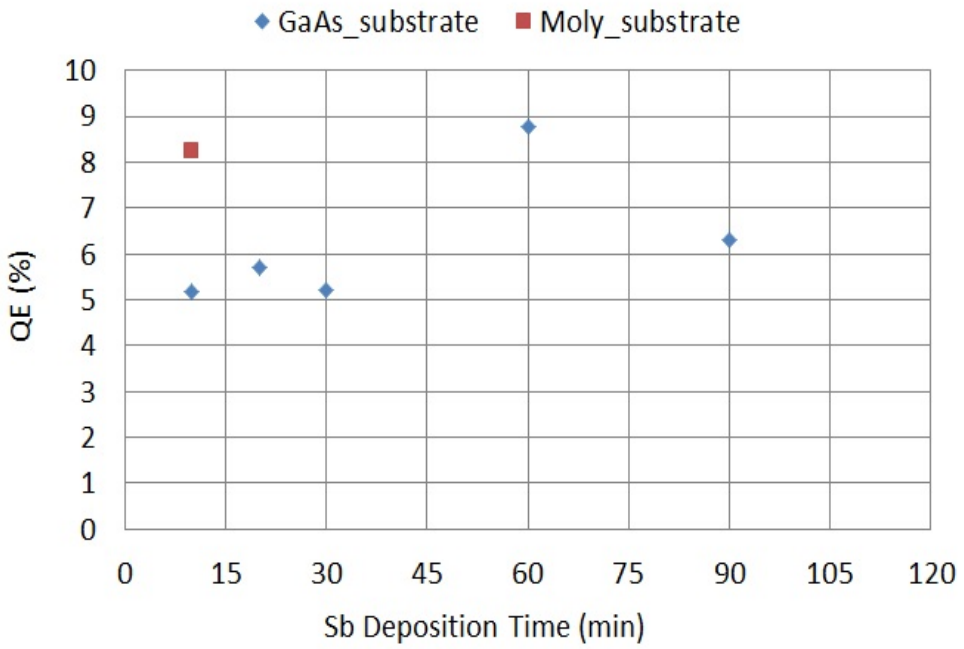

FIG. 65: QE vs. Sb deposition time.

for the six photocathodes. The QEs are the beam based values which are calculated using Equation 4.1 with the beam current delivered to the beam dump and the incident laser power. The measurement error is thus at the several percent level.

6.2 BEAM PREPARATION FOR THE EMITTANCE MEASUREMENTS

Beam preparation is important for the measurements. Since there are no beam position monitors along the beamline one relies on three viewers, the Faraday cup, and the beamline dump to make sure the beam transports well from the gun to the beam dump.

First, beam is steered to the center of the each viewer using upstream correctors. The center of a viewer is about the center of the beampime at that location. A well transported beam should be close to the center of the beampipe so any perturbation would not cause the beam to scrape the beampipe. Then beam is steered to the beam dump in a way that the current readbacks from the Faraday cup and beam dump are the same so there is no beam loss. Second, beam needs to be centered at each of the four lenses using upstream correctors and downstream viewers. When beam is centered at a lens, changing the lens setting will only change the size of the beam while the central position of the beam should remain fixed. A downstream viewer can monitor any position changes. After finishing the steps above one needs to send some CW beam, say, 10 μA, to the Faraday cup and the beam dump to make sure there is no beam loss. One may have to iterate the above steps a few times to achieve the lens centering and no-loss beam transport. When beam transports well to the beam dump the beamline vacuum should be stable as an elevation of the beamline vacuum is a good indication that the beam does not transport well.

Beam should also be centered in the Faraday cup and beam dump otherwise the current readbacks may not be accurate. Given the fact that the beam size is much smaller than the Faraday cup and beam dump it is very easy to achieve the beam centering on these two devices. In the GTS beamline the beam dump is about 80 cm downstream of the wire scanner and this is a very short distance. If beam is not well centered in the beam dump the wire scanner signal is noisy because the some electrons stimulate secondary emission which may collect on the wire scanner.

After beam transports well to the beam dump a wire scanner scan is checked to make sure the beam position is good for the wire scanner. If it is not, one needs to use the upstream correctors to adjust the beam position so wire scans show three well separated peaks, one for each wire. Figure 66 shows a typical wire scan result. There are three peaks detected,

one from each wire corresponding to x, u, and y axes, the rms beam sizes being 0.6017 mm, 0.5614 mm, and 0.6063 mm, respectively. In this case there is some noise between the peaks as indicated by the pedestal.

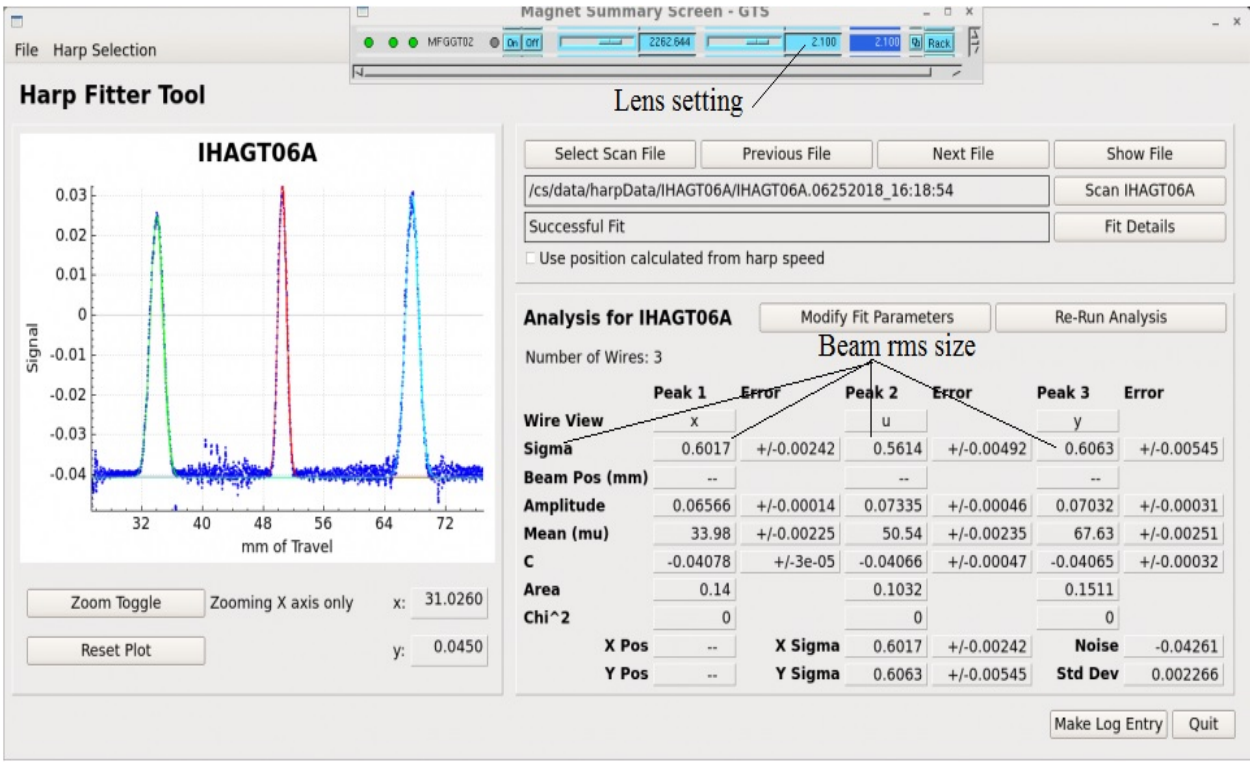

FIG. 66: A wire scan shows there are three peaks, with their rms sizes in x, u, and y axes.

After the beam is well tuned it may not stay tuned at all times. Conditions could change, especially after a run and all the systems are turned off. When the beam is turned back on again one must check conditions to make sure the beam is still good (no beam loss, no vacuum excursion, etc.) and make necessary adjustments when needed. Sometimes the beam orbit changes just after cycling a magnet. Sometimes after a photocathode is swapped the beam trajectory is different because the photocathode may not be seated exactly where it was previously. Ideally the photocathode surface is perpendicular to the beam line. Even a small angle error can change the beam trajectory. When this happens this error can be easily corrected using the first pair of correctors in the beamline.

The electron beam is formed by the photoemission of electrons with illumination of a laser onto a photocathode. The shape of the laser spot on the photocathode affects the beam shape. It is the best if the electron beam is round when it comes out of the photogun.

This requires that the laser beam spot on the photocathode is round. Through the optical lenses and mirrors the laser size and shape can be adjusted. A Spiricon laser beam profiler was used to measure the laser beam profile. The Spiricon reports the measured $1/e^2$ value, as shown in Figure 67. The rms laser size is a quarter of its $1/e^2$ value for Guassian conditions.

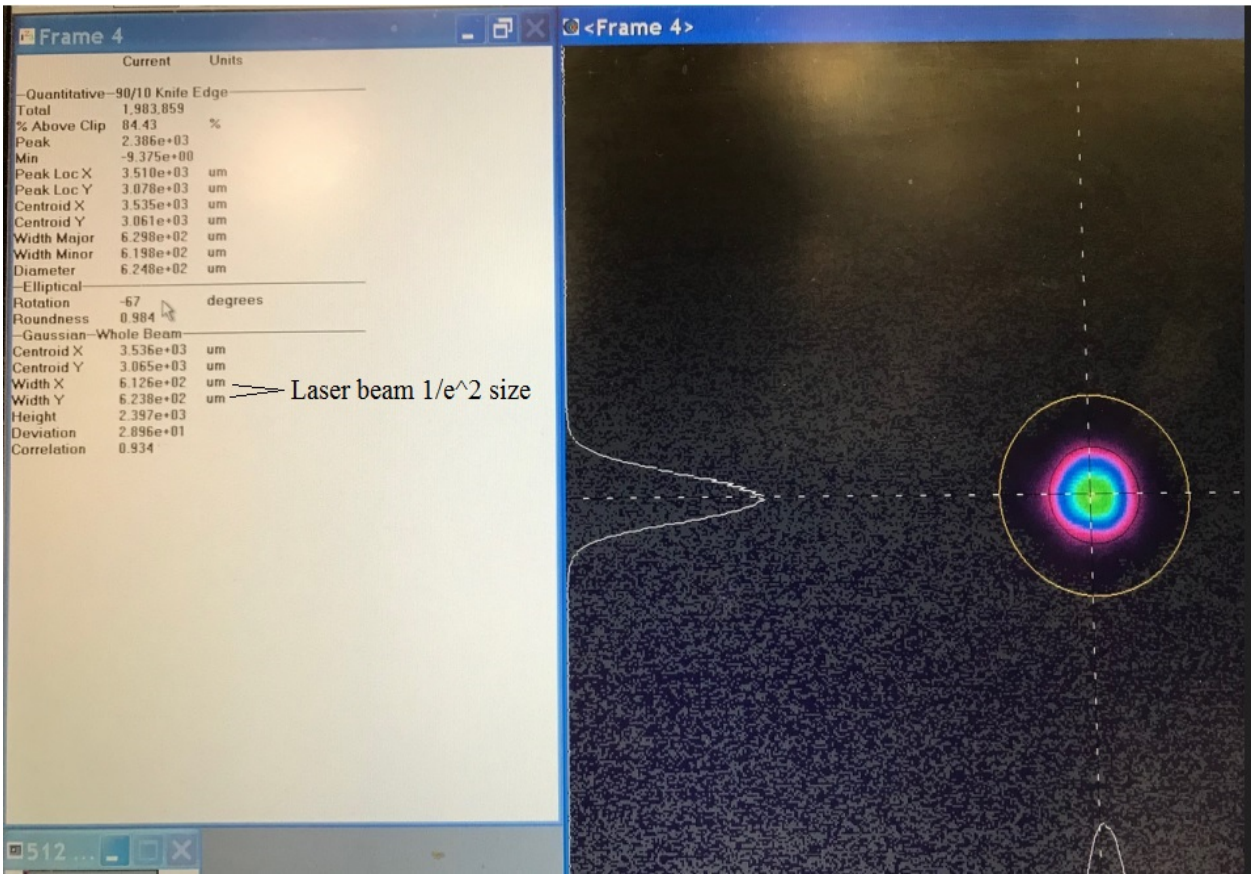

FIG. 67: The Spiricon software measures beam profile and reports its $1/e^2$ beam size.

When using the Spiricon laser beam profiler to measure a laser beam profile it is not possible to put the camera where the photocathode is since the photocathode is in the photogun vacuum chamber. At different location along the laser beam pass the profile would be different. This can be easily resolved by putting a beam splitter between the last optical lens and the photocathode and measuring the beam profile of the split laser beam. One needs to make sure that the distance between the Spiricon camera and the beam splitter is the same as that between the photocathode and the beam splitter.

The laser incident angle on the photocathode is 25°. When converting to the laser rms spot size on the photocathode in x plane, σ_x, the conversion factor $\cos 25° = 0.91$ should be

used. For the *rms* size in y plane, σ_y, the conversion factor is 1. In order to make a round electron beam the laser beam profile from the Spiricon profiler should have x and y ratio of 0.91 to 1.

After the laser size is set one can let the electron beam drift to a viewer, i.e., with all the lenses off. From the beam image on the viewer one can check the electron beam size in the x plane and y plane. If the electron beam is not round one can make adjustment to the laser beam profile until the electron beam is round. Figure 68 shows an electron beam on a viewer with its *rms* size $\sigma_x = 4.51$ mm, and $\sigma_y = 4.65$ mm.

When an electron beam is not round it may not be caused by the laser beam. Another thing can affect the electron beam shape is the location of the laser spot on the photocathode. The cathode front plate is not flat, as shown in Figure 18 on page 20. This is a design feature to make the electric field focus the electron beam. Due to this electric field distribution if the laser spot is too far away from the geometric center of the puck, i.e., very close to the edge of the opening of the cathode front plate, the electron beam symmetry may be affected. The opening of the cathode front plate has a diameter of 12.8 mm. If the laser spot location is within an area of diameter of 8 mm or smaller the electron is not affected, as shown by measurement in Section 6.5.

About 30 cm downstream of the wire scanner there is a viewer. This viewer can be used to set the scan range of the lens. During the emittance measurement only the scanning lens is on. All other three lenses are off. In order to find a scan range, one can set all the lenses to zero field and let beam drift to the viewer. Since all the lenses are set to zero field the beam size would very large. Then one can slowly increase the scanning lens setting. As the scanning lens setting goes up the size of the beam on the viewer becomes smaller. When the beam size becomes the smallest the setting of the scanning lens is roughly the mid point of the scan range. Using a step size, say 0.05 A, one can set a few points on either side of the mid point and measure the beam size at each lens setting using the viewer or the wire scanner. One then can feed each of the lens setting and its corresponding beam size to a ROOT program (see Appendix D) to calculate the beam emittance. Figure 69 shows a typical emittance calculated from a set of wire scans. Figure 69 (a) is for x plane and Figure 69 (b) for y plane. The top trace is beam *rms* size versus lens current squared and bottom trace is beam *rms* size squared versus the lens current squared with fit. From the plot one can check the scan quality. Figure 69 shows the plots are symmetric and the data points coincide with the fit. Therefore the scan is a good one. Table 4 shows the beam parameters, the normalized beam emittance, the thermal angle, α, β, and γ at the location where the

scanned lens is. Those parameters are reported on the lower right-hand side corner in Figure 69 from the ROOT program.

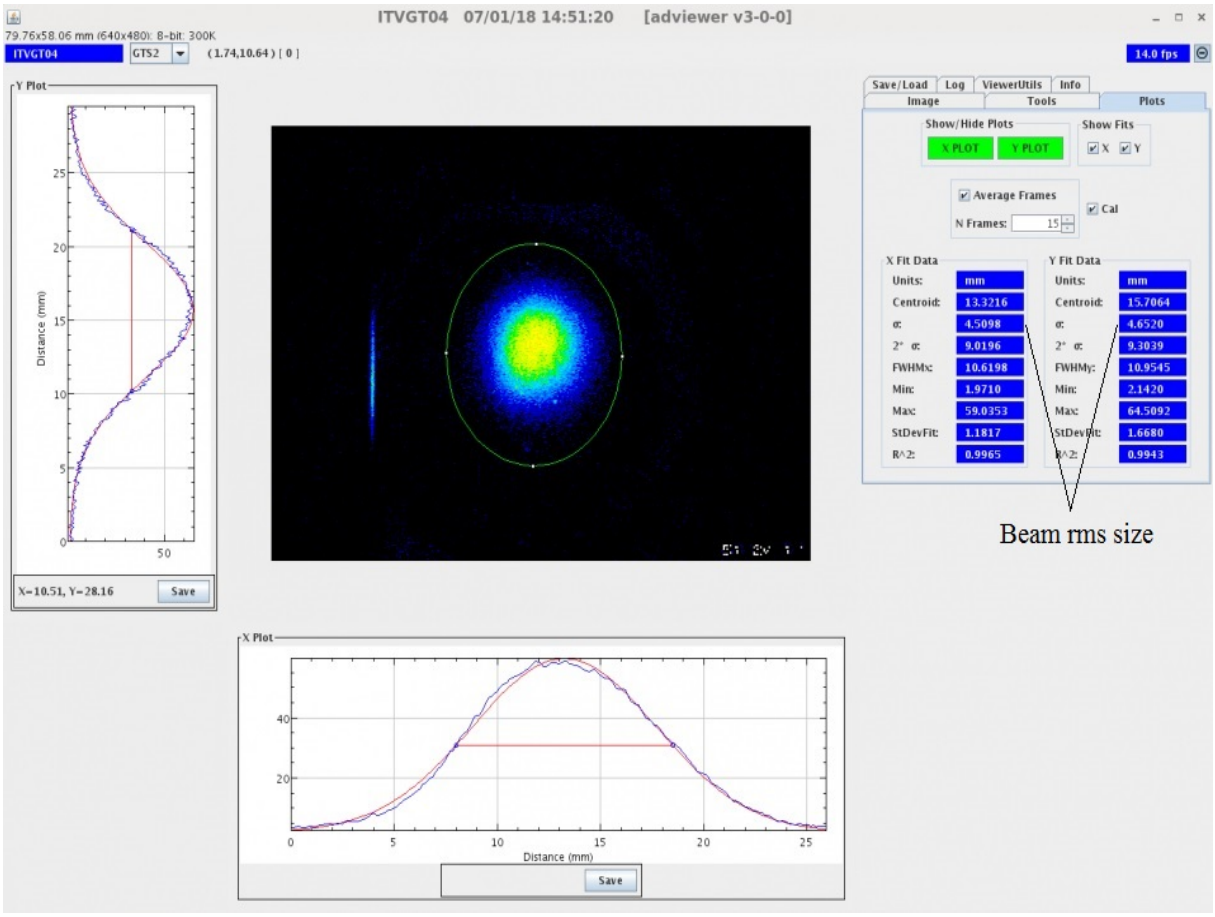

FIG. 68: An electron beam drifts to a viewer. All lenses are off.

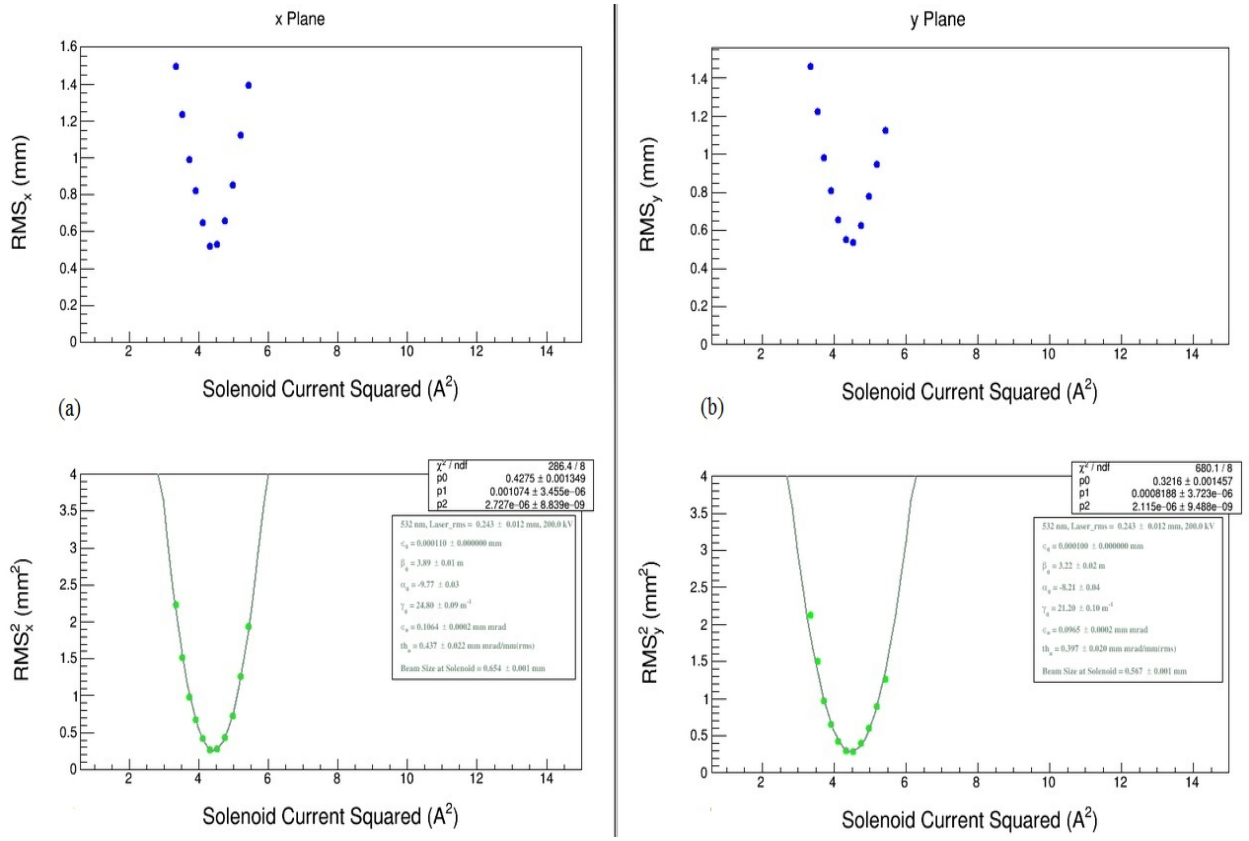

FIG. 69: Top: beam size vs solenoid current squared. Bottom: beam size squared vs solenoid current squared with fit (a) x plane (b) y plane.

TABLE 4: Calculated normalized emittance.

	ε_n(mm mrad)	Thermal angle(mm mrad/mm)	α	β	γ
x	0.1064±0.0002	0.437±0.022	-9.77±0.03	3.89±0.01	24.8±0.09
y	0.0965±0.0002	0.397±0.020	-8.21±0.04	3.22±0.02	21.2±0.10

6.3 BEAM EMITTANCE VS. BUNCH CHARGE OR BEAM CURRENT

This research focuses on the thermal emittance therefore a low bunch charge (current) beam was used to eliminate the space charge effect. The beam duty factor is 1.5%. In order to determine what was a good beam current to measure the thermal emittance, various beam

currents were used when measuring the beam emittance. Figure 70 (a) shows the normalized beam emittance versus bunch charge. Figure 70 (b) shows the normalized emittance versus

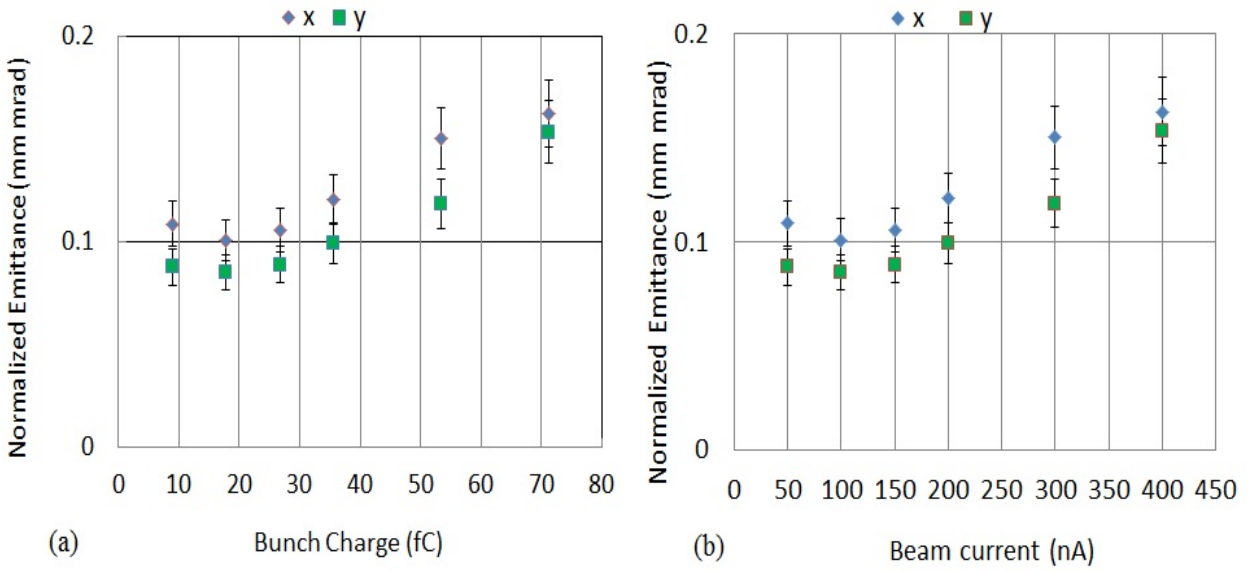

FIG. 70: Space charge affects beam emittance. (a) Emittance vs bunch charge. (b) Emittance vs beam current.

equivalent current. The condition for this measurement was that the laser *rms* size was 0.2 mm and a solenoid and a wire scanner were used. The gun high voltage was -200 kV. From the data one can tell 100 nA or 18 fC bunch charges is a good choice to measure the thermal emittance. Higher beam current or higher bunch charges creates the space charge effects as indicated by the dependence of measured emittance on charge. In this research all emittance data were taken using 100 nA tune mode beam (1.5% duty factor) when using a wire scanner to measure the beam sizes. When a viewer was used to measure the beam sizes the current is less than 2 nA tune mode beam otherwise the viewer would be saturated.

6.4 BEAM EMITTANCE VS. GUN HIGH VOLTAGE

The normalized beam emittances were measured at different gun high voltages while keeping all other conditions the same. As discussed in Section 5.6.4 on page 77 the normalized beam emittance should not vary with the gun high voltage as long as the beam is relativistic. Figure 71 shows the normalized emittance versus the gun high voltage. The normalized emittance becomes constant when the gun high voltage is higher than -200 kV.

This measurement justifies that -200 kV is used during subsequent measurements of beam emittance through this research; -200 kV is high enough that space charge effects are negligible. Figure 5.6.4 shows that the beam emittance changes with the voltage when the voltage is lower than -150 kV. This is because the beam is not relativistic yet when the voltage is below -150 kV. The measurement data in Figure 71 were taken with laser *rms* size of 0.31 mm.

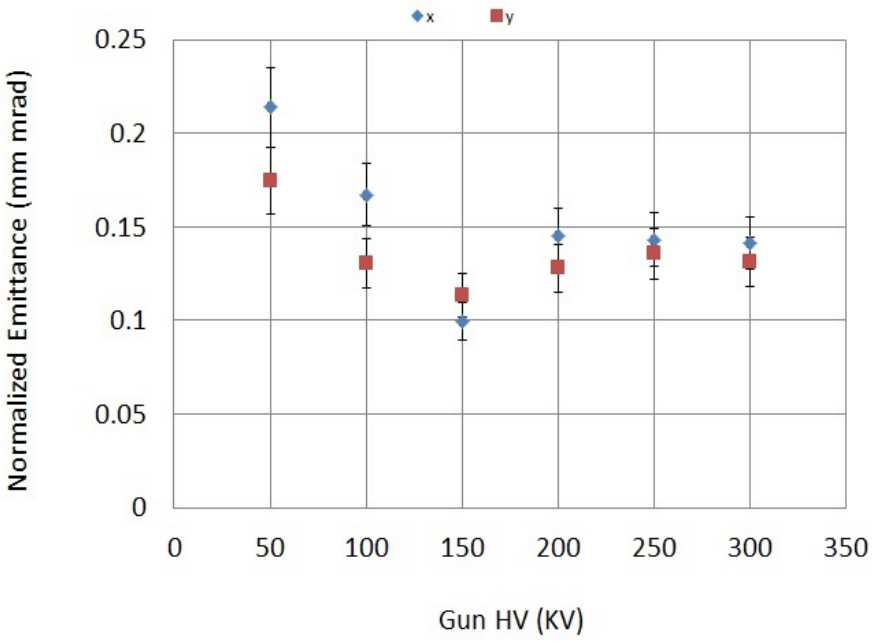

FIG. 71: The normalized emittance becomes constant when the gun HV is higher than 200 kV.

6.5 EMITTANCE ACROSS THE PHOTOCATHODE

In Section 3.1 the electric field symmetry was affected somewhat by the insulator and the shed. It was not clear how the beam quality was affected. A GPT simulation indicated that both x and y orbits were kicked but the beam would transport fine. The emittance measurements were done across the whole photocathode to check whether the beam emittance is affected by the asymmetry or not. A fully activated photocathode was used for this study; the diameter of the photocathode is 12.8 mm. The laser spot was put at the center of the photocathode first. Then the laser spot was moved up and down, and left and right

for a few points for each direction. The emittance was measured horizontally at nine points, and vertically at eight points. The data show that there was no obvious effect nearby the photocathode center. At the very edge of the photocathode the emittance is higher but this is expected because the electric field near the edge is altered by the cathode front face plate. Within the circular area of 3 mm radius the emittance is not affected. Also a simulation was done using the GPT. Figure 72 show the results: (a) is the x plane; (b) is y plane. One way

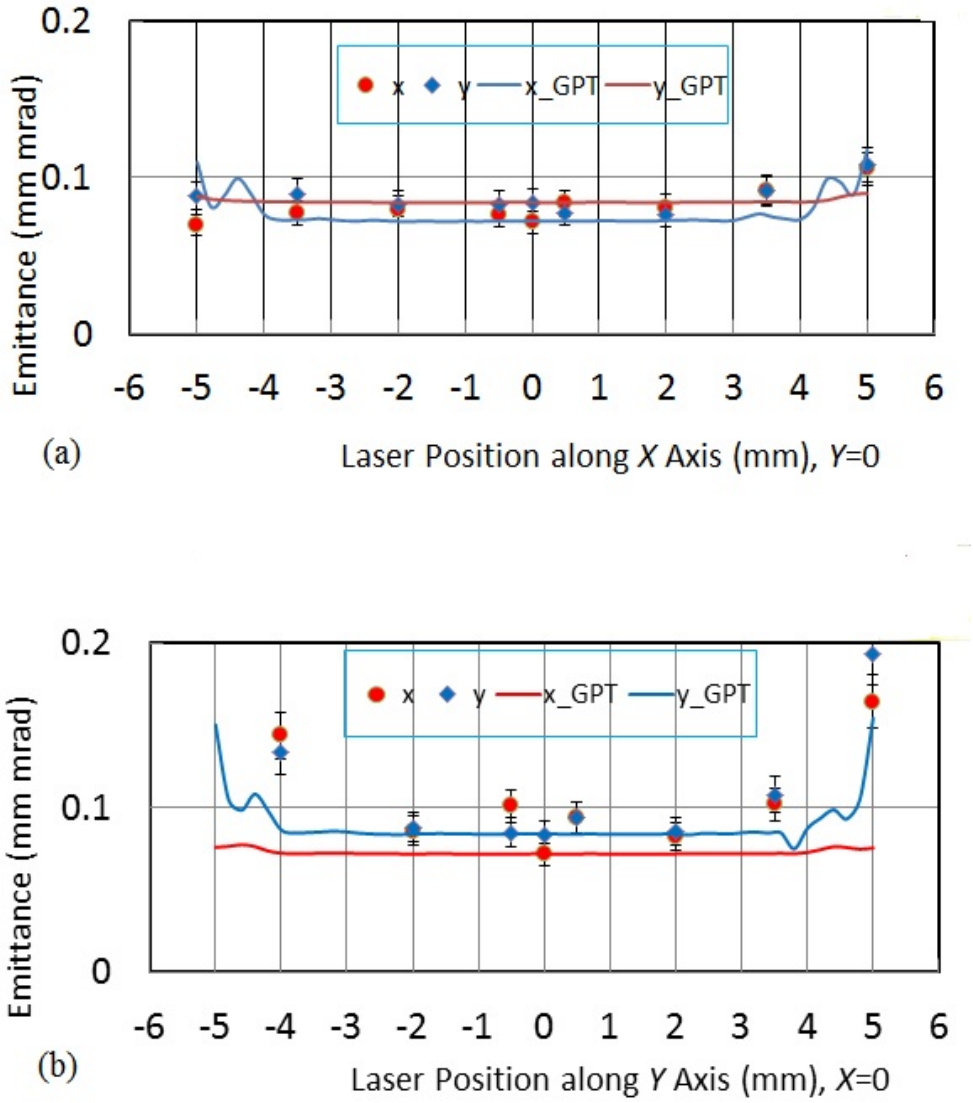

FIG. 72: The normalized emittance across a photocathode: (a) Horizontal scan, and (b) Vertical scan.

to explain the beam emittance is not affected is: the slight field symmetry change does not change the focusing aspect of the field between the photocathode and the anode; the symmetry change just slightly kicks beam as a whole.

6.6 EMITTANCE ACROSS A DAMAGED SPOT

During beam operations ions may be generated due to beam scraping the beampipe or other beamline components, or from beam hitting the beam dump. Even stray electrons, especially during high current runs, can generate numerous ions. Because the photogun is negatively biased those ions tend to travel towards the gun. Once an ion passes the anode it will hit the photocathode and the photocathode may be damaged from this ion bombardment.

Figure 73 shows there are more than a dozen damaged spots near the center of a photocathode: the white dots are the damaged spots. Their sizes are less than 1 mm $\times$ 1 mm. At a damaged spot the QE usually is lower than that of a normal spot, or in a worse case scenario, the QE drops to zero because the photocathode material is completely removed. Because the Cs_xK_ySb photocathodes are very robust, the QE at the undamaged portion is still good. In the case of GaAs photocathodes the QE is lost entirely.

FIG. 73: A photocathode was damaged due to ion back bombardment

Figure 74 shows a viewer image of a beam produced by a laser spot being on top of a damaged spot. The ring-shape image indicates that the laser spot overlaps the damaged spot and the QE in the center of the ring is very low. The ring is the edge of the damaged spot. To study how a damaged spot affects the beam emittance the incident laser spot on the photocathode was positioned on a damaged spot and adjacent to it. The emittance was measured at each location. Figure 75 shows the QEs and emittances on and near a damaged spot. Even through the QE dropped about 60% the emittance did not change much indicating that the beam angles at emission are not strongly influenced by photocathode damage. The estimated size of the damaged spot is about 0.9 mm $\times$ 0.8 mm. The laser rms size is 0.2 mm. For these measurements a viewer was used to measure the beam sizes while scanning the solenoid.

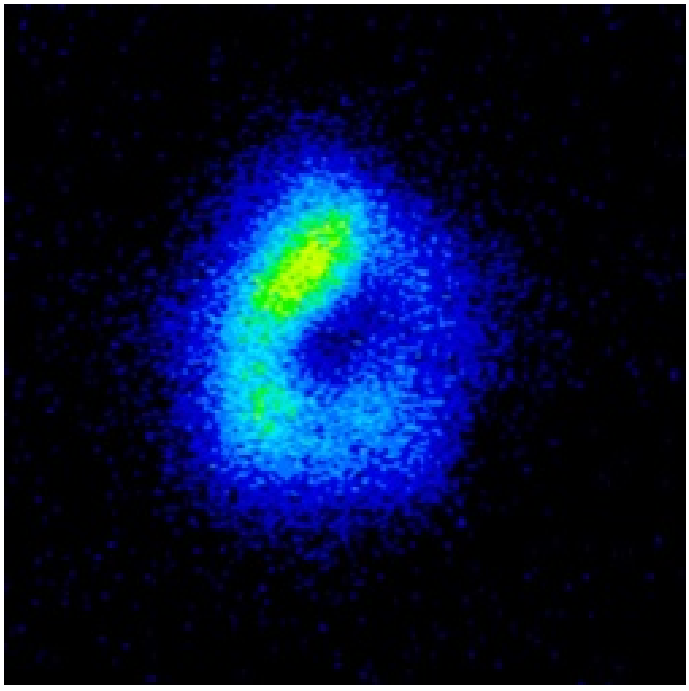

FIG. 74: A beam image from a damaged photocathode.

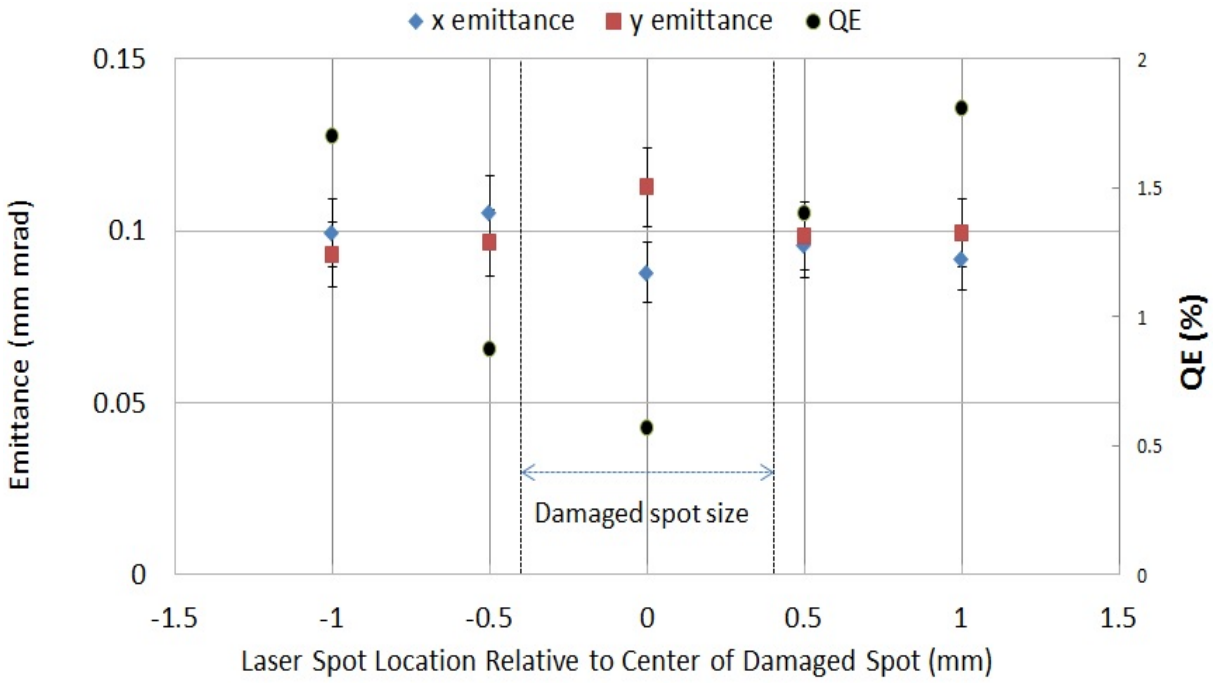

FIG. 75: QE and emittance were measured at and near a damaged spot on a photocathode.

6.7 EMITTANCE VERSUS LASER SPOT SIZE AND THICKNESS OF ANTIMONY LAYER

Six photocathodes were made: one with a molybdenum substrate, and five with GaAs substrates. Table 3 on page 85 shows the information on the photocathodes.

The incident laser spot size affects the electron beam emittance. The larger laser spot size makes the electron beam emittance larger. The emittance normalized to the laser spot size should remain the same although the laser size affects beam emittance. Often the emittance normalized to the laser spot size is called thermal angle. A plot of the emittance versus the laser spot size should be linear and the slope of the plot is the thermal angle. The laser spot rms size was set to 0.155, 0.256, 0.351, and 0.436 mm. At each laser spot size the beam emittance was measured for each photocathode. The figures in Figure 76 show the normalized beam emittances in the x plane and y plane versus the incident laser rms size. The plots are linear for each photocathode within errors. Also the slopes are close to each other.

It had been believed that the thickness of the Sb layer affects the beam emittance [23]. In general, the grain size and porosity of Sb films increase significantly with increasing

film thickness. The range for the grain size is from a few nanometers to a few hundred nanometers. The hypothesis tested in these measurements is that the thickness of the Sb layer affects the surface roughness of a photocathode. This surface roughness in turn affects the photoemission of electrons from the photocathode. The measurements directly address this topic. In Figure 76 the functions listed in the lower-right corner of each plot are the fit functions. The coefficients of the functions are the averaged thermal angle of the electron beam from each photocathode. Figure 77 shows a plot of the thermal angle versus the Sb deposition time. The plot includes both x plane and y plane thermal angles. The thermal angles do not appear to change much with the Sb deposition time. As the thickness of the

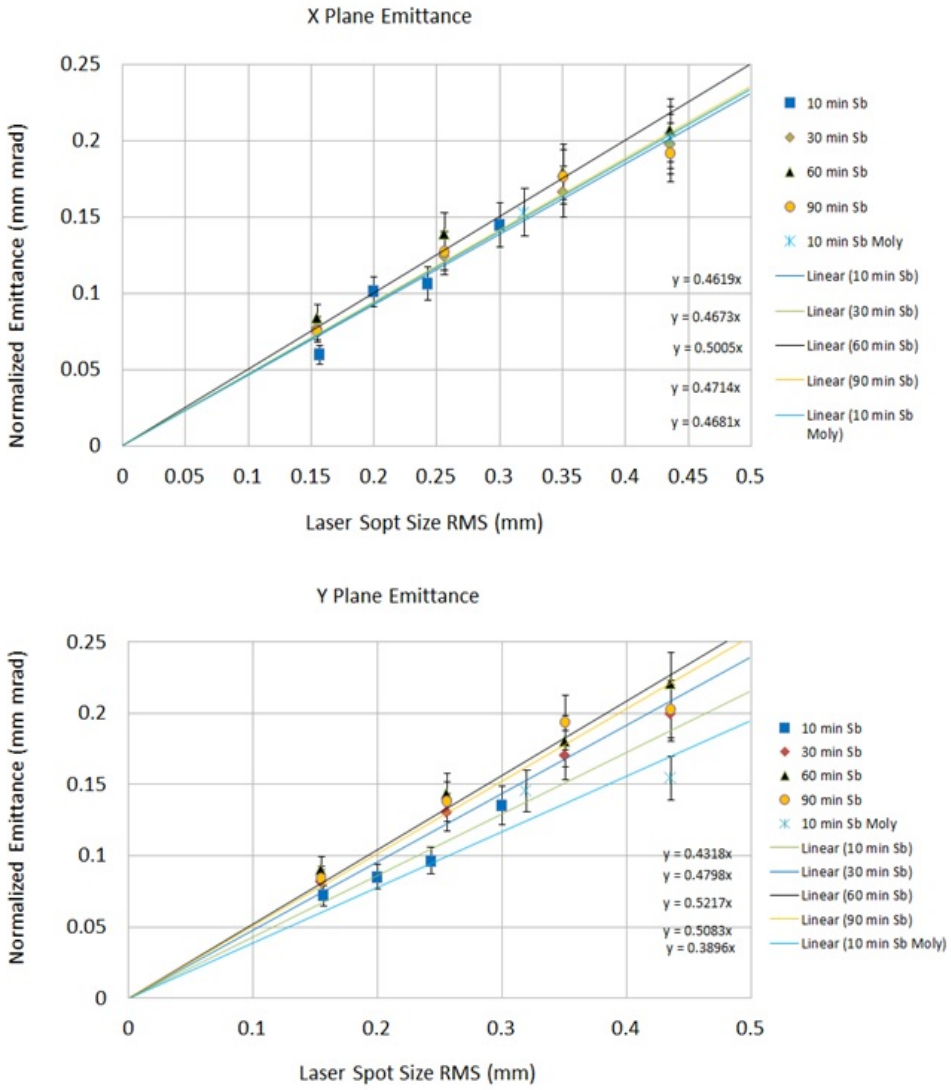

FIG. 76: Normalized emittance versus laser spot rms size for each photocathode.

Sb layer increases with the deposition time, one can conclude that the thickness of the Sb layer does not affect the thermal angles significantly. Since the thermal angle is just the emittance normalized to the laser size one can conclude that the thickness of the Sb layer does not affect the emittance significantly. The Cornell university research group measured the thermal angle under similar conditions and their result is 0.56 ± 0.03 mrad [19].

With 10 minutes of Sb deposition time there are two photocathodes: one has the GaAs substrate; the other has the molybdenum substrate. Figure 77 shows that these two photocathodes have almost identical thermal angles, which means that the substrate materials do not affect the thermal angle or the beam emittance. Originally the molybdenum substrate photocathode was not included in the study plan, therefore there are no data for the molybdenum substrate photocathodes with Sb deposition time of 30, 60, and 90 minutes.

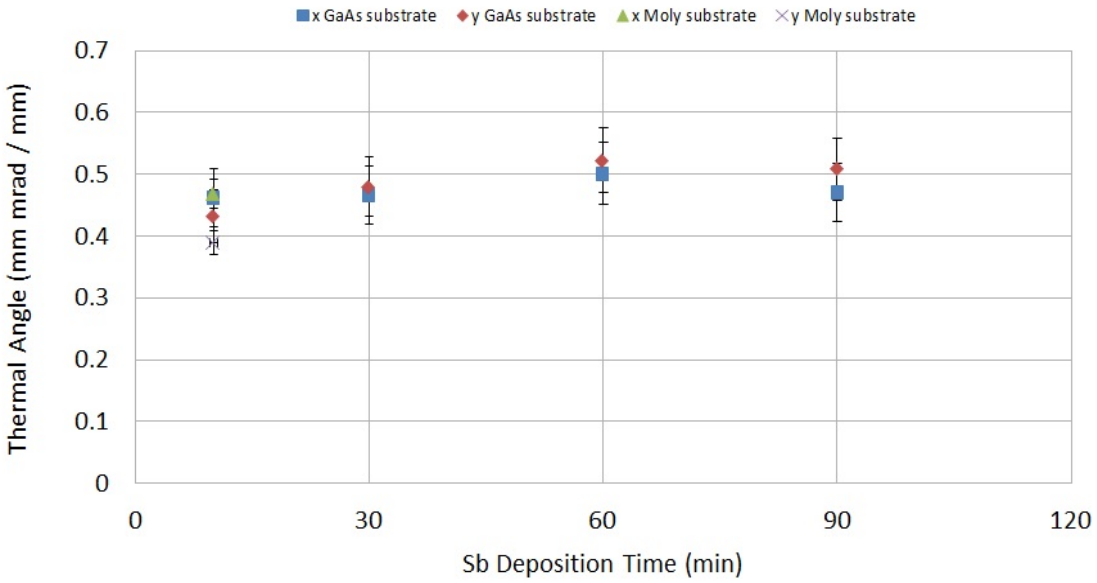

FIG. 77: Thermal angles do not vary much with Sb deposition time.

6.8 PHOTOCATHODE SURFACE ROUGHNESS AND THICKNESS OF THE ANTIMONY LASER

When fabricating the photocathodes different deposition times were used to grow antimony layers. While keeping constant the current (25 A) to the antimony heater the deposition times were 10, 20, 30, 60 and 90 minutes. The longer deposition time makes the antimony layer thicker. These different deposition times make the thicknesses of the

antimony layers range from a few dozen nm to several hundred nm. The thickness of the antimony layer affects the surface roughness of the photocathode. Table 5 shows the green laser light absorption rate and reflection rate. The data were obtained by measuring the incident laser power and reflected laser power. Then the absorption rates were calculated. The laser light shined on the photocathode or the substrate by rotating the puck. Table 5 indicates that the thickness of the antimony layer affect the surface roughness of the photocathode. For a photocathode with thin antimony layer the substrate materials may affect the surface roughness of the photocathode.

TABLE 5: Absorption and reflection rate of green laser light.

Materials	Substrate	Deposition time of Sb (min)	QE (%)	Absorption rate (%)	Reflection rate (%)
Photocathode	GaAs	30	5.23	73.2 ± 0.8	26.8 ± 0.8
Photocathode	GaAs	60	8.79	89.1 ± 0.3	10.9 ± 0.3
Photocathode	GaAs	90	6.30	85.4 ± 0.4	14.6 ± 0.4
Photocathode	Molybdenum	10	8.25	89.9 ± 0.3	10.1 ± 0.3
Molybdenum only	N/A	N/A	N/A	68.2 ± 0.8	31.8 ± 0.8
GaAs only	N/A	N/A	N/A	65.8 ± 0.9	34.2 ± 0.9

6.9 HIGH CURRENT RUN AND PHOTOCATHODE QE LIFETIME

QE lifetime is a very important property of a photocathode. A good photocathode should have a long lifetime and can sustain a long delivery of beam. Four photocathodes with GaAs substrate and one photocathode with molybdenum substrate were used for the lifetime studies. The QE lifetime is evaluated for a photocathode by continuously running CW beam from a single location on the photocathode for an extended time period. Usually high current beams are used for this study. During the high current beam running the photocathode QE will decay. The photocathode QE lifetime is defined as the time it takes for the initial QE_0 to drop to QE_0/e, with e being the Euler's number. Sometimes the photocathode QE lifetime is defined in terms of the charge extracted for the initial QE_0 to drop to QE_0/e. Table 6 shows the calculated QE lifetime and conditions. In Table 6 the first column is the gun high voltage, the second column is the gun solenoid current, the third column is

the substrate of the photocathode, the fourth column is the Sb deposition time when the photocathode was made, the fifth column is the electron beam current delivered during a QE lifetime measurement, the sixth column is the duration of a lifetime measurement, and the last column is the calculated QE lifetime in Coulombs.

Figure 78 shows a plot of the lifetime versus Sb thickness for the GaAs substrate photocathodes. It is obvious that the thickness of the Sb layer affects the photocathode lifetime. But it does not seem to have a pattern: the photocathode with 90 minute Sb deposition time has much longer lifetime; the other three photocathodes have their lifetimes close to each other.

TABLE 6: QE lifetime measurements of photocathodes.

HV(kV)	Solenoid(A)	Substrate	Sb depo time(min)	I(mA)	T(h)	LT(C)
-100	150	Moly	10	28.0	58	9.4e03
-100	150	Moly	10	20.0	20	3.3e11
-200	200	Moly	10	14.0	90	1.0e13
-200	200	Moly	10	4.5	37	9.0e11
-200	0	Moly	10	4.5	11	2.2e05
-200	0	GaAs	20	4.5	6	1.6e02
-200	0	GaAs	30	1.0	6	1.1e02
-200	0	GaAs	60	1.0	9	2.8e01
-200	0	GaAs	90	4.5	10	6.6e03

Table 6 also shows that photocathodes with molybdenum substrate have outstanding lifetimes. Figure 79 shows that the lifetime versus beam current for the photocathode with molybdenum substrate. The Sb layer is thin because the Sb deposition time is only 10 minutes.

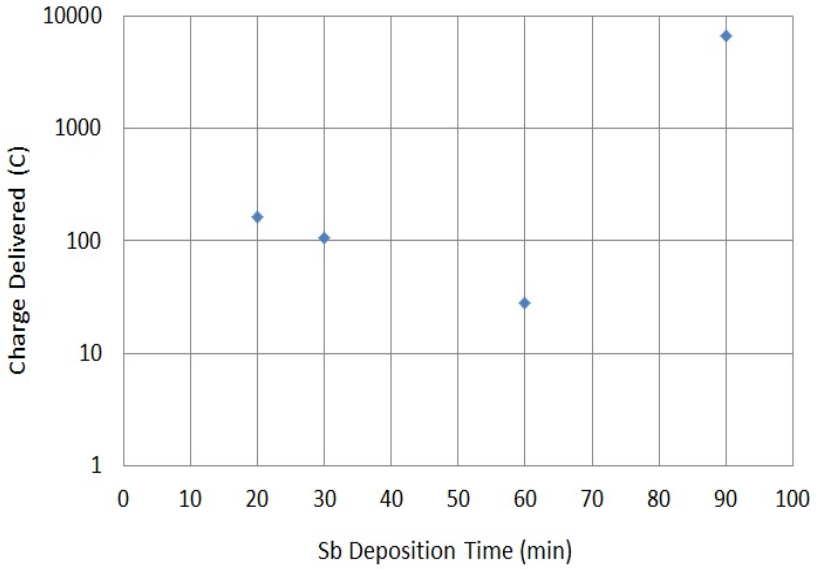

FIG. 78: Lifetimes of photocathodes with GaAs substrate and different Sb deposition time (from table 6).

Figures 80 and 81 are the lifetime measurements at 20 mA and 28 mA. At 20 mA the calculated lifetime is almost infinite but at 28 mA the lifetime is much shorter but still remarkably good. Different substrate materials affect the QE lifetime but not the beam emittance as discussed in Section 6.7.

At this stage the current could not be raised to higher than 28 mA because of hardware limitations. After hundreds of hours of use the molybdenum substrate photocathode's QE had dropped from 8.25% to 3.25%. The laser power reached its limit which is about 1.8 W. The high voltage power supply has its power limit, 3 kW, leading to the average current limit.

The GTS beamline is short and some of the beam-generated ions travel towards the gun vacuum chamber and damage the photocathode. The gun solenoid can serve as a magnetic mirror. Therefore the ions are turned away and do not hit the photocathode when the gun solenoid is energized. During the high current runs the anode was biased to positive 1000 V to repel the ions so they will not go into the photogun chamber. The combination of energizing the gun solenoid and biasing the anode prevents the photocathode from damage by the ions.

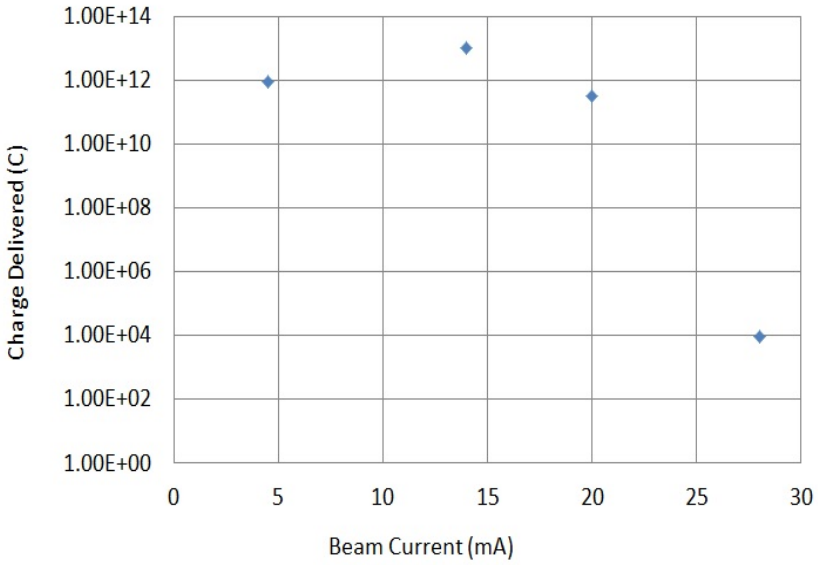

FIG. 79: Lifetime of photocathode with molybdenum substrate at different beam currents.

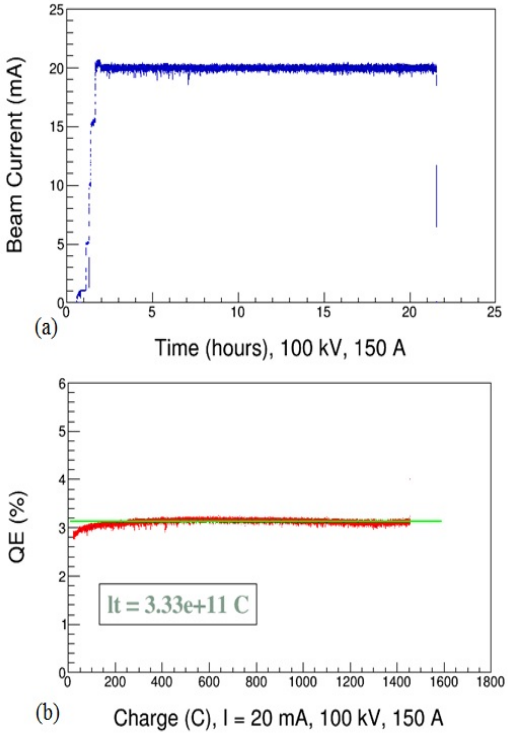

FIG. 80: Lifetime measurement with beam current of 20 mA. (a) Current vs time (b) QE vs charge delivered.

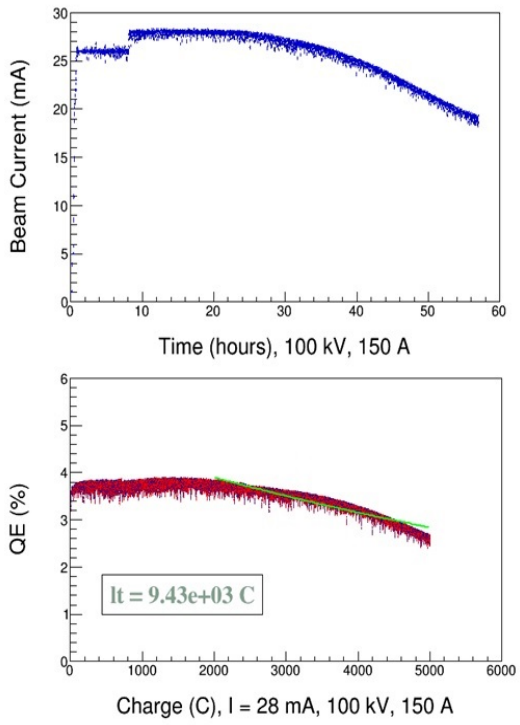

FIG. 81: Lifetime measurement with beam current of 28 mA. (a) Current vs time (b) QE vs charge delivered.

6.10 ERROR ANALYSIS AND LIMITATIONS

6.10.1 ERROR ANALYSIS

No physical quantity can be measured with perfect certainty. There are always errors in any measurement. However, a greater care and more refined experimental methods can reduce the errors in the measurements. There are two types of experimental errors: systematic errors and statistical errors. Common sources of systematic errors are faulty calibration of measuring instruments, poorly maintained instruments, or faulty reading of instruments by the user. Random errors are errors that affect the precision of a measurement. Statistical errors, also called random errors, can be reduced by repeating the measurement or by refining the measurement method or technique. Table 7 show the systematic errors in emittance and thermal angle from the possible source. The first and second columns contain the variables and the associated errors. The third and fourth columns are the resultant errors in the emittance and thermal angle. Those resultant errors for emittance are obtained by

$$\frac{\Delta\varepsilon}{\varepsilon} = \frac{|\varepsilon_1 - \varepsilon_2|}{(\varepsilon_1 + \varepsilon_2)/2}, \tag{6.1}$$

where ε_1 and ε_2 are calculated emittance with and without the variable errors, respectively, and

$$\Delta\varepsilon = |\varepsilon_1 - \varepsilon_2|, \tag{6.2}$$

$$\varepsilon = (\varepsilon_1 + \varepsilon_2)/2. \tag{6.3}$$

The total error in the last row is calculated using

$$\frac{\Delta\varepsilon_t}{\varepsilon} = \sqrt{(\frac{\Delta x_1}{x_1})^2 + (\frac{\Delta x_2}{x_2})^2 + (\frac{\Delta x_3}{x_3})^2 + ...} \tag{6.4}$$

The errors for the thermal angle are obtained in the similar way. The error from the wire size of the wire scanner is not considered because the ratio of the beam size and the wire size is at least 25 to 1. With this ratio the measured beam error caused by the wire size is negligible (0.004%) [24].

TABLE 7: Systematic errors from possible sources.

Error source	Error (%)	Resultant x emittance errors (%)	Resultant y emittance errors (%)
Beam energy	0.11	0.18	0.22
Solenoid field map	2.00	1.00	1.00
solenoid current	0.04	0.12	0.06
Distance between lens and harp	0.33	0.71	0.34
Total error (%)		1.04	1.08

Tables 8 and 9 are the statistical errors for x and y planes, respectively. The percentage error for x emittance is estimated to be

$$1.05\% + 0.55\% = 1.60\%, \tag{6.5}$$

and for y is

$$1.08\% + 1.74\% = 2.82\%. \tag{6.6}$$

TABLE 8: Statistical error analysis data for the horizontal rms beam sizes and thermal angles for 3 trials and 8 solenoid current settings.

Solenoid I (A)	2.244	2.204	2.164	2.124	2.084	2.044	2.004	1.964	x emittance (mm mrad)
x beam size (rms, mm) σ_1	0.905	0.721	0.609	0.579	0.614	0.742	0.894	1.045	0.125
x beam size (rms, mm) σ_2	0.875	0.724	0.611	0.573	0.621	0.743	0.872	1.052	0.124
x beam size (rms, mm) σ_3	0.880	0.722	0.609	0.573	0.619	0.731	0.878	1.049	0.123
Average	1.062	0.722	0.609	0.573	0.619	0.739	0.882	1.048	0.124
sd	0.013	0.001	0.001	0.005	0.004	0.005	0.009	0.003	0.001
% error	1.49	0.2	0.24	0.78	0.63	0.74	1.103	0.25	0.55

TABLE 9: Statistical error analysis data for the vertical rms beam sizes and thermal angles for 3 trials and 8 solenoid current settings.

Solenoid I (A)	2.244	2.204	2.164	2.124	2.084	2.044	2.004	1.964	y emittance (mm mrad)
y beam size (rms, mm) σ_1	0.934	0.737	0.622	0.553	0.610	0.726	0.879	1.071	0.128
y beam size (rms, mm) σ_2	0.940	0.771	0.641	0.577	0.648	0.748	0.906	1.055	0.132
y beam size (rms, mm) σ_3	0.926	0.765	0.634	0.566	0.625	0.718	0.899	1.148	0.133
Average	0.945	0.758	0.632	0.565	0.628	0.731	0.895	1.092	0.130
sd	0.012	0.015	0.008	0.010	0.015	0.013	0.011	0.041	0.002
% error	1.13	1.94	1.23	1.78	2.45	1.72	1.23	3.73	1.74

6.10.2 LIMITATIONS

The maximum beam current was limited to 28 mA due to the fact that the two high voltage power supplies used had either a current limit or a power limit. When 28 mA beam was run the anode was positively biased to 1000 V to prevent the ion bombardment. The anode bias voltage most likely needs to be increased to a higher level for higher current runs. The existing feedthrough for the anode bias is not designed for an bias voltage higher than 2000 V. In order to run higher current beam an higher rated feedthrough for anode bias and a power supply with higher current and power limits are needed.

The beam profiler, the YAG viewer, cannot reliably measure the beam size smaller than 500 μm due to power saturation on the YAG film. The wire scanner has three wires. All the three wires have the same diameter of 20 μm. It can measure the beam size smaller than the wire size [24]. In this research setup the smallest size for the emittance measurements is about 500 μm. Most data taken using the viewer were just for cross checking.

CHAPTER 7

CONCLUSION AND OUTLOOK

7.1 CONCLUSION

DC high voltage photoguns are in high demand as electron accelerators. The successful design, construction, and operation of this novel inverted-insulator geometry DC photogun represents a significant contribution to the accelerator electron-gun field. An electron beam produced from a gun operating at higher voltage has higher energy, which makes it easier for the beam to transport into accelerating RF cavities. A DC high voltage photogun based on an inverted-geometry insulator design was constructed using centrifugal barrel-polished electrodes and standard high voltage DC photogun assembly techniques and procedures. High voltage conditioning using krypton gas is very effective. The gun was conditioned to -360 kV and demonstrated stable beam operations at -300 kV without field emission. This new compact and simple design makes it easier to build a DC photogun capable of -300 kV operation.

The barrel polishing technique is a good way to polish the gun parts compared to the diamond paste polishing, providing microscopically smooth surfaces in only hours instead of many days. The shed linearized the potential along the insulator and significantly lowered the electric field at the triple-point junction. The implementation of the shed protected the insulator from damage at high voltages. The insulator and shed alter the electric field symmetry in the region between the photocathode and anode. GPT simulation predicted that the effect on the electron beam is not significant so no correction was made but a design for correction is available if needed in the future. The electron beam transported well from the gun to the beamline dump with very low interception on the anode, which confirms the GPT simulation and supports the statement that field asymmetry does not significantly affect beam transport.

A vulnerable part of the gun is the insulator because the electric potential drop from one end to the other of the insulator is 300 kV. A linear potential drop along the insulator is preferred. Also the electric field is high in the region where the insulator connects the electrode. The region is called a triple-point-junction because it is where the insulator, metal and vacuum meet.

Electrostatic field maps were obtained using the POISSON SUPERFISH electrostatic solver and iterative adjustments to the electrostatic model served to optimize the diameter of the cathode electrode within the gun chamber, to set the cathode-anode gap, and to refine the shape of the triple-point junction shield with the goal of keeping the electric field strength less than 10 MV/m at -300 kV bias voltage. Higher DC field strengths often lead to field emission that can be very difficult to process out. The photogun has two axes of symmetry: the vertical axis defined by the insulator and the longitudinal axis defined by the electron beam path in the anode-cathode gap. The high voltage analysis of the insulator and plug including corresponding dielectric properties and the design of the triple-point junction shield were performed using cylindrical symmetry, while the anode-cathode gap optimization was done using Cartesian coordinates. A shed was designed to lower the electric field in the triple-junction-point and linearize the electric potential drop along the insulator.

The beam emittance was measured across the entire photocathode. The emittance was measured horizontally at nine points, and vertically at eight points. The data show that emittance is uniform across the photocathode surface, except at the very edge of the photocathode where emittance is higher but this result is expected because the electric field near the edge is altered by the cathode front-face plate.

The beam emittance at a damaged spot is basically the same as measured elsewhere on the photocathode although the QE at the damaged spot is much lower. Although a damaged spot can affect the spatial distribution of the electron beam, it will not significantly impact the phase space quality of the beam.

As an electron bunch is accelerated the longitudinal momentum increases while the transverse momentum remains constant. Thus, the emittance is expected to decrease as $\langle p_z \rangle$ increases. The relativistic factor makes the emittance invariant under acceleration. The experimental data show that the emittance with the relativist factor, the normalized emittance, is constant when the gun voltage is above about -200 kV. At lower voltages, emittance was observed to change, likely due to space charge forces.

During the emittance measurements the YAG beam profiler was limited when measuring beam size smaller than 500 μm due to power saturation on the YAG. A wire scanner with wire size 20 μm is a more reliable beam profiler and can measure a beam size smaller than its wire size. The GTS wire scanner was needed to measure the small beam emittances produced at the photocathode.

Six alkali antimonide photocathodes manufactured on two different substrate materials (GaAs and molybdenum) were investigated. During high current runs, a significant amount

of gas is generated along the beamline and at the beam dump. This gas can be ionized by the electron beam. When produced in sufficient number, the ions within the cathode/anode gap can provide an arc path to ground. So-called micro-arc discharges serve to reduce QE, however the damage is very localized and limited to well-defined small spots. The rest of the photocathode is still good.

The thickness of the Sb layer affects the grain structure, morphology, surface roughness, and porosity of the Sb film. The experimental data show that the thickness of the Sb layer does not affect the beam emittance significantly. There is only a slight emittance growth as the Sb layer becomes thicker. There is no discernible effect on the beam emittance between the two photocathodes with different substrates (GaAs and molybdenum).

For the photocathodes grown on GaAs substrates, the experimental data indicate that the thickness of the Sb layer significantly affects the QE lifetime. The photocathode with the thickest Sb layer exhibited the best lifetime. Different substrate materials also affect the photocathode lifetime. A photocathode sample manufactured with a thin Sb layer on a molybdenum substrate exhibited markedly better photocathode lifetime compared to a similar photocathode manufactured on a GaAs substrate. One possible explanation is laser heating. During high current runs, high laser power is needed and the heat from the laser could affect the structure of the photocathode, which in turn affects the QE and lifetime of the photocathode. The thermal conductivity of molybdenum (139 W m^{-1} K^{-1}) is much higher than that of GaAs (55 W m^{-1} K^{-1}) [25] [26]. As a result, photocathodes grown on GaAs are expected to get hotter during operation, sometimes producing a good result (e.g., improved stoichiometry) or a bad result (e.g., photocathode decomposition). And as the photocathode gets hotter, the band-gap is expected to shift, resulting in reduced QE for illumination with laser light at a constant wavelength. Perhaps a band-gap shift would be temporary, with QE returning to the original value when beam generation is halted and the photocathode cools.

Another possible explanation relates to the lattice spacing of atoms in the substrate and Sb film, with lattice matching providing the best conditions for proper Sb crystal growth, and the best photocathode lifetimes. The lattice spacing of GaAs, molybdenum and antimony are 5.653, 3.147, and 4.307 Å, respectively. The molybdenum substrate provides a better lattice match to the Sb film.

Reliable and sustained high current operation was achieved after the anode was biased to +1000 kV. The positively biased anode repels ions generated in the beamline so that they will not enter the cathode/anode gap. The highest beam current delivered was 28 mA. The

beam current was limited by the available laser power (1.8 W), the photocathode QE, and the power limitation of the high voltage power supply (limited to 3 kW).

A key feature that contributed to the success of this new gun design is the shed. The shed redistributes the electric potential and fields in the photogun chamber in a controlled way so that the field at the triple-point junction is low and there will be no electric breakdown. As a result of this work, Jefferson Lab's main accelerator and the upgraded injector test facility now employ similar designs. The low energy recirculator facility (LERF) at Jefferson Lab will soon replace its bulky existing photogun with a gun of this new design. Most importantly, this research paved the way for the JLEIC cooler.

This research demonstrated that Cs_xK_ySb photocathodes with molybdenum substrate exhibit remarkably long lifetimes, and the beam emittance, or more accurately, the thermal angle, is low. The research answered the question, "how does the photocathode surface roughness affect the beam emittance", asked by many researchers in the photocathode field. There was no significant effect of thickness on beam emittance in the cases measured.

7.2 OUTLOOK

It is possible the present photogun can be operated at voltage higher than -300 kV, although risking damage of expensive insulators. But even assuming a maximum operating voltage of -300 kV, the work presented here provides a pathway to design a photogun capable of reaching -500 kV bias voltage, which is a value at which space charge forces are largely inconsequential. Simply scale the dimensions of important features of the -300 kV gun (gun chamber, shed, cathode electrode and insulator) by a factor 5/3.

The dielectric constant of the insulator used in this research is 8.4. Materials with higher dielectric constant can be used for the insulator. But the insulator with higher dielectric constant should be covered with a thin layer of material with lower dielectric constant so that the accumulated charges on the surface can be drained.

Studies can be performed at even higher current with a high voltage power supply with higher current and power capability. The limiting factors of high beam current are the laser power, the high voltage power supply, the photocathode QE, and ion bombardment. The laser and the high voltage power supply are not an issue. Powerful lasers and power supplies with high capability are commercially available. One can study how to make photocathodes with high QEs. Different materials can be investigated. Same materials but different recipes can be used to see how the QE is affected. Some amount of the ions generated in the

beamline during the high current operations travel towards the photocathode and damage the photocathode. When those energetic ions hit the photocathode they change the photocathode thin film structure and the QE will be lowered. A couple of methods can be studied and compare the results to see which is a good way to prevent the ion bombardment. This research already demonstrated biasing the gun anode is an effective way. An ion collector can be installed in the beamline close to the gun exit. If an ion collector attracts all the ions traveling towards the gun the photocathode would be saved. A short distance downstream of the gun exit the beamline can bent at an angle. The ions traveling towards the photocathode would be steered away by the bending magnet. Maybe a combination of those methods would work the best.

When delivering high beam current the temperature of the photocathode spot the laser hits may be increased. The heating could affect the photocathode QE or QE lifetime. Currently there is no good way to monitor the temperature while delivering beam.

This research did not measure the thickness of the Sb layers. The photocathode roughness is related to the thickness of the Sb layer. Both the surface roughness and the thickness of the Sb layer need to be measured. There may be a correlation between surface roughness, Sb layer thickness, and QE.

The current apparatus in GTS does not have stoichiometry control. The alkali antimonide is Cs_xK_ySb and x and y are unknown until the sample is analyzed. If the stoichiometry can be controlled the ratio of x and y may affect the QE and QE lifetime. With control, better optimized photocathodes may be possible.

BIBLIOGRAPHY

[1] "Pre-Conceptual Design Report (pCDR) for The Jefferson Lab Electron-Ion Collider JLEIC", Jefferson Lab, September 2018.

[2] P. Piot and Y. E. Sun, "Generation and Dynamics of magnetized Electron Beams for High-Energy Electron cooling", FERMILAB-CONF-14-142-APC.

[3] C. Hernandes-Garcia, "GTS 600 kV Gas Insulated Power Supply Maintenance and Safety", Jefferson Lab Operational Safety Procedure, 2017.

[4] M. A. A. Mamun, "Thin Film Studies Toward Improving The Performance Of Accelerator Electron Sources", PhD thesis, OLD DOMINION UNIVERSITY, 2016.

[5] J. H. Billen and L. M. Young, "POISSON SUPERFISH, http://laacg1.lanl.gov/laacg/services/servcodes.phtml.

[6] S. B. van der Geer, "General Particle Tracer (GPT)", http://www.pulsar.nl.

[7] C. Hernandez-Garcia, D. Bullard, F. Hannon, Y. Wang, and M. Poelker, "High voltage performance of a dc photoemission electron gun with centrifugal barrel-polished electrodes", Review of Scientific Instruments 88, 093303, 2017.

[8] C. Hernandez-Garcia, S. V. Benson, G. Biallas, D. Bullard, P. Evtushenko, K. Jordan, M. Klopf, D. Sexton, C. Tennant, R. Walker, and G. Williams, "DC High Voltage Conditioning of Photoemission Guns at Jefferson Lab FEL", AIP Conference Proceedings 1149, 1071, 2009.

[9] M. BastaniNejad, A. A. Elmustafa, E. Forman, J. Clark, S. Covert, J. Grames, J. Hansknecht, C. Hernandez-Garcia, M. Poelker, and R. Suleiman, "Improving the performance of stainless-steel DC high voltage photoelectron gun cathode electrodes via gas conditioning with helium or krypton", Nuclear Instruments and Methods in Physics Research A 762, 135141, 2014.

[10] M. A. Mamun and A. A. Elmustafa, "Effect of Sb thickness on the performance of bialkali-antimonide photocathodes", Journal of Vacuum Science & Technology A 34, 021509, 2016.

[11] H. Wiedemann, *Particle Accelerator Physics,* Springer, 3rd ed., 2007.

[12] K. Wille, *The Physics of Particale Accelerators - An Introduction,* Oxford University Press, 1st ed., 2005.

[13] E. Wilson, *An Introduction to Particle Accelerators,* OXFORD University Press, 1st ed., 2001.

[14] D. Jackson, *Classical Electrodynamics,* John Willey & Sons, Inc., 3rd ed., 1998.

[15] M. Hachmann, "Transverse emittance measurement at REGAE via a solenoid scan". PhD thesis, University Hamburg, 2012.

[16] F. E. Hannon, "A High Average-Current Electron Source for the Jefferson Laboratory Free Electron Laser", PhD thesis, University of Lancaster, 2008.

[17] P. R. Bevington, *Data Reduction and Error Analysis for the Physical Sciences,* McGraw-Hill Book Co., 1969.

[18] M. Minty and F. Zimmermann, *Measurement and control of charged particle beams,* Springer., Berlin, Heidelberg, New York, 2003.

[19] I. Bazarov, L. Cultrera, A. Bartnik, B. Dunham, S. Karkare, Y. Li, X. Liu, J. Maxson, and W. Rousse, "Thermal emittance measurements of a cesium potassium antimonide photocathode", Applied Physics Letters 98, 224101, 2011.

[20] I. Bazarov, B. Dunham, F. Hannon, Y. Li, X. Liu, T. Miyajima, D. Ouzounov, and C. Sinclair, "Thermal emittance measurements from negative electron affinity photocathodes", Proceedings of PAC07, Albuquerque, New Mexico, USA, 2007.

[21] B. Dunham, "Investigations of the physical properties of photoemission polarized electron sources for accelerator applications", PhD thesis, University of Illinois at Urbana-Champaign, 1993.

[22] S. Anderson and J. Rosenzweig, "Space-charge effects in high brightness electron beam emittance measurements", Physical Review Special Topics - Accelerators and Beams, volume 5, 014201, 2002.

[23] G. Gevorkyan, S. Karkare, S. Emamian, I. V. Bazarov, H. A. Padmore, "Effects of physical and chemical surface roughness on the brightness of electron beams from photocathodes", Physical Review Accelerators and Beams 21, 093401, 2018.

[24] A. Freyberger, "Wire Scanner Response", Jefferson Lab Tech Note, JLAB-TN-14-002, 2014.

[25] "Technical data for Molybdenum", http://periodictable.com/Elements/042/data.html.

[26] "Thermal of Gallium Arsenide (GaAs)", http://www.ioffe.ru/SVA/NSM/Semicond/GaAs/thermal.html.

APPENDIX A

SAFETY SYSTEM

The GTS Personnel safety system is a stand-alone system, which ensures the personnel safety. There are access mode, sweep mode, beam mode, and laser alignment mode.

The access mode is an open mode when the beam enclosure is open for maintenance and down periods. The sweep mode is a mode while the beam enclosure is being locked up. The beam mode is the mode that the devices can be energized and beam run. The laser alignment mode is the state when personnel can be in the beam enclosure and work on the laser system. When the beam enclosure is in any state other than open state the beam enclosure will drop to the open state if the entrance door is opened.

There are also an ODH system and a radiation monitoring system at the GTS which are not interlocked.

APPENDIX B

CONTROL SYSTEM

The Experimental Physics and Industrial Control System (EPICS) is used in this research. EPICS is a software environment used to develop and implement distributed control systems to operate devices such as particle accelerators, telescopes and other large experiments. EPICS interfaces to the real world with IOCs (Input Output Controllers). https://epics.anl.gov/

EPICS uses Client/Server and Publish/Subscribe techniques to communicate between the various computers. Most servers (called Input/Output Controllers or IOCs) perform real-world I/O and local control tasks, and publish this information to clients using the Channel Access (CA) network protocol.

EPICS was originally written jointly by Los Alamos National Laboratory and Argonne National Laboratory, and is now used by many large scientific facilities throughout the world (see the EPICS Sites page for some of the major users). Development now occurs cooperatively between these various groups, with much sharing of I/O device support and client applications.

APPENDIX C

BEAM MODE

In GTS there are three operational beam modes: viewer limited mode, tune mode, and CW beam. The beam has a line sync of 60 Hz with the period of 16.667 ms.

Viewers are diagnostic devices and usually cannot take high power beam. Viewer limited mode beam is a low-power beam mode for viewers. Beam is limited for 1 to 10 μs for each 60 Hz cycle (16.667 ms). The duty factor is less than 0.06%. In order to avoid to damage a viewer the viewer limited beam should be used whenever a viewer is inserted in the beam path. Usually several nA beam is enough to see a clear image on a viewer. A viewer can be used to check beam presence and shape, measure the beam size, center a solenoid, etc. In GTS viewers are safety interlocked with beam mode: when a viewer is inserted into the beamline the beam mode changes to the viewer limited mode automatically.

The tune mode is that beam is on for 250 μs for each cycle. The duty factor is 1.5%. When commissioning or tuning beamline the tune mode beam is safe to use.

Continuous Wave (CW) mode has beam on for the entire cycle. The duty factor is 100%. The beam has full power. Most experiments use the viewer limited beam and tune beam for commissioning and tuning, CW beam for production runs.

In this research the viewer limited beam and tune beam were used to commission the beamline and measure beam emittance. CW beam was used to measure the lifetime of photocathodes.

APPENDIX D

SOFTWARE TOOLS

The POISSON SUPERFISH is a free software tool maintained by Los Alamos National Lab. POISSON SUPERFISH is a collection of programs for calculating static magnetic and electric fields and radio-frequency electromagnetic fields in either 2-D Cartesian coordinates or axially symmetric cylindrical coordinates. The programs generate a triangular mesh fitted to the boundaries of different materials in the problem geometry. In this research only the static electric field distribution model is needed. http://laacg1.lanl.gov/laacg/services/servcodes.phtml

GPT is based on full 3D particle tracking techniques, providing a solid basis for the study of 3D and non-linear effects of charged particles dynamics in electromagnetic fields. All built-in beam line components and external 2D/3D field-maps can be arbitrarily positioned and oriented to simulate a complicated setup. GPT provides various 2D and 3D space-charge models. http://www.pulsar.nl

ROOT is a modular scientific software framework. It provides all the functionalities needed to deal with massive data processing, statistical analysis, visualization and storage. It is mainly written in C++ but integrated with other languages such as Python and R. https://root.cern.ch. Three programs were written using ROOT in this research to calculate the beam emittances and errors, photocathode QE lifetimes, and gun high voltage run times.

APPENDIX E

REPLACEMENT OF ANTIMONY

Below is the procedure for loading Sb to the prep chamber.

1. Lock out the power supply for the Sb source heater.
2. Close the gate valve between the prep chamber and gun chamber. Close the valve between the prep chamber and the ion pump and turn on the ion pump. Close the valve between the prep chamber and the turbo pump.
3. Detach the Sb-source-linear-actuator assembly from the prep chamber at the connecting flange. Once it is detached insert tubing to have constant nitrogen in the chamber to keep it dry and clean.
4. Use a pair of clean tweezers and to take out the crucible from the heater basket and clean it using cleaning agent. Put back the clean crucible to the heater basket.
5. Loaded about 1 g of high-purity (99.9999%) Sb pellets to the crucible.
6. Replace the used gasket for the flange and take out the nitrogen tubing.
7. Carefully insert the Sb source portion into the prep chamber and tighten the screws for the flange.
8. Open the valve between the prep chamber and the turbo pump and let it pump until the vacuum reaches about 10^{-5} Torr
9. Start to bake the system at 200 °C using heat tapes or an oven. It takes 24 to 48 hours.
10. A few hours prior to terminating the bake activate the NEGs.
11. After the bake is done open the valve between the prep chamber and the ion pump.
12. Check the turbo pump readback. If it is good, about 10^{-7} or 10^{-8} Torr, turn on the ion pump.
13. When the ion pump current readback is below 100 nA perform a leak check using helium and the RGA.
14. If no leak the procedure is complete.

APPENDIX F

REPLACEMENT OF CESIUM AND POTASSIUM

Below is the procedure for loading Cs and K to the reservoir.

1. Close the bakeable metal valve.
2. Detach the pinch-off copper tube from the mini flange underneath the metal valve.
3. Cut off the pinch-off portion and re-use the tube, or find a new copper tube with a mini flange on one end. The tubing ID is 1.12 cm and OD 1.27 cm.
4. Insert 1 g potassium breakseal ampule and 1 g cesium breakseal ampule into the copper pinch-off tube.
5. Pinch-off the open end of the tube to make a vacuum tight seal.
6. Attach the loaded tube to the dispenser by tightening the mini flange screws.
7. Open the metal vale. Use a heat tape to heat up the copper tube up to 200 °C for a few hours to desorb water. Pump out the water.
8. Stop the heating and wait until the pressure recovers and the tube reaches the room temperature.
9. Brake the glass ampules by slightly pinching the outside of the copper tube, cracking the glass ampules.
10. Pump out the argon released from the ampules.
11. Once vacuum is recovered close the metal valve. Procedure complete.

APPENDIX G

FABRICATION OF PHOTOCATHODES

Below is the procedure for fabricating photocathodes.

1. Move the puck onto the bottom heater. Make sure the Sb source and the dispenser of Cs and K are in the garage position so there will be no undesired release of Cs, K or Sb.

2. Turn on the bottom heater to heat clean the substrate at 550-600 °C for several hours. The longer the cleaner.

3. At the end of heat cleaning, reduce the temperature to 200 °C.

4. Transfer the puck to the top heater. Lower the top heater to put the puck in the predefined position. Turn off the bottom heater and lower it to the lowest position (safe position).

5. Use the SOLO to turn on the top heater and maintain the temperature at 200 °C so the substrate temperature is 100 °C due to 50 % efficiency.

6. If a limited active area is desired, move the mask underneath the puck, aim a desired size hole at the center of the substrate. The distance between the puck and the mask is about 1 mm. Make sure they do not touch each other by checking the conductivity using a multimeter. See Figure 40 (b) for the circuit.

7. If full activation is desired, move the mask underneath the puck. The distance between the puck and the mask is about 1 mm. Make sure they do not touch each other by checking the conductivity using a multimeter. Then move the mask away from the puck until the substrate is just fully uncovered.

8. Turn on the laser and align it. If full activation, make sure the laser hits the center of the substrate. Otherwise aim the laser to the hole picked in step 6.

9. Turn on the power to the Sb source with it in the garage position. Set the power supply current 25 A. Use a clamp meter to double check the current is 25 A. Wait for five minutes to make sure the Sb is hot.

10. Move the Sb source to the predefined position: center of the prep chamber, 3.8 cm below the substrate.

11. Start the timer. Deposition time is determined according to your plan. The longer deposition time the thicker Sb layer. Monitor the partial pressure of Sb via the RGA. The prep chamber pressure would be going up too which can be monitored via the ion pump power supply.

12. Once the timer is up quickly move the Sb source back to the garage position. Turn off the power to the Sb source.
13. The deposition of Sb is complete. The following steps are for the co-deposition of Cs and K.
14. Make sure the Cs and K reservoir valve is closed for the. Set the Cs and K reservoir temperature limit to 350 °C. Turn on the nitrogen flow regulator for the reservoir heater to start heating the reservoir. This could take more than a hour. Monitor the the reservoir temperature and dispenser temperature.
15. Adjusting the nitrogen flow regulator would affect the speed of heating up the reservoir. The reservoir temperature usually should be around 300 °C in order for the dispenser temperature to reach about 200 °C. Do not let the nitrogen flow too fast otherwise the dispenser temperature would not up fast.
16. Once the dispenser temperature reach 200 °C move the dispenser to the predefined position. Turn on the puck bias to 284 V. Check the laser alignment again.
17. Start co-deposition of Cs and K by opening the reservoir valve. Check the partial pressures of Cs and K.
18. A few minutes later the photocurrent current (pico-ammeter readback) should start to go up slowly. Calculate the QE using the input laser power (0.2 mW) and the photocurrent. When the photocurrent reaches the maximum and starts to decrease retract the Cs and K reservoir to the garage position and close the reservoir valve.
19. Check to see if the QE is reasonable. If QE is good. The co-deposition of Cs and K is complete. Turn off the bias. Turn off the heat. Let vacuum recover.
20. If QE is too low, repeat co-deposition of Cs and K.

APPENDIX H

QE MAPPING OF PHOTOCATHODES

After a photcathode is fabricated a full evaluation of the photocathode is desired. QE mapping is a common evaluation method. The following is the procedure used to QE map a photocathode.

1. Turn on the camera and the monitor of the photocathode-camera-monitor system.
2. Turn on the QE laser and make sure the optical alignment is still correct: the laser light going into the photogun chamber from one view port, hitting the photocathode and coming out of the chamber from another viewer port.
3. Turn on the x/y stage step motor. From the step motor control screen set both x and y to zero. This step places the QE laser at (0, 0) on the photocathode. Adjust the optics to make sure laser hit point A.
4. Set both x and y to 2000. This step set the QE laser at (2000, 2000). Adjust the x/y gain to make sure laser hit point B.
5. Open the gate valve between the gun chamber and prep chamber, electrically ground the photocathode by pushing the long manipulator against the puck.
6. Make sure the anode, the battery and the pico-ammeter are connected so the pico-ammeter can read the photocurrent. Bias the anode to + 284 V.
7. Open the QE TOOL software and from the interface check the information: laser power, laser wavelength, scan ranges, scan step sizes.
8. Hit the scan button.
9. Once the scan is done a QE map pops up. Log the scan result. Repeat the scan as you like.
10. When the scan is finished back out the set up: retract the long manipulator, close the gate valve, turn off the QE laser, turn off the x/y step motor.

APPENDIX I

BASIC PROPERTIES OF CESIUM, POTASSIUM, ANTIMONY, MOLYBDENUM, AND GALLIUM ARSENIDE

Cesium is a highly reactive chemical element with symbol Cs and has atomic number 55. It is a soft, silvery-gold alkali metal with a melting point of 28.5 °C (83.3 °F), which makes it one of only five elemental metals that are liquid at or near room temperature. Caesium has physical and chemical properties similar to those of rubidium and potassium. The most reactive of all metals, it is pyrophoric and reacts with water even at 116 °C (177 °F). It has only one stable isotope, caesium-133. Its boiling point is 641 °C (1,186 °F). Its thermal conductivity is 35.9 W/(mK). Electrons per shell is 2, 8, 18, 18, 8, and 1. It has a body-centered-cubic crystal structure with lattice spacing of 3.62 Å. https://en.wikipedia.org/wiki/Caesium.

Potassium is a chemical element with symbol K and has atomic number 19. Istopes are ^{39}K, ^{40}K, and ^{41}K. Its melting point is 63.5 °C (146.3 °F), boiling point 759 °C (1398 °F). Electrons per shell is 2, 8, 8, and 1. Its thermal conductivity is 102.5 W/(mK). It has a body-centered-cubic crystal structure with lattice spacing of 5.32 Å https://en.wikipedia.org/wiki/Potassium.

Antimony is a chemical element with symbol Sb and has atomic number 51. Isotopes are ^{121}Sb, ^{123}sb, and ^{125}Sb. Its melting point is 630.63 °C (1167.13 °F), boiling point 1635 °C (2957 °F). Electrons per shell is 2, 8, 18, 18, and 5. Its thermal conductivity is 24.4 W/(mK). It has a rhombohedral crystal structure with lattice spacing of 4.307 Å. https://en.wikipedia.org/wiki/Antimony.

Molybdenum is a chemical element with symbol Mo and atomic number 42. It atomic weight is 96. Its melting point is 2632 °C (4753 °F). Its thermal conductivity is 138 W/(mK). its lattice spacing is 3.147 Å. https://en.wikipedia.org/wiki/Molybdenum.

Gallium arsenide (GaAs) is a compound of the elements gallium and arsenic. It has a crystal structure with lattice spacing of 5.65 Å . Its thermal conductivity is 55 w/(mK). Its melting point is 1238 °C. https://en.wikipedia.org/wiki/Gallium_arsenide.

VITA

Yan Wang
Department of Physics
Old Dominion University
Norfolk, VA 23529

Academic Preparation

- Ph.D., Department of Physics, Old Dominion University, Norfolk, Virginia, December 2018
- M.S., Department of Physics, Old Dominion University, Norfolk, Virginia, December 1995
- B.S., Department of Physics, Liaoning University, China, July 1985

Professional Experience

- Jefferson Lab, August 1998 - present, responsible for injector beam operations of Continuous Electron Beam Accelerator

Recent Publications

1. Y. Wang, et. al., "300 kV DC High Voltage Photogun With Inverted Insulator Geometry and CsK_2Sb Photocathode", in Proceedings of IPAC18, Vancouver Canada, May 2018
2. C. Hernandez-Garcia, Y. Wang, et. al., "High voltage performance of a DC photoemission electron gun with centrifugal barrel-polished electrodes", Review of Scientific Instruments 88, 093303, September 2017
3. Y. Wang, et. al., "Commissioning of the 123 MeV Injector for 12 GeV", in Proceedings of IPAC15, Richmond Virginia, May 2015

Typeset using LaTeX.